Progress in Aerospace Sciences 54 (2012) 1–58

Contents lists available at SciVerse ScienceDirect

Progress in Aerospace Sciences

journal homepage: www.elsevier.com/locate/paerosci

Photogrammetric techniques for aerospace applications

Tianshu Liu [a,*], Alpheus W. Burner [b], Thomas W. Jones [c], Danny A. Barrows [c]

[a] Department of Mechanical and Aeronautical Engineering, Western Michigan University, Kalamazoo, MI 49008, USA
[b] Jacobs Technology NASA Langley Research Center, Hampton, VA 23681-2199, USA
[c] NASA Langley Research Center, Hampton, VA 23681-2199, USA

ARTICLE INFO

Available online 27 April 2012

Keywords:
Photogrammetry
Optical measurements
Wind tunnel
Space structure
Flight testing

ABSTRACT

Photogrammetric techniques have been used for measuring the important physical quantities in both ground and flight testing including aeroelastic deformation, attitude, position, shape and dynamics of objects such as wind tunnel models, flight vehicles, rotating blades and large space structures. The distinct advantage of photogrammetric measurement is that it is a non-contact, global measurement technique. Although the general principles of photogrammetry are well known particularly in topographic and aerial survey, photogrammetric techniques require special adaptation for aerospace applications. This review provides a comprehensive and systematic summary of photogrammetric techniques for aerospace applications based on diverse sources. It is useful mainly for aerospace engineers who want to use photogrammetric techniques, but it also gives a general introduction for photogrammetrists and computer vision scientists to new applications.

Contents

* Corresponding author. Tel.: +1 269 276 3426; fax: +269 376 3421.
E-mail address: tianshu.liu@wmich.edu (T. Liu).

0376-0421/$ - see front matter © 2012 Elsevier Ltd. All rights reserved.
http://dx.doi.org/10.1016/j.paerosci.2012.03.002

1. Introduction

Photogrammetry is the science of determining the geometrical (or metric) information (position, size and shape) of objects by analyzing images recorded on films or electronic media. The fundamental problem of photogrammetry is to establish the geometrical relationship between the image plane and the three-dimensional (3D) object space at the time of the imaging event. Once this relationship is correctly established, the relevant geometrical information and derived physical quantities about the object can be obtained from its imagery. Photogrammetric methods are particularly useful when the object to be measured is inaccessible or difficult to access, when the object moves and deforms, and when its contour and surface information is required. The earliest roots of photogrammetry can be traced to the Renaissance painters who studied the principles involved via geometrical analysis in the late 1400s. The next significant development was projective geometry that constitutes the mathematical basis of photogrammetry. Interestingly, the advent of the modern aviation after the first power-flight of the Wright brothers in the early 1900s promoted the great expansion of aerial photogrammetry for topographic mapping from photographs taken by cameras installed in a level-flying aircraft. Therefore, as a result of the intensive research focused on this field, the developed methodology, instrument and terminology of photogrammetry are largely influenced by aerial photogrammetry [46,80,102,109].

With the rapid advance of the technology of electro-optical and video cameras and computers in the 1990s, the analytical photogrammetric techniques based on models of cameras have allowed the use of non-metric cameras and the various applications of close-range photogrammetry (or non-topographic photogrammetry) like industry inspection, medical imagery, and architectural documentation. On the other hand, computer scientists have dealt with the perspective projection problem in computer vision or machine vision related to artificial intelligence while they tend to adopt different formulations and more versatile mathematical methods in perspective geometry, differential geometry and image algebra [81,41,34]. Due to the replacement of films by electronic image sensors, expressions other than photogrammetry have been used to denote this extraction of spatial information from images. Part of the impetus for these name-changes is to emphasize the modern nature of these efforts and to emphasize that digital images, rather than film, make up the raw data. These various names, which are largely a matter of personal choice of researchers of a special application, include digital photogrammetry, geomatics, videogrammetry,

videometrics, and computer vision. Here the generic term 'photogrammetry' is adopted, and sometimes interchangeably used with some of the other terms.

Photogrammetric techniques have been found to be very useful as a remote and non-contact measurement method for specialized aerospace applications including wind tunnel testing, aircraft flight testing, and ground-based and flight testing of large space structures [19,22,99,25,67,83–85]. Although aeronautics has promoted modern topographic photogrammetry, the photogrammetric applications in aerospace sciences discussed in this review are basically non-topographic. The applications of the specialized photogrammetric techniques are usually constrained under some unique environments like vacuum chambers, high-pressure and cryogenic wind tunnel test sections and generally all with limited optical access. A typical photogrammetric system for such measurements includes cameras (video and scientific CCD cameras) and a computer for data reduction. Digital images are usually acquired and reduced with automated image processing in nearly real time, often on the same computer and often with many images in a sequence or set of sequences. Some of the specialized aerospace applications include aeroelastic wing deformation, wind tunnel model attitude/position, sting bending, model injection rates at blow-down wind tunnels, surface deformation of micro-air-vehicles, full-scale drop model trajectory and impact dynamics, and structural deformation of ultralight and inflatable large space structures.

A whole class of quantitative image-based flow diagnostic and visualization techniques in aerodynamics and fluid mechanics either use some form of photogrammetry or could benefit from its use. These image-based flow diagnostic techniques include pressure and temperature sensitive paints (PSP and TSP), Doppler global velocimetry (DGV), particle image velocimetry (PIV), particle tracking velocimetry (PTV), projection moiré interferometry (PMI), planar laser induced fluorescence (PLIF), laser-induced thermal acoustics (LITA), and oil-film interferometry for skin friction measurements. In fact, the geometrical relationship between the 3D object space and image plane is of fundamental importance for all the image-based techniques. For surface measurement techniques, photogrammetry provides the unique point correspondence between a surface and image when the equation of the surface is given, and therefore data extracted from images can be mapped onto a surface grid in the object space. The mapping procedure in PSP and TSP uses simpler resection methods that determine the camera exterior orientation parameters under an assumption that the interior orientation and lens distortion parameters are known [37,8,63,32]. Naughton and Liu [82] use photogrammetry to address both model curvature and camera perspective problems in oil-film interferometry for skin friction measurements, not only simplifying the requirements for measuring the geometric placements of the optical components, but also improving the measurement accuracy. Particle tracking velocimetry is based on photogrammetric intersection from multiple cameras to determine the position of each particle at two instants and further calculate its velocity [39]. Stereoscopic and tomographic particle image velocimetry uses either some special form of perspective projection transformation or certain empirical models to establish the relationship between the measurement domain and images [2].

Photogrammetry has proven to be a valuable tool in measurements of the surface profile and dynamical behavior of gossamer structure (ultra-low-mass space structure) both in ground and in-flight tests as an integral part of the design process [83–85,56,57]. Precise photogrammetric measurement of large structures supporting space technologies is well established. In particular, over the last few decades, measurements of large solar arrays and other structures have been conducted on various occasions as part of a flight experiments on the Space Shuttle [49]. A critical aspect of high-precision photogrammetry is the use of circular targets on the object under study although photogrammetric measurements can be performed using any discernible feature. Analysis of images of the object is performed to precisely determine the center of the targets, from which intersection can be performed to find the three-dimensional location of that target on the original object. This type of measurement performed on multiple targets can reveal the overall shape of the structure. Current practices for photogrammetric measurements of gossamer structures use attached retro-reflective targets, attached white diffuse targets, and white-light projected targets. A new projected-target-generating method based on laser-induced fluorescence has been developed [38], and it offers a distinct advantage over other target-generating methods since hundreds or thousands of targets are typically needed for surface measurements.

Following this introduction, in Section 2, the perspective projection transformation and models for cameras and lenses are discussed. In Section 3, the camera calibration/orientation methods are reviewed, which are key procedures in photogrammetric measurements. Although there are various camera calibration methods in photogrammetry and computer vision, the Direct Linear Transformation (DLT) and a closed-form resection solution are useful for initial estimation of the camera exterior orientation parameters. Then, an optimization method for full camera calibration/orientation from a single image of a three-dimensional target field is described in comparison with laboratory calibrations, which is particularly suitable for wind tunnel testing. Photogrammetric intersection is also discussed. The components of typical photogrammetric systems, including cameras, targeting, and software, are discussed in Section 4. The content in Section 5 focuses on photogrammetric measurements of wing deformation and model attitude in wind tunnels. Typical photogrammetric systems and their applications in large wind tunnels are described. Photogrammetric measurement uncertainty is discussed in Section 6. Special topics in Section 7 are smart wing deformation, in-flight aeroelastic deformation, determining loads from deformation, and dynamic aeroelastic deformation. A short account is given in Section 8 to discuss the role of photogrammetry in quantitative global flow diagnostic techniques like image-based velocimetry, pressure and temperature sensitive paints, and oil-film interferometry. Photogrammetric methods applied to vision-based autonomous aircraft landing are presented in Section 9. Photogrammetric measurements for gossamer space structures are described in Section 10, including measurement requirements and applications. The appendices provide some mathematical details on relevant technical aspects.

2. Perspective projection transformation and camera modeling

2.1. Collinearity equations

Photogrammetric measurements extract metric data in the three-dimensional (3D) object space from two-dimensional (2D) images. The collinearity equations provide the perspective projection relationship between the 3D coordinates in the object space and corresponding 2D coordinates in the image plane [110,77,80,67]. Camera calibration/orientation is required for quantitative image-based measurements to determine the camera interior and exterior orientation parameters, as well as the lens distortion parameters which supplement the collinearity equations. Fig. 2.1 illustrates the perspective projection relationship between the 3D coordinates (X,Y,Z) in the object space and

the corresponding 2D coordinates (x,y) in the image plane. The lens of a camera is modeled by a single point known as the perspective center denoted by (X_c, Y_c, Z_c) in the object space. Likewise, the orientation of the camera is characterized by three Euler orientation angles. The orientation angles and location of the perspective center are referred to in photogrammetry as the exterior orientation parameters. On the other hand, the relationship between the perspective center and the image coordinate system is defined by the camera interior orientation parameters, namely, the camera principal distance c and the photogrammetric principal-point location (x_p,y_p). The principal distance, which equals the camera focal length for a camera focused at infinity, is the perpendicular distance from the perspective center to the image plane, whereas the photogrammetric principal-point is where a perpendicular line from the perspective center intersects the image plane. Due to lens distortion, however, perturbation to the imaging process leads to departure from collinearity that can be represented by the shifts δx and δy of the image point from its 'ideal' position on the image plane.

The image and object-space coordinate systems are related through sequential rotational transformations, that is,

$$\begin{pmatrix} x-x_p-\delta x \\ y-y_p-\delta y \\ -c \end{pmatrix} = \lambda M(\kappa)M(\phi)M(\omega)\begin{pmatrix} X-X_c \\ Y-Y_c \\ Z-Z_c \end{pmatrix}, \tag{2.1}$$

where the rotation matrices are defined as

$$M(\omega)=\begin{pmatrix} 1 & 0 & 0 \\ 0 & \cos\omega & \sin\omega \\ 0 & -\sin\omega & \cos\omega \end{pmatrix}, \quad M(\phi)=\begin{pmatrix} \cos\phi & 0 & -\sin\phi \\ 0 & 1 & 0 \\ \sin\phi & 0 & \cos\phi \end{pmatrix},$$

$$M(\kappa)=\begin{pmatrix} \cos\kappa & \sin\kappa & 0 \\ -\sin\kappa & \cos\kappa & 0 \\ 0 & 0 & 1 \end{pmatrix} \tag{2.2}$$

The first rotation $M(\omega)$ is around the object-space coordinate X axis and the rotational vector is aligned with the X axis. The second rotation $M(\phi)$ is around a new object-space coordinate Y axis (after the first rotation) and the rotational vector is opposite to the Y axis. The third rotation $M(\kappa)$ is around a new Z axis (after the first and second rotations) and the rotational vector is aligned with the Z axis.

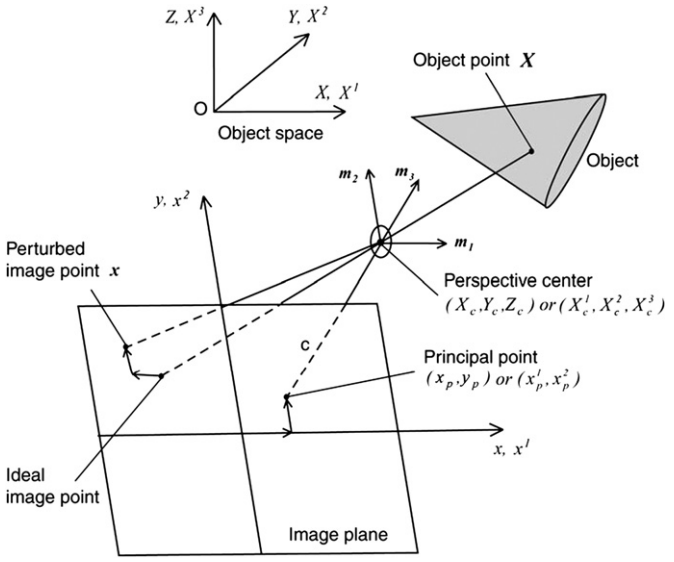

Fig. 2.1. Perspective projection from the 3D object space to the image plane.

Eliminating the scaling factor λ from Eq. (2.1) leads to the collinearity equations

$$\begin{aligned} x-x_p-\delta x &= -c\frac{m_{11}(X-X_c)+m_{12}(Y-Y_c)+m_{13}(Z-Z_c)}{m_{31}(X-X_c)+m_{32}(Y-Y_c)+m_{33}(Z-Z_c)} \\ y-y_p-\delta y &= -c\frac{m_{21}(X-X_c)+m_{22}(Y-Y_c)+m_{23}(Z-Z_c)}{m_{31}(X-X_c)+m_{32}(Y-Y_c)+m_{33}(Z-Z_c)}, \end{aligned} \tag{2.3}$$

where m_{ij} $(i, j=1, 2, 3)$ are the elements of the rotation matrix $\boldsymbol{M}=M(\kappa)M(\phi)M(\omega)=[m_{ij}]$ that are functions of the Euler orientation angles (ω,ϕ,κ),

$$\begin{aligned} &m_{11}=\cos\phi\ \cos\kappa, \quad m_{12}=\sin\omega\ \sin\phi\ \cos\kappa+\cos\omega\ \sin\kappa, \\ &m_{13}=-\cos\omega\ \sin\phi\ \cos\kappa+\sin\omega\ \sin\kappa, \quad m_{21}=-\cos\phi\ \sin\kappa, \\ &m_{22}=-\sin\omega\ \sin\phi\ \sin\kappa+\cos\omega\ \cos\kappa, \\ &m_{23}=\cos\omega\ \sin\phi\ \sin\kappa+\sin\omega\ \cos\kappa, \\ &m_{31}=\sin\phi, \quad m_{32}=-\sin\omega\ \cos\phi, \quad m_{33}=\cos\omega\ \cos\phi. \end{aligned} \tag{2.4}$$

The orientation angles (ω,ϕ,κ) are approximately the pitch, yaw, and roll angles of a camera in an established coordinate system. The image coordinate shifts δx and δy can be modeled by a sum of the radial and decentering distortions [45,47]

$$\delta x=\delta x_r+\delta x_d \quad \text{and} \quad \delta y=\delta y_r+\delta y_d, \tag{2.5}$$

where

$$\begin{aligned} \delta x_r &= K_1(x'-x_p)r^2+K_2(x'-x_p)r^4 \\ \delta y_r &= K_1(y'-y_p)r^2+K_2(y'-y_p)r^4, \\ \delta x_d &= P_1[r^2+2(x'-x_p)^2]+2P_2(x'-x_p)(y'-y_p), \end{aligned} \tag{2.6}$$

$$\begin{aligned} \delta y_d &= P_2\,[r^2+2(y'-y_p)^2]+2P_1(x'-x_p)(y'-y_p), \\ r^2 &= (x'-x_p)^2+(y'-y_p)^2. \end{aligned}$$

Here, K_1 and K_2 are the radial distortion parameters, P_1 and P_2 are the decentering distortion parameters, and x' and y' are the undistorted coordinates in the image plane.

Eq. (2.6) uses the photogrammetric principle point (x_p,y_p) as reference. The proper reference point to use is discussed in Section 2.4.1 if the lens optical axis is not perpendicular to the image plane. The 3rd-order radial distortion, which is the dominant term, can be either barrel $(K_1<0)$ or pincushion $(K_1>0)$ distortion as illustrated in Fig. 2.2. It is important to verify the sign convention for the distortion terms as sometimes the opposite sign convention to that presented here is used. For barrel distortion the image is displaced toward the point of symmetry, whereas for pincushion distortion the image is displaced away from the point of symmetry. Typical displacement vectors generated by lens distortion are shown in Fig. 2.3. Note that the 5th-order radial distortion K_2 term may have significant relative error after calibration due to its relatively small effect except for large image formats. The units of the radial distortion are m^{-2} and m^{-4} for the 3rd and 5th order distortions, respectively. When lens distortion is small, the unknown undistorted coordinates can be approximated by the known distorted

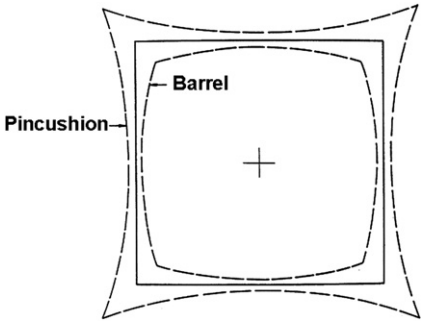

Fig. 2.2. Pincushion and barrel distortion of a square image.

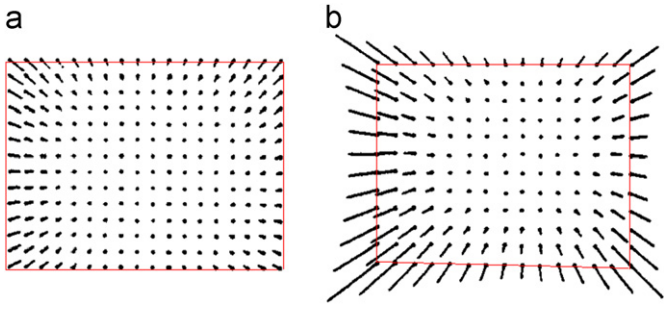

Fig. 2.3. Displacement vectors due to lens distortion, (a) barrel distortion ($K_1<0$), and (b) pincushion distortion ($K_1>0$). The solid rectangles in red represent the undistorted image plane coordinates.

coordinates, i.e., $x'\approx x$ and $y'\approx y$. For large lens distortion, an iterative procedure can be employed to determine the appropriate undistorted coordinates to improve the accuracy of estimation. The following iterative relations can be used: $(x')^0=x$ and $(y')^0=y$, $(x')^{k+1}=x+\delta x[(x')^k,(y')^k]$ and $(y')^{k+1}=y+\delta y[(x')^k,(y')^k]$, where the superscripted iteration index is $k=0,1,2\ldots$. The collinearity equations, Eq. (2.3), contain a set of the camera parameters to be determined by camera calibration; the parameter sets $(\omega,\phi,\kappa,X_c,Y_c,Z_c)$, (c,x_p,y_p), and (K_1,K_2,P_1,P_2) in Eq. (2.3) are the exterior orientation, interior orientation, and lens distortion parameters of a camera, respectively. The task of analytical camera calibration is to obtain the camera exterior, interior, and distortion parameters by solving the supplemented (with distortion) collinearity equations.

Note that the Euler angles ω, ϕ and κ have identical rotation matrices as the angles $\omega-\pi$, $\pi-\phi$ and $\kappa-\pi$ [101]. These two sets of the angles are simply alternate ways to arrive at the final correct orientation of a camera. Either angle set is equally valid even though the values for the three angles can appear quite different. This fact represents the duality of the rotation matrix. Thus, a transformation between the two equivalent sets of the rotation angles is given by $\omega'=\omega\pm\pi$, $\phi'=\pm\pi-\phi$, and $\kappa'=\kappa\pm\pi$. After the substitution of these angles into Eq. (2.4), the nine elements of the rotation matrix remain unchanged. It is desirable to compute the duality set of the angles and to restrict the angles to $[-\pi,\pi]$ in the $(\omega,\ \phi,\ \kappa)$ system. Note that the duality of the rotation matrix is not simply due to the cyclical nature of the trigonometric functions with additions of $\pm 2\pi$.

2.2. Alternative forms of collinearity equations

In some cases, the vector and index notations are more convenient for conciseness of expression [69]. In this section, the 3D object space coordinates (X,Y,Z) and the 2D image coordinates (x,y) are replaced by $X=(X^1,X^2,X^3)^T$ and $x=(x^1,x^2)^T$, respectively. The perspective projection transformation can be expressed in a vector form, i.e.,

$$\frac{x^1-x_p^1-\delta x^1}{-c}=\frac{\boldsymbol{m_1}\bullet(\boldsymbol{X}-\boldsymbol{X_c})}{\boldsymbol{m_3}\bullet(\boldsymbol{X}-\boldsymbol{X_c})}=\frac{\overline{X}^1}{\overline{X}^3}$$
$$\frac{x^2-x_p^2-\delta x^2}{-c}=\frac{\boldsymbol{m_2}\bullet(\boldsymbol{X}-\boldsymbol{X_c})}{\boldsymbol{m_3}\bullet(\boldsymbol{X}-\boldsymbol{X_c})}=\frac{\overline{X}^2}{\overline{X}^3}, \tag{2.7}$$

where the perspective center (or optical center) and the principal-point location in the image plane are given by $\boldsymbol{X_c}=(X_c^1,X_c^2,X_c^3)^T$ and $\boldsymbol{x_p}=(x_p^1,x_p^2)^T$, respectively. The vectors $\boldsymbol{m}_1=(m_{11},m_{12},m_{13})^T$ and $\boldsymbol{m}_2=(m_{21},m_{22},m_{23})^T$ are the directional cosine vectors parallel to the x^1-axis, x^2-axis in the image plane, respectively. The vector $\boldsymbol{m}_3=(m_{31},m_{32},m_{33})^T$ is normal to the image plane, with a direction from the principal point to the optical center along the optical axis. As shown in Fig. 2.1, the unit orthogonal vectors $\boldsymbol{m}_1$, $\boldsymbol{m}_2$, and $\boldsymbol{m}_3$ ($\boldsymbol{m}_i\bullet\boldsymbol{m}_j=\delta_{ij}$) constitute a local object space coordinate frame at the optical center $\boldsymbol{X_c}$. The coordinates $\overline{\boldsymbol{X}}=(\overline{X}^1,\overline{X}^2,\overline{X}^3)^T$ are the projections of the object space position vector $\boldsymbol{X}-\boldsymbol{X_c}$ in the $(\boldsymbol{m_1},\boldsymbol{m_2},\boldsymbol{m_3})$ frame. The scaling factor $\lambda=-c/\boldsymbol{m_3}\bullet(\boldsymbol{X}-\boldsymbol{X_c})$ is a ratio between the principal distance and the projected component of the object space position vector $\boldsymbol{X}-\boldsymbol{X_c}$ on the optical axis along $-\boldsymbol{m}_3$ direction. When a point $\boldsymbol{X}$ is on the focal plane $\boldsymbol{m}_3\bullet(\boldsymbol{X}-\boldsymbol{X_c})=0$, the scaling factor becomes infinite ($\lambda=\infty$), which corresponds to the points at infinity on the image plane.

In addition, Eq. (2.7) can be re-written in the homogenous image coordinates $\boldsymbol{x}_h=(x^1,x^2,1)^T$, i.e.,

$$\boldsymbol{x_h}=\lambda\boldsymbol{P}(\boldsymbol{X}-\boldsymbol{X_c}), \tag{2.8}$$

where the matrix $\boldsymbol{P}=[p_{ij}]=\boldsymbol{A}^{-1}\boldsymbol{M}$ describes the relationship between x_h and $\boldsymbol{X}-\boldsymbol{X_c}$, and $\boldsymbol{A}=[a_{ij}]$, defined as

$$\boldsymbol{A}=\begin{pmatrix}1 & 0 & -x_p^1-\delta x^1\\ 0 & 1 & -x_p^2-\delta x^2\\ 0 & 0 & -c\end{pmatrix}, \tag{2.9}$$

is related to the interior orientation parameters. A tensor form of Eq. (2.8) is $a_{ij}x_h^j=\lambda m_{ij}(X^j-X_c^j)$. Here, the Einstein convention for summation is used, and the tensor-form of the collinearity equations is sometimes convenient for mathematical manipulation. Another alternative form of the collinearity equations in the homogenous coordinates is $\boldsymbol{x_h}=\lambda\boldsymbol{P_hX_h}$, where $\boldsymbol{X_h}=(\boldsymbol{X}^1,\boldsymbol{X}^2,\boldsymbol{X}^3,1)^T$ is the homogenous object space coordinates, and $\boldsymbol{P_h}=\boldsymbol{A}^{-1}\boldsymbol{M_h}$ (3×4) is an extended matrix of $\boldsymbol{P}$, and $\boldsymbol{M_h}=(\boldsymbol{M}-\boldsymbol{MX_c})$ is the extended rotational matrix (3×4). Note that Eq. (2.8) is nonlinear due to the distortion terms and the scaling factor which varies throughout the field.

Furthermore, Eq. (2.7) can be re-written as a form suitable to least-squares estimation for the object space coordinates $\boldsymbol{X}$

$$\boldsymbol{W_1}\bullet(\boldsymbol{X}-\boldsymbol{X_c})=0\ \text{ and }\ \boldsymbol{W_2}\bullet(\boldsymbol{X}-\boldsymbol{X_c})=0, \tag{2.10}$$

where $\boldsymbol{W}_1$ and $\boldsymbol{W}_2$ are defined as $\boldsymbol{W_1}=(x^1-x_p^1-\delta x^1)\boldsymbol{m_3}+c\boldsymbol{m_1}$ and $\boldsymbol{W_2}=(x^2-x_p^2-\delta x^2)\boldsymbol{m_3}+c\boldsymbol{m_2}$. As shown in Fig. 2.4, the vector $\boldsymbol{W}_1$ is on the plane spanned by the orthogonal unit vectors $\boldsymbol{m}_1$ and $\boldsymbol{m}_3$, while $\boldsymbol{W}_2$ is on a plane spanned by $\boldsymbol{m}_2$ and $\boldsymbol{m}_3$. Geometrically, Eq. (2.10) describes two planes normal to $\boldsymbol{W}_1$ and $\boldsymbol{W}_2$, defining an intersection line of the two planes through the optical center $\boldsymbol{X_c}$. For a given image point $\boldsymbol{x}=(x^1,x^2)^T$, Eq. (2.10) is not sufficient to determine the object space point with the three unknown coordinates $\boldsymbol{X}=(X^1,X^2,X^3)^T$. Hence, extra equations associated with additional cameras and other geometrical constraints should be added to find a unique least-squares solution of $\boldsymbol{X}$. The collinearity equations contain the exterior orientation parameters $(\omega,\phi,\kappa,X_c^1,X_c^2,X_c^3)$, interior orientation parameters (c,x_p^1,x_p^2) and are supplemented with the lens distortion parameters (K_1,K_2,P_1,P_2).

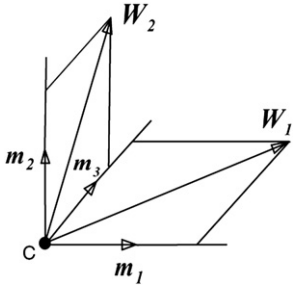

Fig. 2.4. Relationship between the vectors $\boldsymbol{m_i}$ and $\boldsymbol{W_j}$.

2.3. Notes on collinearity equations

It is common to mix units in photogrammetric computations. For example, x, y, c, x_p, and y_p can be in one consistent set of units (typically mm), while X, Y, Z, X_c, Y_c, and Z_c can be in another consistent set of units (typically meters or inches). This is clearly illustrated in Eq. (2.7). As long as the length units are consistent for the left-hand and right-hand side in Eq. (2.7), respectively, the correct relationship is preserved. Note that if one chooses to use pixels as the unit of length for the image data, then one would need to use pixels for the principal distance and principal point as well. The more typical choice of mm for units of length in the image is largely due to the almost universal practice of using mm to denote the focal length of lenses.

It is useful to consider the collinearity equations when the Euler angles are all set to zero. The rotation matrix then becomes the identity matrix consisting of a diagonal matrix of ones. If the collinearity equations are further simplified by setting x_p and y_p at zero and X_c and Y_c at zero, the equations are reduced to $x=-cX/Z_c=X\ mag$ and $y=-cY/Z_c=Y\ mag$, where $mag=-c/Z_c$ is a magnification factor. This illustrates that for this simplified geometry where the object space motion at $Z=0$ is parallel to the image plane, the object-to-image relationship is governed by the magnification factor only. In fact, this directly corresponds to Eq. (2.7) in the ($\boldsymbol{m}_1$, $\boldsymbol{m}_2$, $\boldsymbol{m}_3$) frame.

The standard Gaussian object-image relationship, $1/f=1/o+1/i$, can be used to estimate the principal distance c if the image distance i in the equation is replaced with c and the object distance o at which the lens is focused is known. For example, if $f=25$ mm and the lens focal setting is adjusted for $o=60$ in, a reasonable estimate for c is 25.42 mm. In order to obtain proper focus at 60 in the lens is translated about 0.42 mm away from the image sensor. The correct principal distance to use when the 25-mm focal length lens is focused on an object distance of 60 in is 25.42 mm. Note that the Gaussian object–image relationship only applies for the particular distance at which the lens is focused. This object distance is not necessarily where a given target in a 3D object field might lie. This relationship does not apply throughout the object field, and it only holds for a particular object distance. For instance, if the 25 mm focal length lens in the above example were focused on infinity, the correct principal distance to use would be 25 mm for all object distances, not just for objects far away. Likewise if the lens happened to be focused at 60 in then the correct principal distance to use for all object distances (even if not located at 60 in) would be the value of 25.42 mm that we found above. The magnification is, in general, a function of the object field location given by the ratio of the distance from the rear perspective center to the image point divided by the distance from the front perspective center to the object point.

2.4. Misaligned image plane

2.4.1. Reference symmetry point

The correct reference point to use for the lens distortion is the principal point (x_p, y_p) only if the optical axis of the lens is perpendicular to the image plane. If the image plane is tilted (for instance as can occur with small format non-metric cameras), the point of symmetry for distortion (x_s, y_s), which essentially locates the optical axis of the lens, is the correct reference point to be used for distortion (see Fig. 2.5). However, some calibration methods such as the bundle adjustment or optimization cannot effectively separate the two points and thus use a single point that is carried in the solutions and calibrations labeled as the principal point. If no radial distortion is present, the single reference point found by bundle adjustment or optimization will be essentially the principal point. If the distortion is present, however, the single reference point found by bundle adjustment or optimization will be due to the combined effect of (x_p, y_p) and (x_s, y_s), depending on the relative influence of the imaging portion [correctly referenced to (x_p, y_p)] or the influence of the distortion [correctly referenced to (x_s, y_s)]. In general, if there is little distortion and/or the lens is well aligned, (x_p, y_p) is an adequate reference point for distortion. If not, the point of symmetry (x_s, y_s) should be used if available. Most textbooks use (x_p, y_p) as the reference for lens distortion, which implicitly assumes an untilted lens.

2.4.2. Lens–image misalignment relationship

For an ideally constructed lens, all centers of curvature of the various lens surfaces that make up the lens are assumed aligned along a common axis referred to here as the optical axis of the lens. Such a perfectly constructed lens with the optical axis perpendicular to the image plane would have no decentering

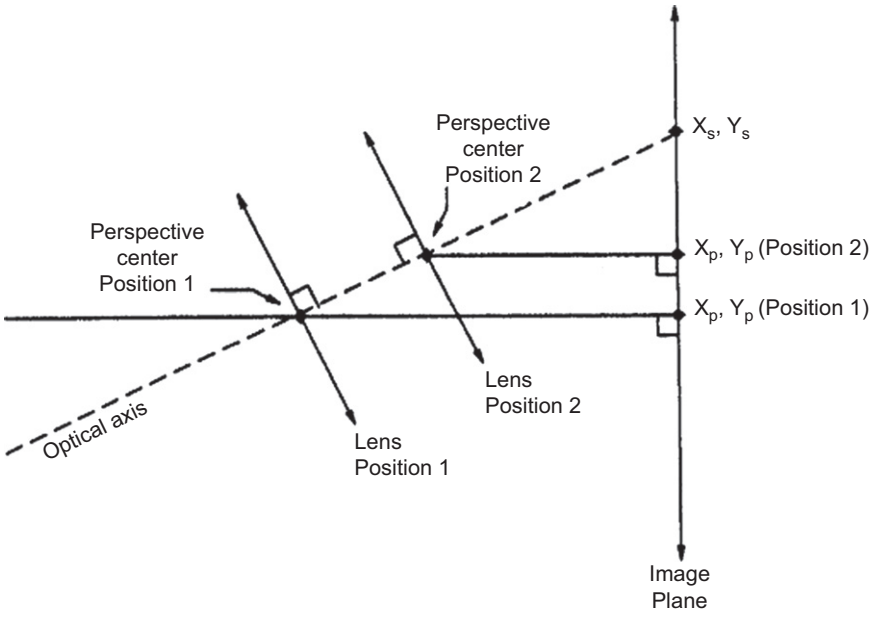

Fig. 2.5. Principal point (x_p,y_p) and point of symmetry (x_s,y_s) for zoom lens with tilted image plane.

distortion, but might still suffer from radial distortion. For the perfectly constructed lens, the undistorted image plane coordinates are given by the intersection in the image plane of a ray from a given object point which enters the lens at the front perspective center and exits the lens at the rear perspective center on its way toward the image plane. This relationship is described with the collinearity equations. Radial distortion is considered to be a function only of the undistorted image coordinates on the image plane which is perpendicular to the optical axis and therefore, with this model, the radial distortion would not vary with the object distance for a fixed principal distance.

For a misaligned image plane and ideally constructed lens, the photogrammetric principal point used in the imaging relationship (collinearity) is not located at the intersection of the optical axis with the image plane, but rather at the intersection of a perpendicular line from the rear perspective center to the image plane. Instead, the intersection of the optical axis with the image plane locates the proper point of symmetry to be used in the computation of distortion corrections. The variation of the location of the principal point, (x_p,y_p), as the lens is shifted along the optical axis (mimicking a zoom lens) is depicted in Fig. 2.5. For zoom lenses, the variation in the principal point as a function of zoom setting (varying principal distance) is often linear. The point of symmetry (x_s,y_s) remains fixed while the principal point, being defined as the foot of the perpendicular line to the image plane from the rear perspective center, varies with zoom setting. Fig. 2.6 illustrates the displacement vectors associated with the variation of lens distortion at different zoom settings.

In analytical self-calibration, only one photogrammetric principal point can generally be solved for. If the radial distortion is zero, this single point will correspond to the principal point, even if the image plane is misaligned. For a misaligned image plane when radial distortion is present, the single point found will approximate the principal point, but may have some additional error due to competition in the solution between imaging and distortion. This is because imaging is properly referenced to the principal point, whereas lens distortion is properly referenced to the point of symmetry. When comparing image coordinates of an aligned and a misaligned image plane there will be an "apparent" distortion that is analogous to the "apparent" distortion between two images (neither of which suffers any lens distortion) of an object from different perspectives.

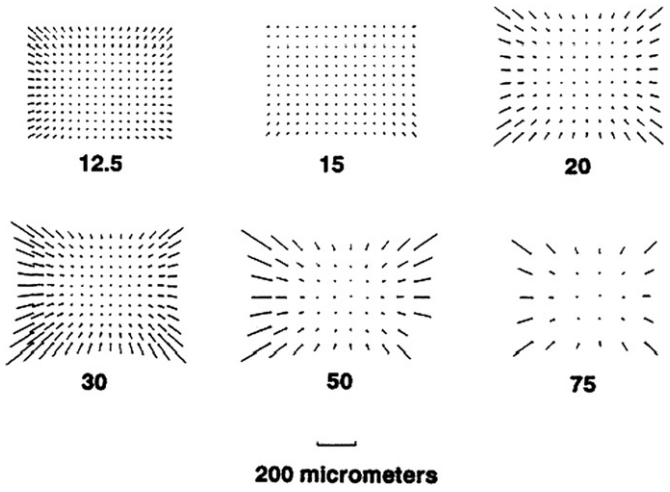

Fig. 2.6. Distortion of a zoom lens as a function of zoom setting (focal length).

3. Camera calibration/orientation and intersection

Camera calibration/orientation is a key element of photogrammetric or videogrammetric measurements. Analytical camera calibration/orientation techniques have been used to solve Eq. (2.3) for the determination of the interior and exterior orientation parameters and lens distortion parameters of the camera/lens system [52,45,95,106]. The term 'camera calibration' generally refers to the determination of the interior orientation parameters, while the term 'camera orientation' generally refers to the determination of the exterior orientation parameters. Camera calibration and orientation are often combined with the simultaneous determination of target coordinates in a 'bundle-adjustment' solution to the collinearity equations, given appropriately diverse views of the object of interest from a large number of images. Since the collinearity equations coupled with additional parameters for lens distortion are non-linear, the iterative method of least-squares estimation has been used as a standard technique for the solution of the collinearity equations in photogrammetry. However, direct recovery of the interior orientation parameters including (c,x_p,y_p) is often impeded by inversion of a singular or ill-conditioned normal equation matrix that mainly results from strong correlation between the exterior and interior orientation parameters. In order to reduce the correlation between these parameters and enhance the determinability of (c,x_p,y_p), Fraser [46,45] suggested the use of multiple camera stations, varying image scales, different camera roll angles and a well-distributed target field in three dimensions. These schemes for selecting suitable calibration geometry could improve the properties of the normal equation matrix.

For most aerospace applications where optical access and preparation time are limited and cameras are usually fixed, however, a simple single-image method of camera calibration is desirable that has a minimum impact on productivity and is less time consuming than other calibrations [67]. In Appendix A, the Direct Linear Transformation (DLT) method and a closed-form resection solution given by Zeng and Wang [111] are briefly described, which are useful for initial estimation of the exterior orientation parameters of a camera based on a number of known targets. An optimization method for comprehensive camera calibration developed by Liu et al. [67] is also described, which can determine the exterior orientation, interior orientation and lens distortion parameters (as well as the pixel aspect ratio of a CCD array) from a single image of a known 3D target field. The optimization method, combined with the DLT, allows automatic camera calibration without an initial guess of the orientation parameters. Camera calibration methods used in computer vision have been reviewed and evaluated by Salvi et al. [97].

3.1. Initial estimation

The DLT, originally proposed by Abdel-Aziz and Karara [1], can be very useful to determine approximate values of the camera parameters. In Appendix A, the DLT equations are obtained by rearranging the terms in the collinearity Eq. (2.3), where the DLT parameters are related to the camera exterior and interior orientation parameters [77]. Unlike the standard collinearity equations, the DLT equations are linear when the lens distortion terms are neglected. In fact, the DLT is a linear treatment of what is essentially a non-linear problem at the cost of introducing two additional parameters. Without using an initial guess, a linear least-squares solution can be directly obtained. Because of its simplicity, the DLT is widely used in both non-topographic photogrammetry and computer vision. When the lens distortion cannot be ignored, however, iterative solution methods are still needed and as a result the DLT loses its simplicity. In general, the

DLT can be used to obtain fairly good values of the exterior orientation parameter and the principal distance, although it gives a poor estimate for the principal-point location. Therefore, the DLT is valuable since it can provide initial approximations for more accurate methods like the optimization method discussed below for comprehensive camera calibration. In general, the DLT needs at least six targets and it is not appropriate for a planar/near-planar target filed. In addition, as shown in Appendix A, the closed-form resection solution given by Zeng and Wang [111] based on three points is useful for an initial estimation of the exterior orientation parameters.

3.2. Optimization method

To deal with the singularity problem in solving the collinearity equations, the optimization method developed by Liu et al. [67] is based on the following insight. Strong correlation between the interior and exterior orientation parameters leads to the singularity of the normal-equation-matrix in a least-squares method for a complete set of the camera parameters. Therefore, to eliminate the singularity, a least-squares method is used for the exterior orientation parameters only, while the interior orientation and lens distortion parameters are calculated separately using an optimization scheme. As shown in Appendix A, this optimization method contains two separate interacting procedures: resection for the exterior orientation parameters and optimization for the interior orientation and lens distortion parameters. It is noted that direct optimization in the whole parametric space (14 parameters) often converges to an inaccurate result due to the complicated topology in the high-dimensional space, depending on initial values and perturbations. A practical alternative is to decompose the high-dimensional space into smaller subspaces and solve the optimization problems interactively with different methods in these subspaces. Naturally, the parametric space can be decomposed into the exterior orientation parameters (six parameters) and the interior orientation parameters plus the lens distortion parameters and pixel-spacing-aspect ratio (a total of eight parameters).

The objective function for minimization is the standard deviation of the estimated interior orientation parameters on a 3D target field such as std(x_p) that has a simple topological structure near the global minimum point. In other words, the optimization problem is to seek the correct values of the interior orientation parameters by minimizing the objective function. A 3D field of targets on a step configuration is simulated as shown in Fig. 3.1. A typical topological structure of std(x_p) is shown in Fig. 3.2 near the global minimum point (c,x_p,y_p)=(28,0.2,0.08) mm for simulated image of the target field. Clearly, near the global minima

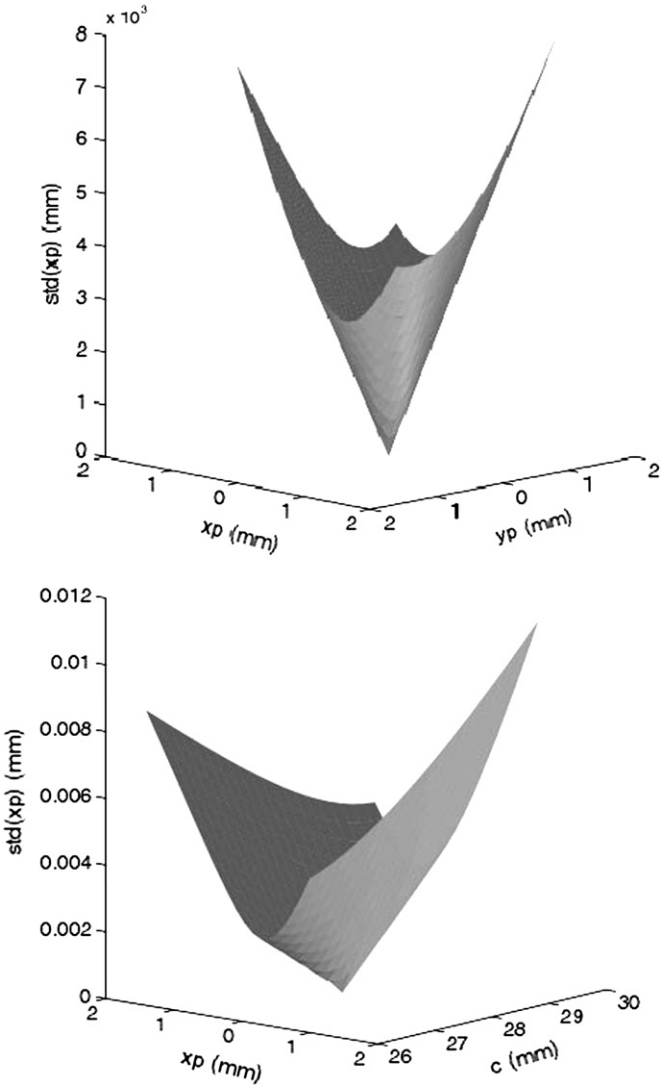

Fig. 3.2. Topology of the objective function near the minimum point (c, x_p, y_p)=(28, 0.2, 0.08) (mm).

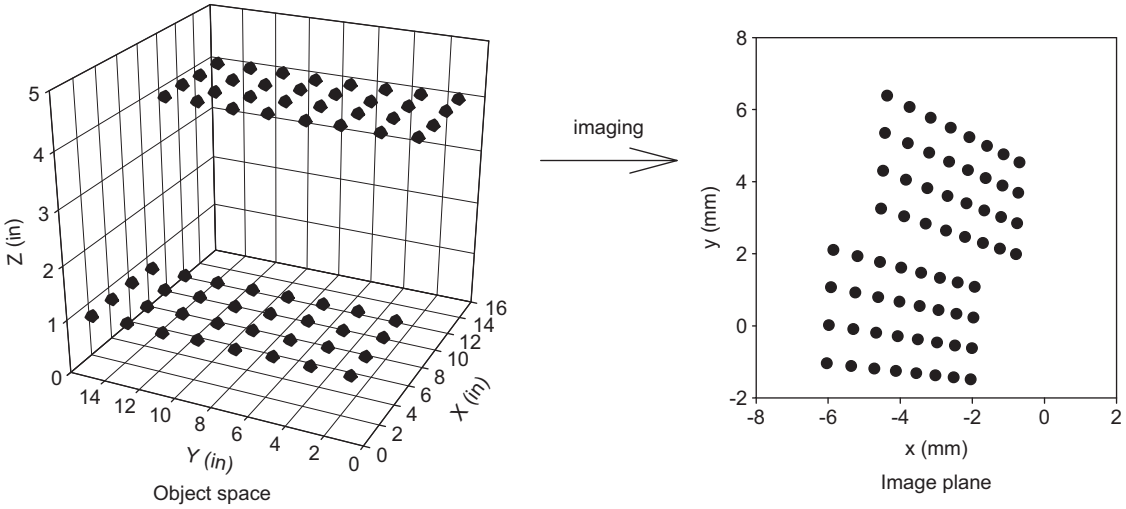

Fig. 3.1. Target field on a step configuration and its image.

std(x_p)=0, std(x_p) exhibits a single "valley" structure such that the optimization problem is well defined.

Generally, the topological structure of std(x_p) is affected by the three-dimensionality of the target field. For the step target field, the step height H characterizes the three-dimensionality. Fig. 3.3 shows the topological structures of std(x_p) for $H=6$ and 2 in. Note that the two surfaces are partially in contact. Evidently, the stronger three-dimensionality of the target field with a larger H produces a steeper "valley" in topology. From a standpoint of optimization, the stronger three-dimensionality leads to faster convergence. Fig. 3.4 shows effect of the three-dimensionality (step height H) on convergence of the principal distance in the optimization solution. The similar behavior of convergence is observed for the other parameters. Clearly, the strong three-dimensionality of the target field improves convergence rates. For a planar field of targets ($H=0$), the optimization method does not generally converge to the true values. Hence, the optimization method requires a 3D target field.

The topological structure of std(x_p) or std(y_p) can also be affected by random disturbances on the targets. To simulate this effect, the target coordinates in the image are disturbed by mathematically adding a zero-mean random disturbance with a Gaussian distribution. Fig. 3.5 shows the topological structures of std(x_p) at disturbance levels of 1 μm and 6 μm (these disturbance levels correspond to 0.08 and 0.46 pixel for a typical CCD video camera system). The flattening of the sharp "valley" near the minimum point in Fig. 3.5 implies that noise in the image leads to a slower convergence rate and produces larger errors in the optimization computations. Fig. 3.6 shows typical errors of the interior orientation parameters (c, x_p, y_p) as functions of the disturbance level, where the correct simulated values of (c, x_p, y_p) are (28, 0.2, 0.08) (mm). For a typical CCD video camera, for example, the random error in the target centroid measurement is usually less than 0.3 μm (0.023 pixel). Thus, the corresponding predicted precision error in the estimated values of (c, x_p, y_p) by the optimization method is no more than 0.02 mm. Besides

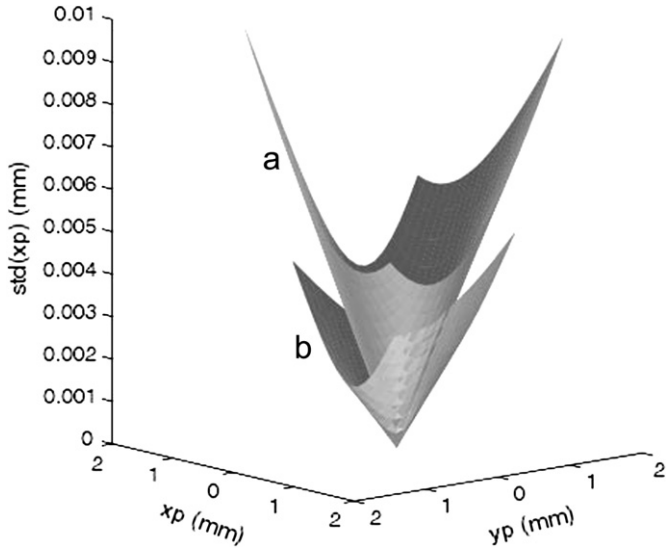

Fig. 3.3. Effect of three-dimensionality (step height H) on topology of the objective function near the minimum point, (a) $H=6$ in, (b) $H=2$ in.

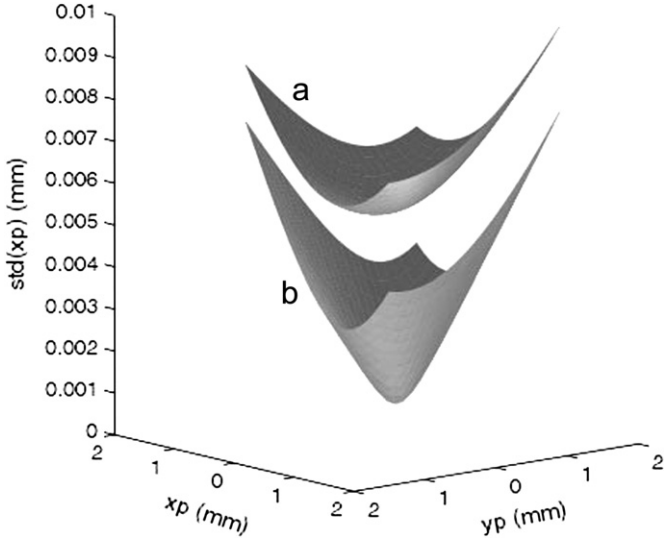

Fig. 3.5. Effect of disturbance in image plane on topology of the objective function near the minimum point, (a) disturbance level of 6 μm; (b) disturbance level of 1 μm.

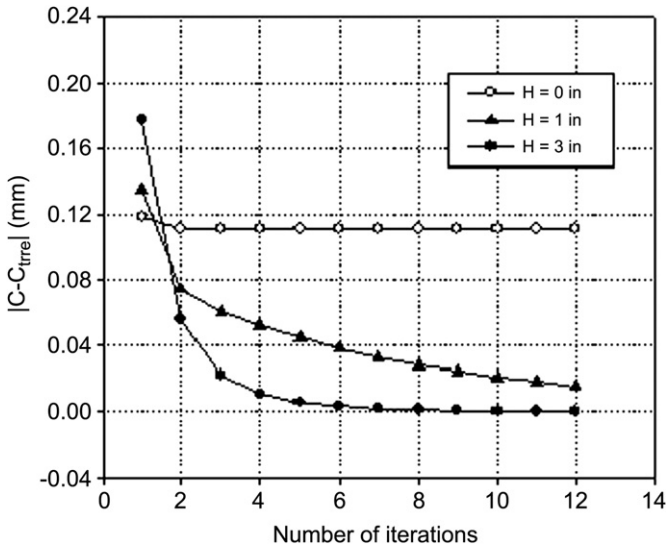

Fig. 3.4. Effect of three-dimensionality (step height H) on convergence of the principal distance in the optimization solution.

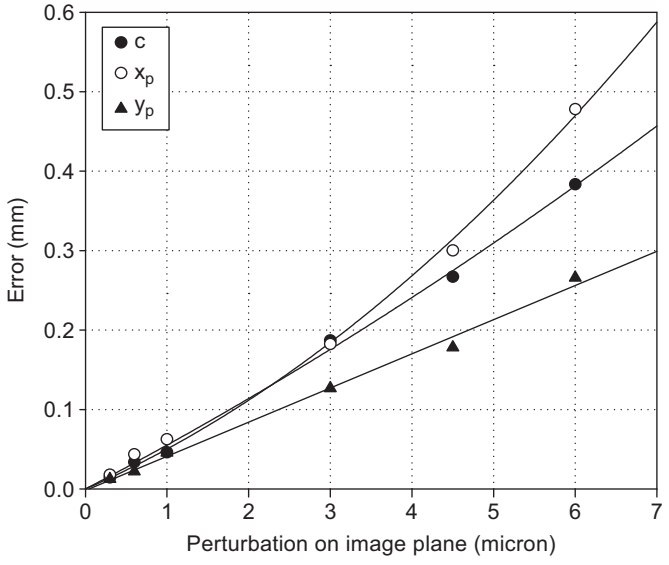

Fig. 3.6. Errors in the interior orientation parameters as functions of disturbance level.

std(x_p), other appropriate objective functions may also be used. An obvious choice is the root-mean-square (rms) of the residuals of calculated object space coordinates of all targets. In fact, it is found that these objective functions are qualitatively equivalent in the optimization problem.

3.3. Laboratory calibration

In order to evaluate the accuracy of the optimization method, camera calibrations for an Hitachi CCD camera with a Sony zoom lens (12.5 to 75 mm focal length) and an 8 mm Cosmicar television lens were made in a NASA Langley laboratory. The measurement system consisted of a CCD camera, a personal computer with a Matrox Pulsar frame-grabber board, a step target plate, and software. A target-tracking program was used to track targets and compute target centroids [66]. The CCD array size of the Hitachi camera was 8 mm by 6 mm. The digitized image size was 640 by 480 pixel with vertical and horizontal pixel spacings equal to 13.0 μm and 12.9 μm, respectively. The random error in the measurement of target centroids was less than 0.3 μm (0.023 pixel). The 3D target field for camera calibration was provided by a three-step target plate with 54 circular retro-reflective targets of 0.5 in diameter, a 2.0 in step height H and 2.0–in spacing between neighboring targets (see Fig. 3.7). The coordinates of the targets on the plate were measured *a priori* with a three-dimensional coordinate machine with an accuracy of 0.001 in.

For comparison, optical techniques described by Burner et al. [17], were also used for calibration. The laser-illuminated, displaced-reticle technique was used to determine the horizontal and vertical pixel spacing. The principal-point location was found by the unexpanded, laser-illumination technique, and the lens distortion parameters were determined from images of a calibration plate suitably aligned with the camera axis. Fig. 3.8 shows the principal distance given by the optimization method versus zoom setting for the Sony zoom lens. Fig. 3.9 shows the principal-point location and radial distortion coefficient K_1 as a function of the principal distance for the Sony zoom lens. The error bars in the principal-point location are determined based on replication calibration data using the optimization method collected at different camera roll angles and positions over two days. The results obtained by the optimization method are in reasonable agreement with those given by Burner [18] using the optical techniques for the same lens. The optimization method was also used to calibrate the Hitachi CCD camera with an 8 mm Cosmicar television lens. Table 3.1 summarizes the calibration results for the Hitachi CCD camera with 8 mm Cosmicar TV lens. The interior orientation and lens distortion parameters obtained by the optimization method are consistent with those obtained by the optical techniques. The accuracy of camera calibration is usually represented by the residual of the image coordinate calculation. Typically, the optimization method has a residual of 1 μm or less

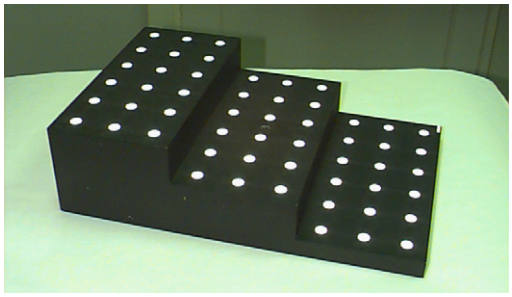

Fig. 3.7. Step calibration target plate.

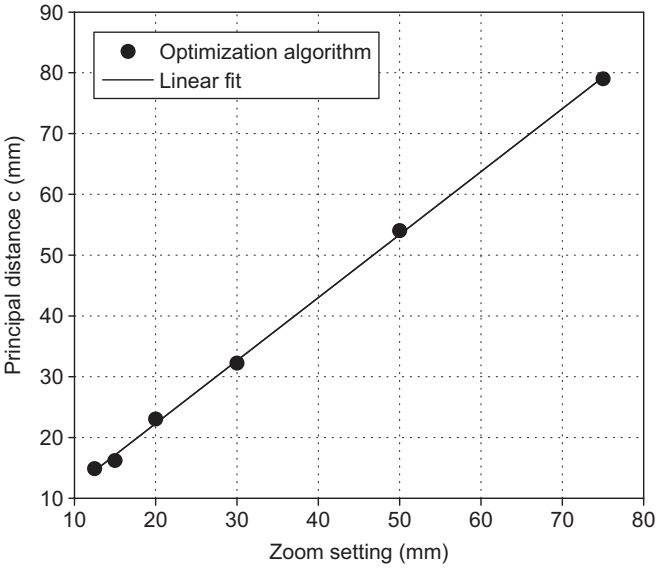

Fig. 3.8. Principal distance vs. zoom setting for a Sony zoom lens.

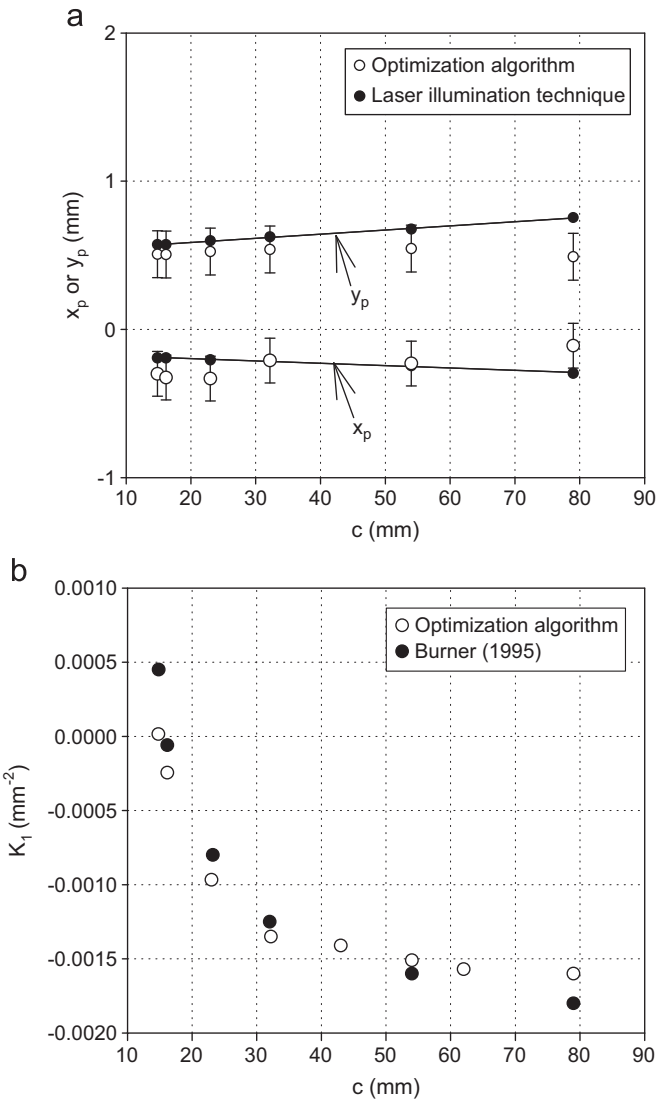

Fig. 3.9. (a) Principal-point location and (b) radial distortion coefficient as a function of the principal distance for a Sony zoom lens connected to an Hitachi camera with an 8 mm by 6 mm CCD array.

Table 3.1
Calibration for Hitachi CCD camera with 8 mm Cosmicar TV lens.

Interior orientation	c (mm)	x_p (mm)	y_p (mm)	S_h/S_v	K_1 (mm^{-2})	K_2 (mm^{-4})	P_1 (mm^{-1})	P_2 (mm^{-1})
Optimization	8.133	−0.156	0.2014	0.99238	0.0026	3.3×10^{-5}	1.8×10^{-4}	3×10^{-5}
Optical techniques	8.137	−0.168	0.2010	0.99244	0.0027	4.5×10^{-5}	1.7×10^{-4}	7×10^{-5}

in the image plane for an 8 mm by 6 mm CCD array, depending on the accuracy of the coordinates of the target plate.

3.4. Bundle method

The bundle method originally developed by Brown [15] provides simultaneous consideration of all sets (or 'Bundles') of photogrammetric rays from all cameras. Referring back to the collinearity equations, Eq. (2.3), a configuration of m cameras imaging n points will yield a total of $2m\times n$ equations if all points can be seen in all images. Here, it is assumed that the interior parameters (c, x_p, y_p) and the lens distortion parameters are known through calibration for all cameras. There are the six unknown exterior parameters (ω,ϕ,κ, X_c, Y_c, Z_c) of the collinearity equations for each camera and three unknown coordinates (X, Y, Z) for each point. The total number of the unknowns is $6m+3n$. To determine a unique solution for both the exterior orientation parameters and coordinates, the inequality $2m\times n\geq 6m+3n$ should hold. Thus, the number of cameras required for the bundle method is related to the number of points by $m\geq 3n/(2n-6)$. When $n\geq 12$ (more than 12 points), two cameras are sufficient to determine the coordinates of the points. Nevertheless, more cameras will lead to a more accurate solution.

Intuitively one can see that for even a small number of cameras and a modest number of points the resulting number of equations can add up to hundreds, if not thousands. Fortunately, a least squares adjustment method will produce a much smaller set of the normal equations. But, even the number of normal equations can be large for many projects with hundreds of points, though it is possible through matrix manipulation to reduce the order of the 'reduced' normal equations to $6m$, where m is the number of images. The bundle adjustment algorithm [16] first solves for the exterior orientation parameters as unknowns and then computes the object point coordinates (X, Y, Z) essentially through a spatial intersection approach. Initial estimate of the exterior orientation parameters can be given using the closed-form resection solution [111] based on three control points that establish the reference coordinate system. Then, the coordinates of all the points are determined by the photogrammetric intersection method. An iteration scheme can be applied to reduce the residual of least-squares estimation.

3.5. Photogrammetric intersection

Given the camera interior and exterior orientation and lens distortion parameters, the object-space coordinates (X^1, X^2, X^3) or (X, Y, Z) can be obtained by solving the collinearity equations when a pair of the corresponding image points is identified in two or multiple images. This procedure is photogrammetric intersection. In the case where only a single camera can be utilized, some geometrical constraint such as one fixed coordinate should be used in order to obtain a unique solution for the object-space coordinates. Therefore, establishing the point correspondence between two or multiple images for the same physical point in the object space is essential to intersection. This is the point correspondence problem in 3D vision. Any given point in the image 1 corresponds to an epipolar line in the image 2 that is a projection of a line connecting the object-space point and the image point through the optical center of the camera 1 onto the image 2. As indicated in Appendix B, the fundamental matrix the Longuet-Higgins equation maps a point in the image 1 to its epipolar line in the image 2 and vice versa. For two calibrated cameras, the epipolar lines in two images can be directly determined from the collinearity equations. The Longuet-Higgins equation indicates that a point in the image 1 corresponds to its epipolar line on the image 2 and vice versa. Therefore, the point correspondence is not uniquely established between two images. To establish the point correspondence between images, at least four cameras (or four images) are needed. In many aerospace applications, the number of targets is not large such that the point correspondence between images can be manually determined. The point correspondence and intersection are further discussed in Appendix B.

4. Typical photogrammetric systems

A typical photogrammetric or videogrammetric measurement system for aeroelastic deformation of wings and bodies in wind tunnel testing includes CCD cameras, computer with an image acquisition frame grabber board, illuminating lights, and targets distributed on a model. Due to the limited optical access in production wind tunnels, photogrammetric methods based on multiple images taken at different positions and angles are often difficult or impossible to deploy. Therefore, photogrammetric systems for wind tunnels may utilize non-optimal geometries consisting of a limited number of cameras (and in some cases may be limited to only one camera). Fig. 4.1 shows schematics of a single-camera and two-camera videogrammetric model deformation (VMD) measurement systems for wind tunnel testing. The sub-components of the photogrammetric system are described below. Burner et al. [24] compared photogrammetric techniques with other optical techniques for measuring model deformation in wind tunnels such as projection moiré interferometry and the commercially available Optotrak^{TM} RH2020 system. It is found that no one technique is best for all applications or facilities. The techniques are also not necessarily mutually exclusive and in some cases can be complementary to one another.

4.1. Cameras

4.1.1. Still cameras

For many years the only cameras used for photogrammetry were large format metric cameras [80]. A camera is deemed metric if both its internal geometry and the distortion characteristics of the lens are repeatable, stable and amenable to modeling via parameters that can be estimated accurately through the process of photogrammetric calibration. The state of the art in metric cameras is represented by the INCA series of digital cameras [see Fig. 4.2(a)] from Geodetic Services, Inc (GSI). In 1991, Kodak introduced the DCS100 and immediately changed the 'metric' playing field with its high resolution (1524 by 1028) CCD sensor packaged in a standard 35 mm SLR camera. The latest release in the DCS family, the PRO SLR has made a significant leap in resolution and available features with the current model supporting a 14 megapixel CMOS imager [see Fig. 4.2(b)].

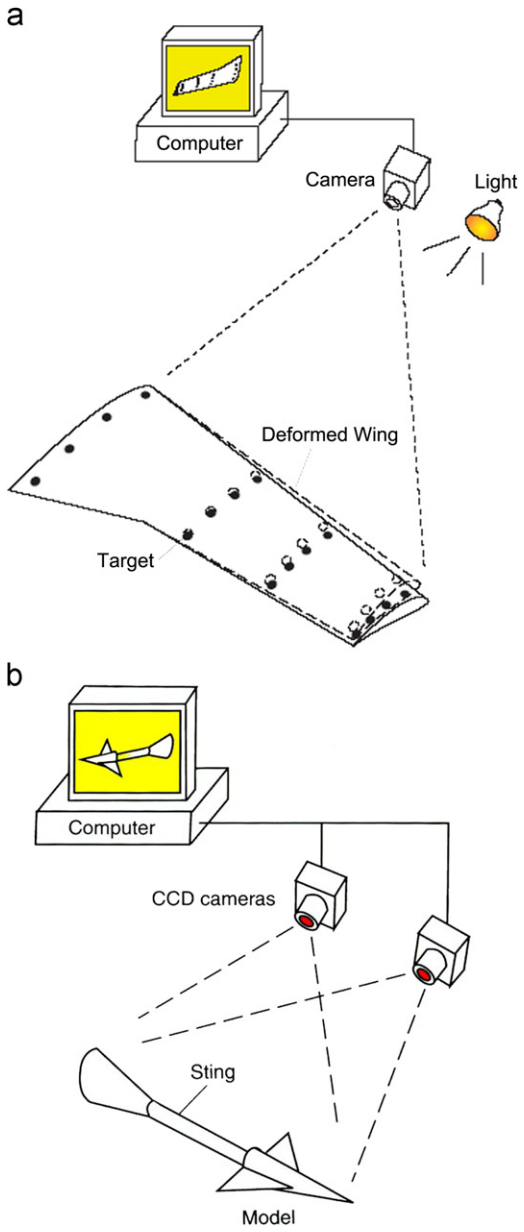

Fig. 4.1. Schematic of (a) single-camera system and (b) two-camera system.

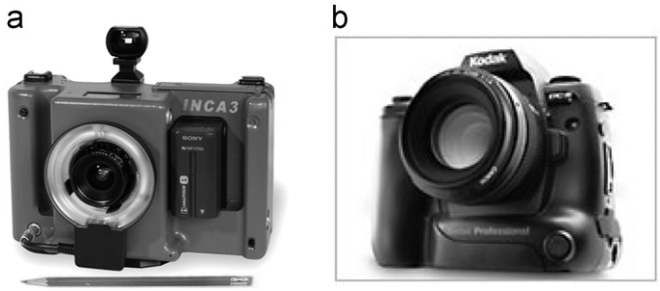

Fig. 4.2. (a) INCA3 metric camera from Geodetic Services (GSI), (b) Kodak DCS760 6 megapixel digital SLR camera.

The DCS family, while widely supported by photojournalists, has been also been adopted by photogrammetrists in various applications such as aerospace tool verification, the measurement and monitoring of large engineering structures and architectural recording [102].

Traditionally, photogrammetry is carried out by moving a single still camera around a rigid structure taking photographs from many observations angles. Although this approach can be used for static measurement of structures, it is more common for aerospace testing to position a number of remotely triggered cameras in fixed locations around the structure. This allows for dynamic recording if the framing rate is sufficient and the cameras are properly synced.

4.1.2. Video cameras

The modern CCD digital video camera, several examples of which are shown in Fig. 4.3, has also found application in the photogrammetric field. While the predecessors of the these cameras offered low resolution, typically (640 by 480 pixel), and found limited applications in photogrammetry, the current range of CCD video camera systems, in terms of features, quality, number of manufacturers and cost, is enormous and many have photogrammetric potential. In videogrammetry systems, the images obtained from the video cameras are generally passed directly to a host personal computer (PC) for storage and processing. A frame grabber is typically designed to reside in the host computer and provide the interface between the video camera and the computer. The frame grabber under software control can adjust camera settings and continuously read the video output of the camera, and in some cases carry out real time processing tasks. In the case of multi-camera systems the frame grabber may provide process synchronization, a critical aspect in recording images as part of dynamic analysis. A more detailed discussion of the functionality of frame grabbers is provided by Shortis and Beyer [102].

Unlike studies of static structures, studies of dynamic behavior must be performed with an array of fixed cameras because the frame acquisition of all cameras must be synchronized to avoid a change in the structure occurring between image acquisitions across all camera locations. Usually still cameras have insufficient framing rates to effectively measure the motion in dynamic studies, necessitating the use of video cameras. Although video cameras have a much higher frame rate than still cameras, the limited bandwidth for image readout, frame grabbing, and storage introduces an image resolution to frame rate trade off. Digital video technology is improving rapidly, and manufactures are offering frame grabbers based on the PCI-X technology that promises peak transfer rate speeds between the frame grabber and the host of 800 MB/s.

This issue of video camera synchronization is important in many studies of dynamic behavior, and the choice of video camera can be critical. With analog video cameras it is common to configure one of the cameras as a master camera, which operates in a free-run mode

Fig. 4.3. Examples of modern CCD digital video cameras.

at its internal frame rate. All of the remaining cameras are configured as slave cameras and are required to synchronize their video clocks to the master camera's video signal, thereby ensuring commonality for the integration time of all cameras. In recent times, however, digital video cameras have supplanted analog cameras because of their significantly higher quality and better suitability for videogrammetry.

Digital video cameras usually have an asynchronous reset input that can be used to synchronize their integration periods. However, some cameras do not respond immediately to their asynchronous reset trigger signal and instead internally align this trigger signal with some internal clock event (such as the horizontal line clock). Such internal trigger signal clock alignment can lead to jitter between the integration periods between the cameras (of up to 60 μs for a 16 kHz horizontal clock), which may be significant in some applications. Hence, depending on the application, it may be important to choose a camera with a true asynchronous reset.

4.2. Targets and lighting

4.2.1. Targets on wind tunnel models

Targets are placed on a model surface at locations where deformation measurements are desired. As shown in Fig. 4.4(a), for a single-camera VMD measurement system in a wind tunnel, targets should be placed in rows on the wing at known spanwise location in order to obtain a solution of the collinearity equations with two equations for two unknowns (X, Z). Both retro-reflective targets and white diffuse polished paint targets, as shown in Fig. 4.4(b), have been used. The retro-reflective targets yield a high contrast image when a light source is placed near the camera and are the targets of choice if aerodynamic considerations will allow the additional thickness and roughness. The white diffuse polished paint targets require a dark background to achieve high contrast. Dark surfaces seen in reflections from highly polished metal models produce sufficient contrast for the white diffuse targets. This helps better the contrast and ability to discriminate false targets on highly reflective models. False targets are also much less of a problem when retro-reflective targets are used in place of diffused surface. Generally, the aperture on a camera lens can be stopped down more when retro-reflective targets are in use. Ideally the thickness of the targets should be small to reduce their intrusiveness to flow. Retro-reflective targets are typically 0.004 in thick, with a surface roughness of 200 μin, whereas the polished paint diffuse targets are typically 0.0005 in thick with a surface roughness of less than 10 μin. Ordinary lights (non-laser) can provide sufficient illumination for retro-reflective (when placed near the camera) and for white diffuse targets. In addition to retro-reflective and white targets, black targets have also been used, particularly when the VMD technique was used simultaneously with pressure-sensitive and temperature-sensitive paints. Model deformation data can be used not only to understand the aeroelastic properties of the model, but can also be used to generate a deformed surface grid of the model for improved CFD calculation and PSP mapping [9].

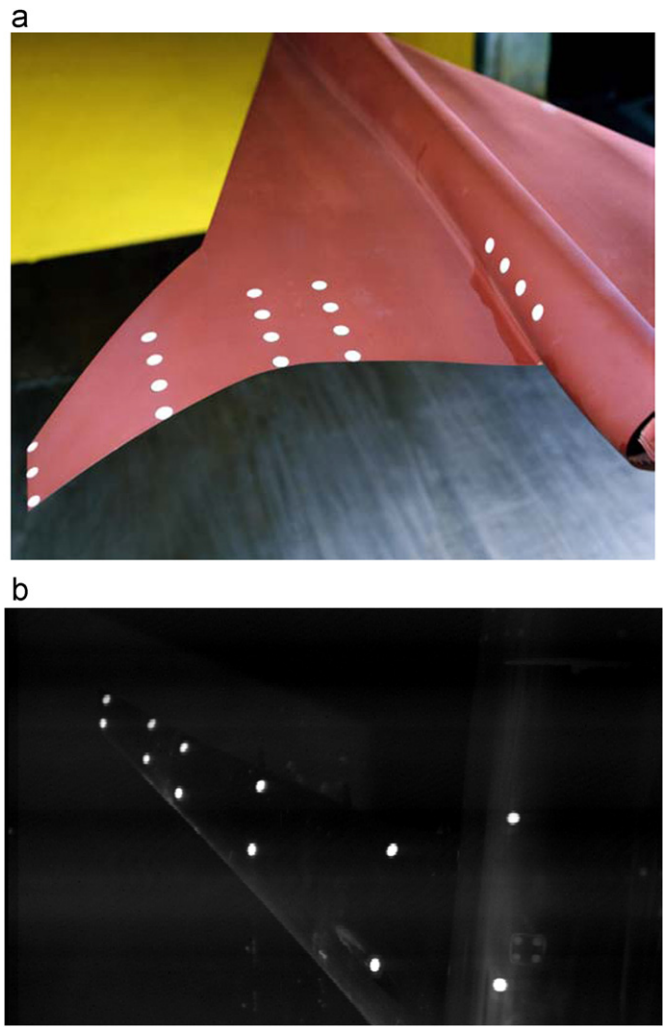

Fig. 4.4. (a) Typical target rows on a model, and (b) typical image of polished paint targets used for videogrammetric model deformation measurements.

4.2.2. Target generation for gossamer structures

Retro-reflective targets are recognized as the "gold" standard for targeting in industrial applications of precision photogrammetry [48]. They offer good contrast and target separation and provide significantly greater illumination return for applications where the viewing angle is under 60° off axis. In general, the paper-thin quality of retro targets provides a minimal impact on the object to be measured. However, it is recognized that the size and weight may impact the structural response of gossamer-type structures (see Section 10). With judicious use of targets this impact may be minimized. Although retro-reflective targets provide excellent high-contrast images, they suffer from disadvantages associated with physically attaching targets to the gossamer structure. White-light projection is an alternative that offers the advantage of non-contact measurement, thereby eliminating the problems associated with attached targets. It works well on diffuse material because, by definition, the projected light is scattered in all directions allowing the acquisition of high contrast images from any viewing angle. However, gossamer structures are often manufactured from highly transparent or specularly reflective aluminum-coated materials that provide little diffuse scattering, which in turn causes difficulties when attempting to photograph projected targets. There are two major disadvantages of white-light projection for these applications. The first is the appearance of "hot-spots" caused by direct reflections of illumination sources. Second, it requires very long exposure times, limiting its use to static measurements. Laser-induced fluorescence (LIF) target generation has recently been demonstrated as a viable alternative technique for photogrammetric target generation. This method uses LIF to generate diffuse-like scattering that allows image acquisition with fast shutter speeds and high imaging rates, and does not suffer from the disadvantages associated with either attached retro-reflective or white-light projected targets. LIF target generation has been studied and

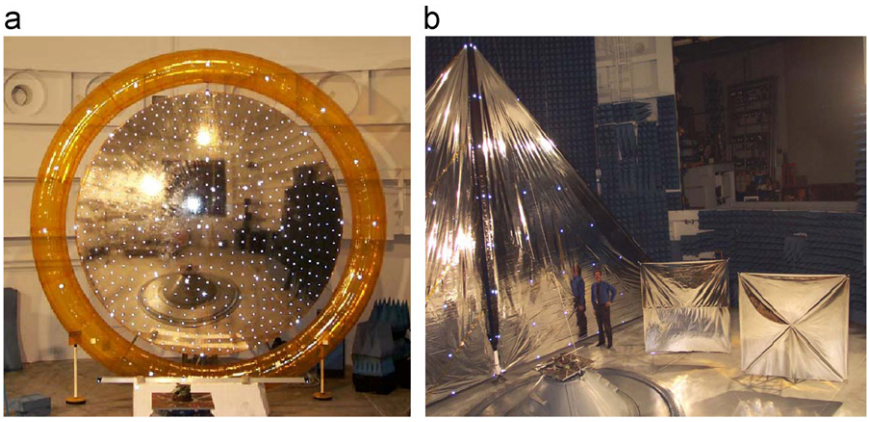

Fig. 4.5. Retro-reflective targets on two large gossamer structures, (a) 5 m inflatable parabolic reflector, and (b) scale-model solar sails.

applied to polymer membranes doped with laser-dye to aid the LIF process.

It is useful to compare the uncommon dot-projection technique with the commonly used and well-understood retro-reflective targeting technique. Several advantages and disadvantages of each method for gossamer applications have been discussed by Pappa et al. [56,85]. Fig. 4.5(a) shows a 5 m inflatable parabolic reflector with 550 6-mm-diameter retro-reflective circular targets. They were installed on this ground test article to measure the reflector shape with photogrammetry. The rms deviation of the surface from an ideal parabolic shape was measured with these targets to be about 1 mm. The targets have never been removed, and it would be difficult to do so now without destroying the reflector. For this reason, retro-reflective adhesive targets are generally not appropriate for measuring thin-film membranes whenever the targets must be removed afterwards. Fig. 4.5(b) shows two quadrants (one-half) of a 10 m square solar sail with 80 28-mm-diameter retro-reflective circular targets. It is a pathfinder solar sail model used for analytical and experimental research and development. Mode shapes of the structure at the target locations were measured with a scanning laser vibrometer. Dynamic response measurements using videogrammetry can also be made with these targets. The static shape of the structure, however, would be inadequately characterized using photogrammetry with these targets because the targets are too large and sparse relative to the wavelength of the wrinkles.

Projected dots of light are an attractive alternative to retro-reflective targets for measuring thin-film membrane structures. Fig. 4.6 shows an example of approximately 4000 circular dots projected onto a freely hanging strip of frosted plastic membrane. Projected dots offer some obvious advantages over adhesive targets for shape and dynamic measurements of membranes (e.g., thousands of targets can be used without adding mass or stiffness), but there are some disadvantages as well. For example, on shiny membranes, the majority of the projected light will specularly reflect from the surface and not enter cameras located at most viewing angles relative to the projector. This causes significant light intensity variation in the images across the area of the projected dots, complicating the photogrammetric analysis and limiting the attainable measurement accuracy. Not surprisingly, the reflection characteristics of membrane surfaces directly affect the quality of images measured with the dot-projection technique. Diffuse surfaces are generally best for photogrammetry since light scatters in all directions resulting in more-uniform contrast in the images. But, in many cases, gossamer structures will require reflective or transparent membranes. Reflective surfaces are more difficult to measure than diffuse surfaces for the reason stated above. Transparent membranes are the most

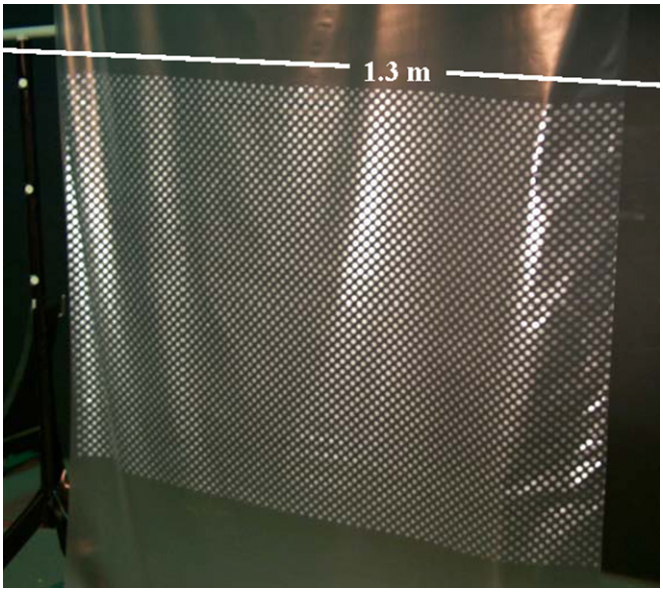

Fig. 4.6. Approximately 4000 projected dots on a thin-film opaque membrane.

difficult of all since projected light passes directly through the material. Note that all membranes have some degree of each of these optical characteristics; that is, membranes are never totally diffuse, totally reflective (specular), nor totally transparent.

Fig. 4.7 shows images obtained by simultaneous dot projection on both shiny and diffuse surfaces using side-by-side pieces of aluminized Kapton and matte-white Mylar films. Fig. 4.9(a) shows the test configuration. The three images in Fig. 4.7(b)–(d) were recorded using camera exposure times ranging from 2.5 to 20.0 s. For this test, the projector was located directly in front of the membranes and the camera was about 30° to the left. The target contrast is clearly superior on the matte surface for all exposure settings. On the aluminized surface, the target contrast varies significantly within each image and with changes in the exposure time. Variable target contrast of this magnitude complicates, but does not preclude, accurate photogrammetric analysis. With shiny membranes, the dot intensity is greatest in the images where the angle of reflection off the membrane is closest to the angle of incidence from the projector.

Different styles of projectors used to broadcast dot-projections are shown in Fig. 4.8. The images presented in Figs. 4.6 and 4.7 were obtained with the consumer-grade Kodak slide projector shown in Fig. 4.8(a). It is bright enough for dot-projection photogrammetry of relatively small objects only (e.g., under

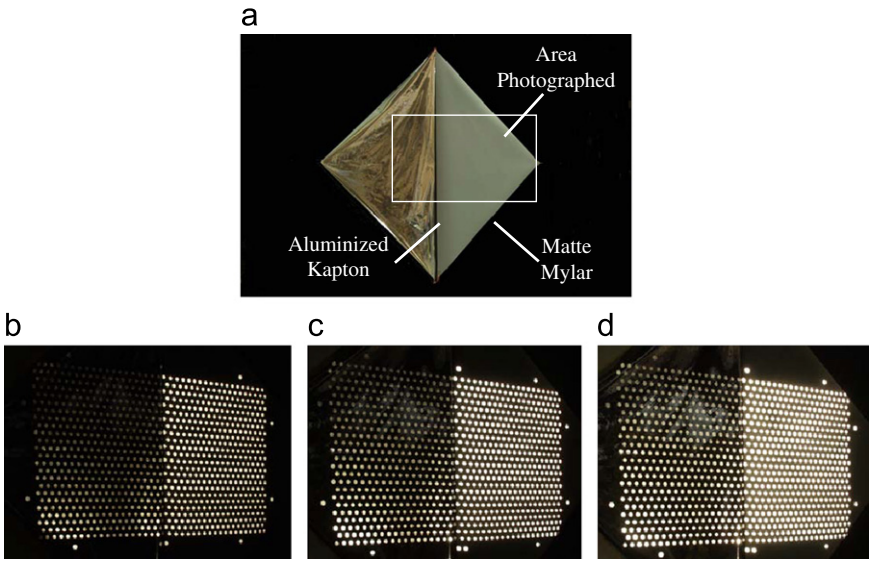

Fig. 4.7. Comparison of projected dots on adjacent shiny and matte-white membranes at various image exposure settings, (a) test configuration, (b) 2.5 s exposure, (c) 8.0 s exposure, and (d) 20.0 s exposure.

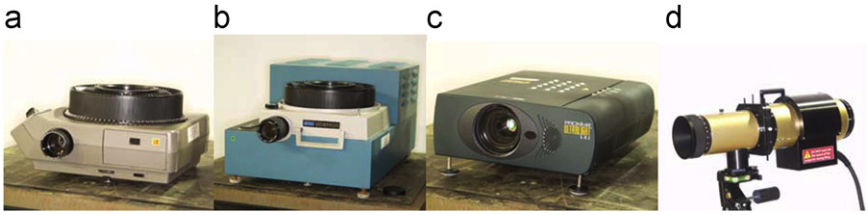

Fig. 4.8. Projectors used in this research, (a) Standard Kodak carousel, (b) high-intensity carousel, (c) digital projector, and (d) Geodetic PRO-SPOT.

2 m). A disadvantage of digital projectors is the pixelation that occurs in the projected dots, causing some reduction in target centroiding accuracy. Fig. 4.8(d) shows a professional PRO-SPOT projector manufactured by Geodetic Services, Inc. specifically for dot-projection photogrammetry [48]. It uses a high-intensity flash tube that is fired by the camera. Slides with up to 22,500 dots are available for this unit.

As previously discussed, transparent and reflective membranes are difficult or impossible to measure with standard white-light dot projection because the majority of the projected light passes directly through the membrane (in the transparent case) or is reflected in undesirable directions (in the reflective case). Consequently, images with sufficiently high contrast are difficult to obtain. The images recorded to date with dot projection on reflective membranes required long image exposure times, making dynamic measurements impossible. To overcome these problems, transparent membranes have been manufactured containing a small quantity of fluorescent laser dye. When excited with a laser light source, the dye absorbs a fraction of the laser energy and consequently fluoresces at a longer wavelength. This fluorescence is emitted in all directions providing a significantly more predictable and repeatable dot pattern that can be viewed from any angle [36,38]. Fig. 4.9(a) shows the test configuration for a proof-of-concept demonstration of this proposed new approach for dot-projection photogrammetry and videogrammetry of membranes.Fig. 4.9(b) shows the test article, which is a small sample of dye-doped CP-2 polyimide membrane wrapped around the top of a white cardboard tube. Note the almost transparent nature of the material. The membrane was illuminated with a laser-generated dot pattern using a 2 mW green (544 nm) helium-neon laser and a diffractive beam splitting element. Fig. 4.9(c) shows a typical digital photograph taken with a low-pass optical filter placed in front of the camera. The filter blocks the reflected green laser light but allows the orange fluorescence light from the membrane dye to pass through. Note that laser speckle is not a problem because photographs are taken of the self-generated (orange) dots of light and not the directly reflected (green) dots of light from the laser. Using several images taken at other viewing angles, an accurate 3D model of the membrane, shown in Fig. 4.9(d), was obtained.

Note that the bottom portion of the membrane with the white cardboard backing produces spots in Fig. 4.9(c) that are almost four times brighter than for the membrane without a backing. This is because the laser energy is scattered by the cardboard and passes though the polymer a second time, effectively doubling the laser (and hence fluorescence) intensity. The fluorescence emitted backwards is also scattered by the cardboard and becomes visible from the front. A similar increase in brightness is expected for doped transparent membranes that have a reflective back coating, such as a solar sail. The bright spot in the center of the pattern is due to the non-diffracted zero-order laser energy from the diffractive beam splitter. Experimentation continues with pulsed laser systems that will potentially allow acquisition of images at video frame rates and hence will provide the capability to make dynamic measurements of dye-doped transparent and reflective membranes that are currently impossible with white-light dot projection systems.

It may be easy to misunderstand exactly what is being measured with the dot-projection technique. This is particularly true for dynamic measurements made with videogrammetry. Clearly, the location of each projected dot on a structure matches the location of the underlying surface. The photogrammetric process accurately computes the 3D coordinates of the center (centroid) of each dot at each instant of time [83,84]. Thus,

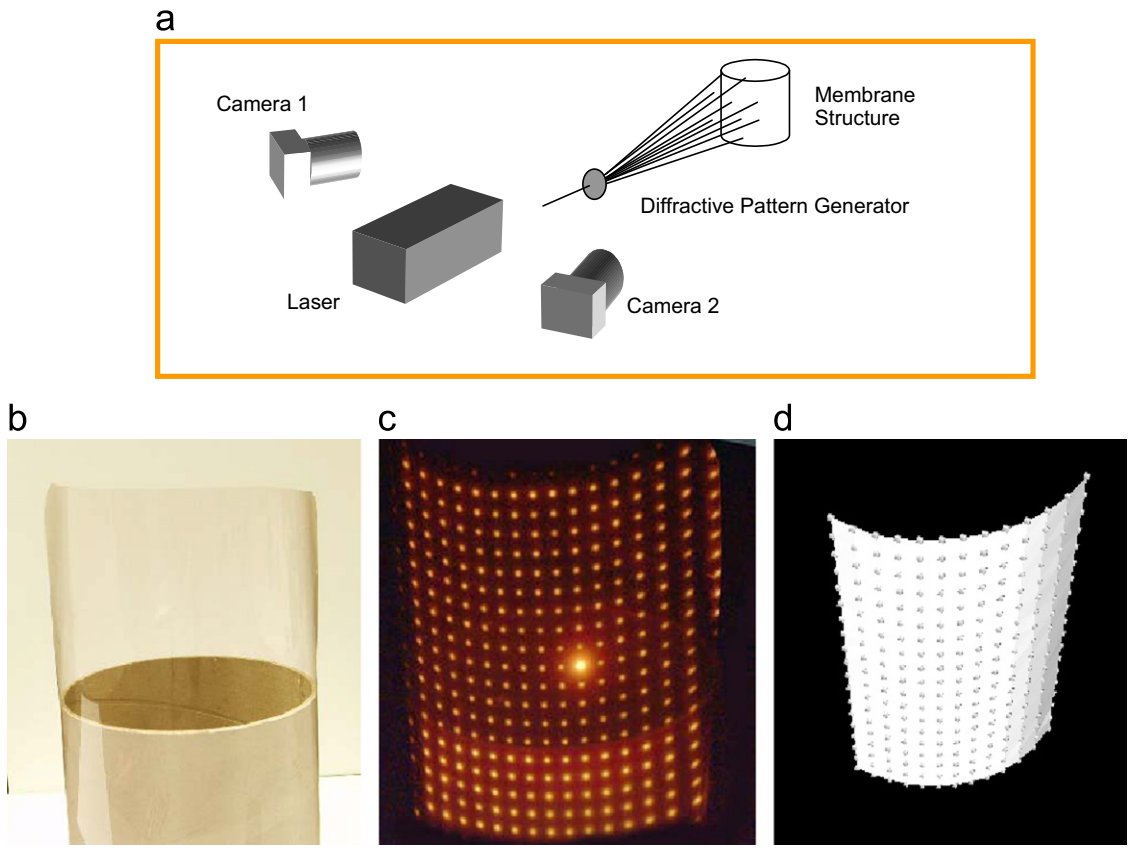

Fig. 4.9. Laser-induced fluorescence for dot-projection photogrammetry of transparent membranes, (a) test configuration for proof-of-concept experiment, (b) transparent CP-2+dye, (c) fluorescence from laser dot projection, and (d) 3D surface by photogrammetry. (For interpretation of the references to colour in this figure legend, the reader is referred to the web version of this article.)

photogrammetry generates a set of 3D points, a so-called point cloud, defining the shape of the structure at the target locations at any instant of time. For static shape measurements, this calculation is performed once. For dynamic measurements, the target coordinates are tracked versus time, generating a series of point clouds and each of these point clouds also accurately defines the shape of the structure at the corresponding instant of time.

However, projected dots do not move with the structure when it vibrates or changes shape in the same way as attached targets do, which is typically the point of confusion. This is an important fundamental difference between attached and projected targets for dynamic measurements. An attached target will move in all three coordinate directions with the structure. Videogrammetry calculates x, y, and z-direction time histories for each attached target that match the motion of the underlying structure in all three directions. A projected dot, however, can only move along a straight line either towards or away from the projector regardless of how the structure moves. Note that a projected dot on a surface represents the intersection of the surface and a stationary ray of light from the projector. Regardless of how the structure vibrates or changes shape, the intersection point for that dot will always lie somewhere on the same ray of light. With projected-dot targets, videogrammetry will again correctly measure the dynamic 3D movement of each target, but in this case the path of each target always follows a straight-line course moving either towards or away from the projector.

Besides ordinary targets, coded targets are introduced in photogrammetric systems. Their automatic detection, recognition, identification, and measurement have facilitated fully automatic exterior orientation and 3D object point determination. In many photogrammetric projects it is highly desirable to have a large number of targeted points to better approximate the true shape of the object.

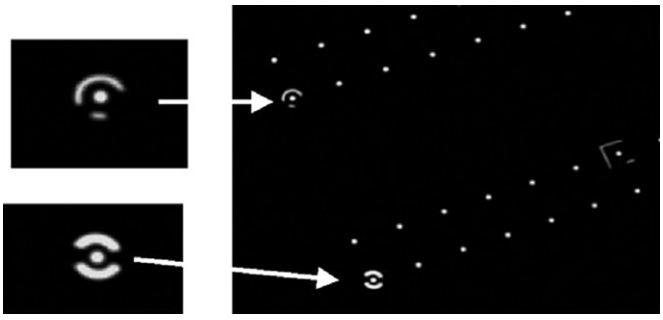

Fig. 4.10. Coded targets used to support photogrammetric measurements.

To automate the process of target identification, many software vendors have included coded target detection in their image scanning algorithms. The codes, which are generally in the form of either a ring or geometric dot pattern, form unique identifiers that are detected, labeled and measured automatically by software. When visible in multiple images, the codes serve as either control or tie points for determining camera position and orientation. Generally, a minimum of 4 to 6 codes is required in each image to support automatic identification of all other targets in the image. Fig. 4.10 provides a representative view of ring-shaped coded targets included in a measurement project.

4.3. Software

4.3.1. Model deformation measurement

Software for videogrammetric model deformation (VMD) measurements is developed specially for wind tunnel testing,

including a suite of routines for image acquisition, target-tracking, identification and blob analysis, centroid calculation, camera calibration/orientation, photogrammetric intersection, and deformation calculation. The structure of the custom software is shown in Fig. 4.11. The software is used to acquire images, locate targets and calculate their centroids, convert target centroids to spatial coordinates in the object space, and compute deformation. Camera calibration/orientation provides the interior and exterior orientation parameters of a camera necessary for the solution of the collinearity equations between the object space and the image plane.

For the VMD technique used in major NASA wind tunnels in the past, standard analog video cameras and PC-based image acquisition frame grabber boards were utilized. The standard RS-170 video signal has an interlaced analog format, with a vertical resolution of 240 pixel per field, and a horizontal resolution determined by the frame grabber. Horizontal resolutions of 640 or 752 are commonly used. However, two fields are combined to give a total vertical resolution of 480, with the added complication that adjacent rows in the final image may have been exposed at different times. This potential problem (for dynamic situations) can be avoided by using single video fields in the model-deformation measurement process, but with reduced vertical resolution. Progressive-scan cameras are non-interlaced and may be more suitable for dynamic conditions.

The target-tracking implementation of the VMD technique uses a double-buffer strategy for image acquisition and processing. At the completion of a single image acquisition, a new image is stored in a second buffer at the same time the first buffer is processed. Since the frame grabber board employs a bus-mastering PCI interface, the main processor of the host computer is free to perform the processing even while a grab is in progress. On the completion of each frame, the acquisition and processing operations are switched between the two buffers. In the free-running mode, the buffer-switching and processing operations are triggered automatically by the end of a video frame through the use of callback functions. The double-buffer method implemented in software yields a throughput of 15 frames per second using standard video-rate CCD cameras. With a high-speed progressive-scan CCD camera, a system throughput of 60 images per second is possible.

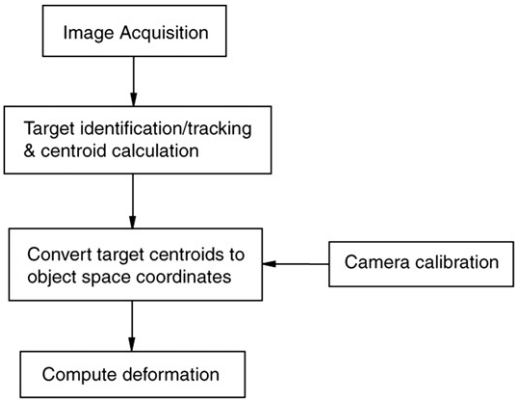

Fig. 4.11. Flowchart of VMD data acquisition and processing.

Once a video frame has been acquired, targets must be identified and located. This is done with a gray-scale centroid calculation to sub-pixel resolution after subtracting an automatically determined background level in the neighborhood of each target. The target centroid $(\bar{x},\bar{y})$ is defined as $\bar{x}=\sum\sum x_i I(x_i,y_i)/\sum\sum I(x_i,y_i)$ and $\bar{y}=\sum\sum y_i I(x_i,y_i)/\sum\sum I(x_i,y_i)$, where $I(x_i,y_i)$ is the gray level. While target tracking, only regions in the image plane in the immediate neighborhood of the targets are utilized, which reduces problems associated with stray image features away from the tracking regions.

Once target-tracking is initiated by the user, the system will continuously track the position of the selected targets, returning a live stream of target position data upon trigger. The size parameters and thresholds are maintained in real time for each target, so the system is relatively insensitive to lighting changes that may occur with changes in model attitude. Anomalies in target-tracking may result from bright surface reflections which interfere with a particular target in the image, high-speed model motion which blurs the targets, or loss of image due to severe lighting changes or obstruction in the viewing field. Target-tracking is improved for such cases by memorizing the last "good" position of targets in the target-tracking process. Once tracking is lost on a particular target, the system will recover the target based on memory of the last known position of the lost target. The memory-based target tracking technique has been implemented and significantly enhances the robustness of the target-tracking against the anomalies.

As discussed before, the analytical camera calibration/orientation techniques are used for the determination of the interior and exterior orientation parameters and lens distortion parameters of the camera/lens system. The optimization method (combined with DLT for the initial values of the exterior orientation parameters) allows automatic camera calibration for the interior and exterior orientation parameters and additional parameters for a given 3D target field that is appropriately aligned with the tunnel coordinate system (see Fig. 4.12). This feature particularly facilitates VMD measurements in large production wind tunnels due to time constraints during videogrammetric setup and calibration.

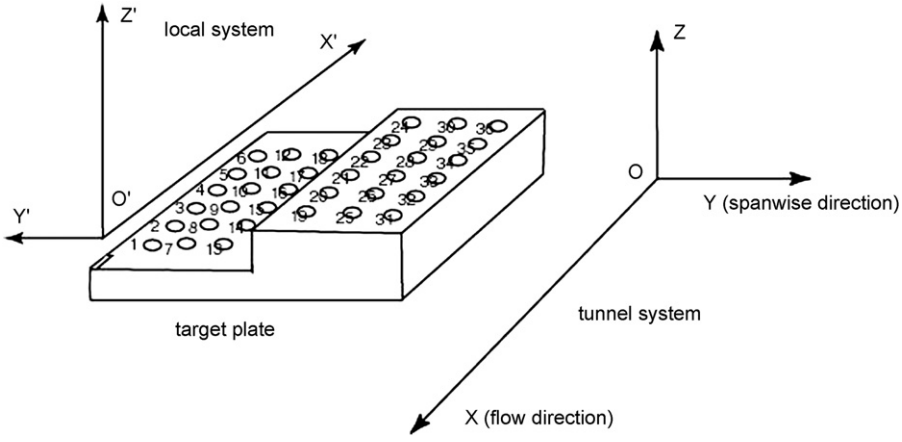

Fig. 4.12. A step calibration target plate aligned with the tunnel coordinate system.

The accurate determination of the interior orientation parameters requires a target field filled in a larger portion of images. However, in large wind tunnels, a target plate placed near a tested model viewed by cameras mounted in windows on the tunnel walls often occupies only a small portion of images. As a result, the interior orientation parameters cannot be accurately obtained. In this case, a two-step approach is suggested, in which the interior and exterior orientation parameters are determined separately. First, a target plate is placed near a camera to be calibrated such that the target field fills up the image plane and consequently the interior orientation parameters can be accurately determined using the optimization method. It is assumed that the interior orientation parameters are fixed as long as the camera/lens setting is locked. Then, the target plate is placed in the position near the tested model and aligned with the tunnel coordinate system; the exterior orientation parameters are obtained for the fixed interior orientation parameters. Fig. 4.13 shows preparation of camera orientation using a step calibration target plate aligned with the tunnel coordinate system.

The data-reduction procedures for the VMD technique include object-space coordinate calculations and deformation calculations. Once the target centroids are computed and the camera orientation parameters are determined, the image-plane coordinates (x,y) can be converted to object-space coordinates (X,Y,Z) using the collinearity equations. A solution for (X,Y,Z) is not possible using a single set of image coordinates (x,y) unless additional information is available. In a single-camera VMD system that has been used in NASA wind tunnels due to its simplicity, the spanwise locations of the targets are usually fixed to reduce the number of unknowns and to calculate the remaining two coordinates. In other words, the collinearity equations can be solved for (X,Y,Z) under a constraint $Y=$const. (normally the semispan coordinate). The geometric explanation of the single-camera solution is illustrated in Fig. 4.14. The solution (X,Y,Z) is the intersection point between the plane $Y=$const. and a line from the image point passing through the perspective center of the lens. When the angle between the plane $Y=$const. and optical axis is zero, there is no unique solution. Therefore, this angle must be large enough (typically larger than 20°) to obtain a more accurate single-camera solution. The single-camera approach works very well for pitch-only sweeps, where a streamwise row of the targets on a wing will basically remain at the same spanwise location, but would fail or require additional information for yaw sweeps. This method is also directly applicable to the angle-of-attack measurements and bending measurements on high-lift systems. Although a multi-camera system enables a more direct solution in more general cases, the single-camera approach has an advantage in simplicity. For a two-camera system, simultaneous images are acquired using two video cameras viewing the same set of targets. Thus, for each target, two sets of collinearity equations are sufficient to determine the spatial coordinates (X,Y,Z) based on two sets of image coordinates (x,y) from the two cameras. The least-squares method is used to solve the four equations for three unknown coordinates (X,Y,Z).

Fig. 4.13. Preparation of camera orientation using a step calibration target plate aligned with the tunnel coordinate system.

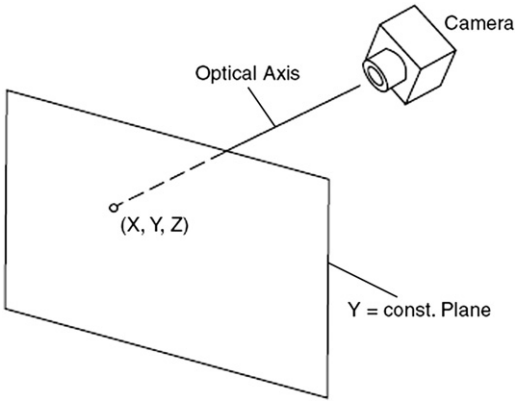

Fig. 4.14. Geometric illustration of the single-camera solution.

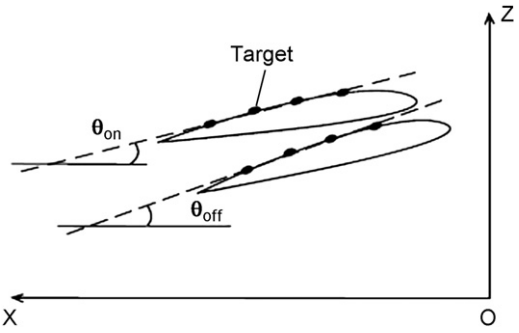

Fig. 4.15. Wing deformation at a spanwise location, where θ_{on} and θ_{off} denote the local pitch angles in wind-on and wind-off cases, respectively.

Two methods are used to calculate twist and bending of a wing. One is the linear fitting method used only for twist calculation. The local angle-of-attack (AOA), defined as $\theta=-\tan^{-1}(\Delta Z/\Delta X)$, is calculated by a linear fit to the target coordinates in the (X,Z) plane at a given spanwise location, as shown in Fig. 4.15. In the wind-tunnel coordinate system (X,Y,Z), the X-axis is in the flow direction, the Z-axis is in the upward direction on the wing surface, and the Y-axis is in the spanwise direction following the right-hand rule. The local wing twist due to aerodynamic load is defined as twist$=\theta_{twist}=\theta_{on}(\eta)-\theta_{off}(\eta)$, where $\theta_{on}(\eta)$ and $\theta_{off}(\eta)$ are the local AOAs in the wind-on and wind-off cases at the normalized semi-span location η. In practical wind tunnel tests, direct calculation is not applicable since the model may not be at the same pitch angle in the wind-on and wind-off cases. Thus, a correction method is used for twist calculation. First, the angle difference $\Delta\theta(\theta_{off})=\theta_{off}-\alpha_{ref}$ in the

wind-off case is fitted using a polynomial as a function of θ_{off}, where α_{ref} is the reference angle-of-attack and θ_{off} is the local AOA obtained by the VMD system in the wind-off case. The reference α_{ref} could be the AOA readout from a wind tunnel system or other reliable AOA data. The wind-on angular data at each semispan station is corrected based on the wind-off calibration curve fits. The corrected AOA $(\theta_{on})_{corr}$ in the wind-on case is calculated using $(\theta_{on})_{corr}=\theta_{on}-\Delta\theta(\theta_{on})$. Finally, the wing twist is obtained using the following relation twist$=\theta_{twist}=(\theta_{on})_{corr}-\alpha_{ref}$.

The 2D transformation method can be used to calculate both wing twist and bending. Assuming that the cross-section of a wing does not deform, a conformal transformation between the wind-on and wind-off coordinates (X_{on},Z_{on}) and (X_{off},Z_{off}) is

$$\begin{pmatrix} X_{on} \\ Z_{on} \end{pmatrix} = \begin{pmatrix} \cos\theta_{twist} & \sin\theta_{twist} \\ -\sin\theta_{twist} & \cos\theta_{twist} \end{pmatrix} \begin{pmatrix} X_{off} \\ Z_{off} \end{pmatrix} + \begin{pmatrix} T_x \\ T_z \end{pmatrix},$$

where T_x and T_z are the translations in the X- and Z-directions, respectively. Given the coordinates (X_{on}, Z_{on}) and (X_{off}, Z_{off}) of a number of targets, the twist θ_{twist} and translations T_x and T_z can be determined using the least-squares method. Wing bending is $bending=T_z-(T_z)_{ref}$, where $(T_z)_{ref}$ is the reference Z-translation in a reference location such as the fuselage.

4.3.2. Measurements of gossamer structures

Pappa et al. [83,84] described the eight steps in photogrammetry measurements of gossamer structures using a typical commercial software package, PhotoModeler Pro (Eos Systems, Inc) for camera calibrations and data analyses. The following steps that are typical in commercial photogrammetric software include: calibrating cameras, planning measurements, taking photographs, importing photographs into PhotoModeler, marking target locations on each image, identifying referencing points in images, processing data (bundle adjustment), and exporting 3D coordinates to CAD program. The primary function of the software is the processing of 2D image measurements of targets to produce 3D object space coordinates of those same points through multi-image photogrammetric triangulation. In many cases the process can be used to simultaneously determine the calibration of the camera(s) within the network either as a primary task or as a secondary benefit. Most commercial software packages either automatically or interactively guide the user through a process of (1) loading the images, (2) marking the targets, (3) referencing the marked targets on multiple images and (4) processing.

The processing step itself is comprised of intermediate steps. The first is known as exterior orientation, which essentially establishes the relative positions of all images forming the network within a specified 3D coordinate reference frame. This may be accomplished via either photogrammetric "relative orientation" or via "spatial resection". Resection, which mathematically computes the position and orientation of each camera position with respect to the assigned coordinate system of the object, is the most common approach since each image can be processed separately. Conceptually, the second step, known as "spatial intersection", uses the computed locations of each camera station to determine the 3D location of a target point by intersecting the imaging rays from all images containing that point. Thus, intersection can be performed point-by-point. Almost universally, however, exterior orientation is refined and spatial intersection performed simultaneously for all points in a multi-image "Bundle Adjustment", which uses the principle of collinearity and incorporates an iterative least squares estimation process to compute the final estimates of 3D target point coordinates and the spatial position and orientation of each image.

The processing of video sequences for the purpose of tracking dynamic motion is a relatively new feature now found in many packages. The user can record an object with two or more video cameras and then process the recorded video to track 3D motion of the targeted object. In most cases the software has the ability to process images in Tagged Image File Format (tif), Windows Bitmap (bmp), JPEG (jpg) or Audio Video Interleave (avi) image sequences. While static cameras allow shape measurement of gossamer structures, the video systems allow low frequency (typically less than 15 Hz) vibrations to be evaluated.

Typically, within the photogrammetry software the measurement process is automatic with default settings governing the solution. However, in those cases where the imagery may be less than optimal the more experienced user can interactively modify parameters to assist the process in reaching a desired solution. Various statistics are often produced for each image as well as for each target point in the solution as a byproduct of the process to assist the user in evaluating the measurement.

The precision of the marked targets as well as that of the derived 3D object point coordinate data is typically the most important information. In most settings outside a laboratory, RMS values for image coordinate residuals (effectively a measure of the internal consistency of the multi-ray spatial intersections) of less than 0.1 pixel are achievable if a good convergent design has been implemented. In high-precision surveys of very stable objects, this figure can be as low as 0.03 pixel. However, of ultimate interest to the user is invariably the standard error for the *XYZ* coordinate estimates for each target point.

In addition to statistical reports to aid in the evaluation of the solution, 3D graphic representations similar to the point cloud and camera station layout assist the user in evaluating the measurement. As photogrammetry has become increasing more popular in the industrial work place the requirement to export 3D model data for use in external CAD, graphics, animation and rendering packages is becoming a commonly requested feature in the processing software. Several software packages offer simulation utilities that aid in the determination of camera orientation and principal distance, two factors that greatly influence target identification when cameras are to be pre-positioned to measure an object. Simulations provide the user the ability to pre-plan measurement positions. The growing number of systems and software tools available from manufacturers has significantly improved the confidence of measurement systems specialists seeking tools with photogrammetric capabilities.

5. Deformation measurements in wind tunnels

Aeroelastic deformation measurements have been made for a number of tests in large production wind tunnels at NASA and Arnold Engineering Development Center (AEDC) over the last 15 years. These facilities (some of which have been decommissioned) are the National Transonic Facility (NTF), the Transonic Dynamics Tunnel (TDT), the Unitary Plan Wind Tunnel (UPWT), 14×22 ft Subsonic Tunnel and the 16-ft Transonic Tunnel (16 ft) at NASA Langley, the 12-ft Pressure Tunnel at NASA Ames, and the 16-ft Transonic Wind Tunnel at AEDC [9,19,20,21,23,25,43,99]. Photogrammetric measurements at the Vertical Spin Tunnel and hypersonic wind tunnels are described by Barrows [4] and Jones and Lunsford [58], respectively. The location of the data-recording camera varies with the tunnel due to window location constraints, competition with other instrumentation for viewing ports, and ease of mounting. VMD measurements on sting-mounted horizontal models have been made at the NTF, UPWT, 16-ft, and TDT. VMD measurements have been made on wall mounted semi-span models at the NTF and TDT. Measurements

have been made on floor mounted semispan and bipod supported full models at the Langley 14×22 ft Tunnel and the Ames 12-ft Tunnel. Photogrammetric measurements of model attitude and position have been made at AEDC 16-ft Transonic Tunnel by using eight PSP cameras to integrate PSP and photogrammetric measurements [93,94].

5.1. National Transonic Facility

The National Transonic Facility (NTF) is a fan-driven, closed circuit, continuous-flow pressurized wind tunnel with an $8.2 \times 8.2 \times 25$-ft long test section and a slotted-wall configuration. The wind tunnel can operate in an elevated temperature mode up to $T=140\ ^\circ$F, normally using air, and in a cryogenic mode, using liquid nitrogen as a coolant, to obtain a test temperature range down to about $-250\ ^\circ$F. The design total pressure range for the NTF is from 15 psia to 130 psia. The Mach number and total pressure are varied to give the desired dynamic pressure. The combination of pressure and cold test gas can provide a range of Mach numbers from 0.1 to 1.2 and Reynolds numbers of 4×10^6 to 145×10^6 ft^{-1}. These characteristics afford full-scale Reynolds number testing for a wide range of aircraft. A major instrumentation challenge at the NTF is the requirement to make measurements over the wide range of temperature from 140 °F down to $-250\ ^\circ$F. Aeroelastic deformation measurements have been made on a variety of different models at the NTF including High Speed Research (HSR) [19], Advanced Subsonic Technology (AST) models [53], commercial aircraft, Blended Wing Bodies (BWB), and Check Standards models [4]. Fig. 5.1 shows typical wing twist of a HSR model at different dynamic pressures for $\eta=0.922$. More recent measurements of wing deformation of the DLR-F6 transport configuration were conducted in NTF [28].

5.2. Transonic Dynamics Tunnel

The Langley transonic dynamics tunnel (TDT) is best known for aeroelastic research and flutter-clearance and other aeroelastic-verification tests of fixed-wing and rotary-wing flight vehicles and launch vehicles. The TDT is a continuous-flow, variable-pressure wind tunnel with a 16-ft by 16-ft test section. The tunnel uses either air or a heavy gas as the test medium and can operate at Mach numbers up to 1.2 while obtaining Reynolds numbers of approximately 3×10^6 ft^{-1} in air and 10×10^6 ft^{-1} in R-134a gas.

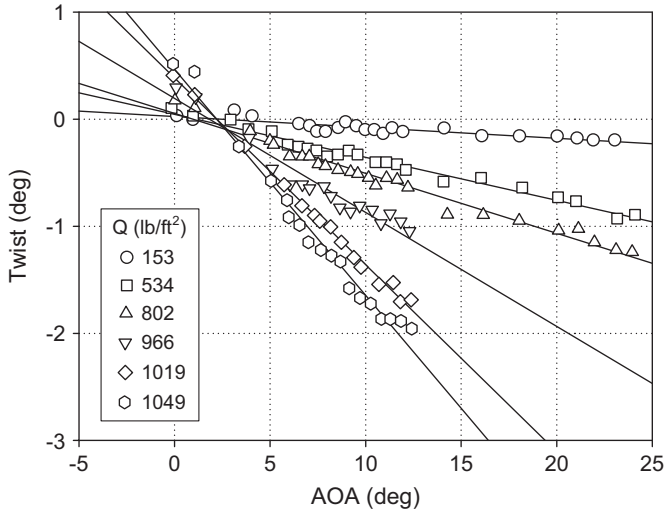

Fig. 5.1. Typical wing twist of a HSR model at varying dynamic pressures for $\eta=0.922$. Measurements were carried out in NTF at NASA Langley.

The first automated videogrammetric measurements of wing twist and bending at NASA Langley were made at the TDT in 1994 where the application of high contrast targets on the wing made possible the use of image processing techniques to automatically determine the image coordinates of the targets. Image sequences up to 8 s long at a 60 Hz rate per data point have been taken for dynamic studies. Videogrammetry has been used at the TDT for a number of tests of semispan models, both rigid and flexible, and full models [50,103,4]. Measurements have been made on the DARPA/Wright Labs/Northrop Grumman Smart Wing that had variable twist and adaptive control surfaces to provide continuous wing contour and variable camber [42]. Tests were first conducted on a conventional wing model without smart structures for comparison to the Smart Wing and to validate the model deformation system. The system was used to determine the trailing edge deflection angles of the Smart Wing that were embedded with shape memory alloy (SMA). This example is described in Section 7.1. The system was also used to measure model wing twist when the SMA torque tubes were activated. Measurements were obtained that provided near real time model control surface deflections and twist. The relevance of the model deformation at TDT, up to this point, was very well received by the tunnel researchers which led to the development of an enhanced wind tunnel specific VMD system [51]. Applications of this VMD at TDT, as well as NTF, were included in nearly every wind tunnel Test for over a decade. Some high visible testing at TDT, which included VMD, involved NASA, DARPA, Air Force, and industry funded Programs. Of these were the High Lift-to-Drag (HiLDA) Flight Program, Aerodynamic Efficiency Improvements (AEI) Program, F/A-18 Active Aeroelastic Wing (AAW) research aircraft Program, and a Morphing Wing Program. All of these programs were unique, by their own rights, and required special attention to details when setting up for the VMD.

5.3. Unitary Plan Wind Tunnel

The Langley unitary plan wind tunnel (UPWT) is a closed circuit, continuous-flow, variable-density tunnel with two 4-ft by 4-ft by 7-ft test sections. One test section has a design Mach number range from 1.5 to 2.9, and the other has a Mach number range from 2.3 to 4.6. The tunnel has sliding-block-type nozzles that allow continuous variation in Mach number while the facility is in operation. The maximum Reynolds number per foot varies from 6×10^6 to 11×10^6, depending on Mach number. A VMD measurement system has been used at UPWT for aeroelastic studies to assess Mach number and Reynolds number effects in addition to comparisons of models with flapped and solid wings. For example, data for the aerodynamically induced wing twist and bending of an HSR NCV model near the wing tip ($\eta=0.992$) for Reynolds number sweeps at Mach=2.4 are plotted in Fig. 5.2. Reynolds number variations were obtained by changing the dynamic pressure, thus the plot in Fig. 5.2 reflects the dynamic pressure effect on the change in aeroelastic wing twist. The maximum wing twist of -1.25° at Mach 2.4 occurs at a Reynolds number of 4.9×10^6. The nearly linear change in twist and displacement as a function of alpha has been observed for a number of HSR models.

5.4. Rotor blades in Ames 40-by-80-ft Wind Tunnel

Blade deformation measurements were conducted by Barrows et al. [6] on the full-scale UH-60A helicopter airloads rotor in the 40-by-80-ft wind tunnel of the National Full-Scale Aerodynamics Complex at NASA Ames Research Center. Multi-camera photogrammetry was used to measure the blade deformation of the four-bladed rotor in a range of advance ratios and thrusts, and

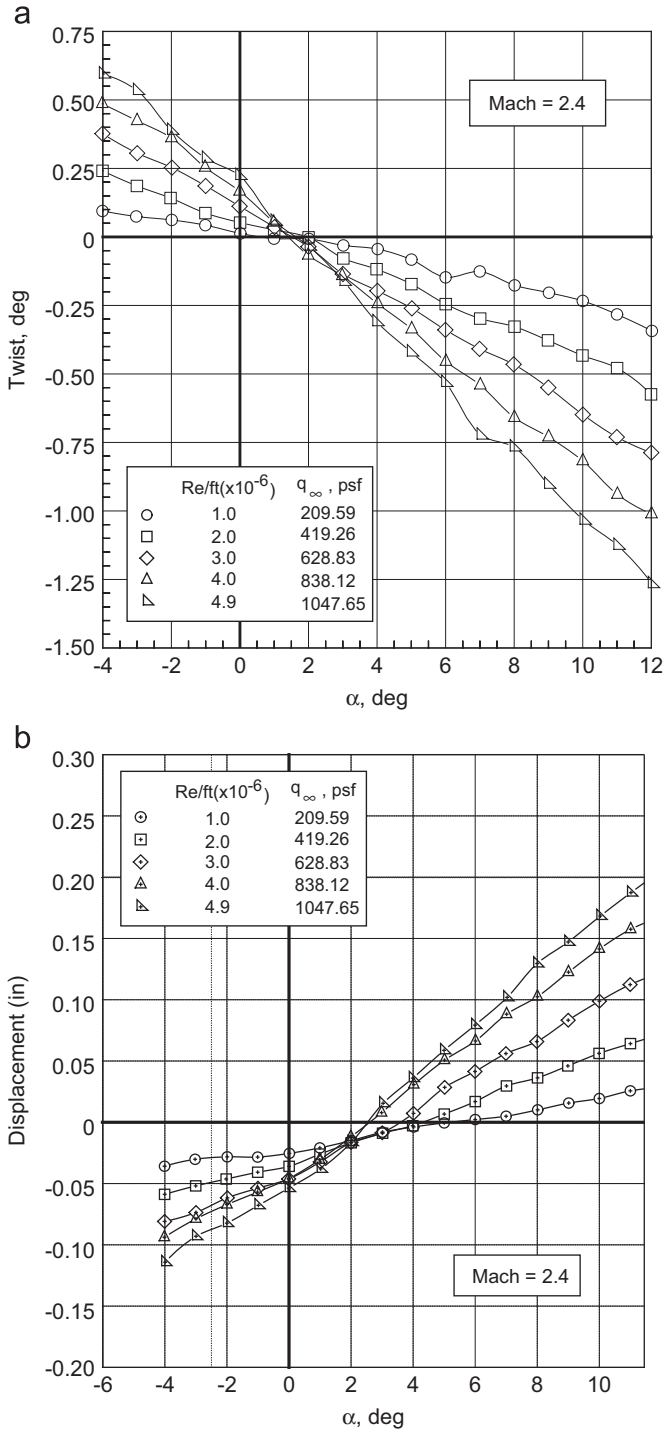

Fig. 5.2. Typical wing twist and vertical displacement of a HSR NCV model at different dynamic pressures for $\eta=0.922$. Measurements were carried out in UPWT at NASA Langley.

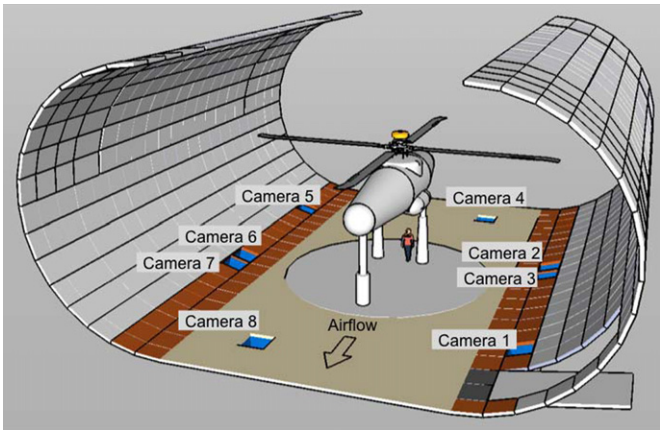

Fig. 5.3. Schematic showing the floor cavity locations in which digital cameras and strobes are installed.

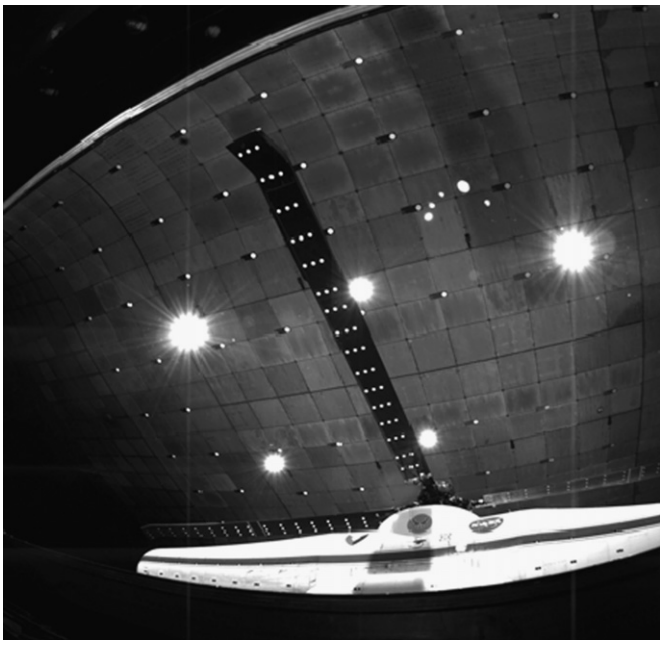

Fig. 5.4. Rotor blades with 2-in diameter retro-reflective targets and 6-in diameter targets installed onto the test-section ceiling for camera orientation.

rotor shaft angles. Fig. 5.3 is a schematic showing the floor cavity locations in which digital cameras and strobes are installed. The eight cameras positioned around the model were placed below the blades and looking up to optimize viewing of the retro-reflective blade targets. As shown in Fig. 5.4, the lower surface of each rotor blade was targeted with 48, 2-in diameter retro-reflective targets, three per radial station, uniformly spaced at approximately 0.05 blade radius intervals between the blade cuff and blade tip. In addition, 84 6-in diameter targets were installed onto the test-section ceiling in order to determine the exterior orientation parameters of the cameras. Target illumination was provided by xenon flash-lamp 50 mJ strobes with pulse duration of 10 μs. Fiber optic bundles positioned as near as possible to the optical axes of each camera lens routed the light from each strobe to illuminate the targets and maximize the light return from the blade and ceiling retro-reflective targets.

After all eight cameras are firmly anchored into their final positions in the test section, camera calibration/orientation are used to determine the exterior orientation parameters of each camera relative to the test section as well as distortion coefficients throughout testing. The constellation of 84 6-in diameter retro-reflective targets distributed over the test-section ceiling was used for calibration/orientation. The locations of the ceiling targets relative to the test section are determined using a commercial photogrammetry measurement system, V-STARS, developed by Geodetic Systems Inc. The ceiling mappings that were obtained without flow provided target locations with a standard deviation of 0.04 in. This is a good example to demonstrate how to calibrate and orient cameras in a large measurement domain based on a large calibration target field (ceiling targets) measured using a mature commercial

photogrammetry measurement system like V-STARS. Then, the sequences of images are processed to calculate accurate centroid locations of discrete targets on the rotor blades, rotor instrumentation hat, and test section ceiling. A suite of custom designed image processing and data reduction functions were developed for this effort using the Matlab software environment. Supporting functions for image processing, photogrammetry, and coordinate transformations are provided via a custom Matlab Photogrammetry Toolbox developed by Western Michigan University (WMU) for NASA [72].. The WMU Toolbox, in conjunction with Mathworks® Matlab Image Processing and Statistics Toolboxes, are integrated into a NASA rotor-specific toolbox suite of functions. The NASA Rotor Toolbox makes use of moderately automated post-test image processing procedures that identify BD targets and calculates the image plane centroid spatial coordinates for each. Fig. 5.5 shows typical pitch angles over the full azimuth. Fig. 5.6 shows aeroelastic blade bending of the blade 1 at the azimuth angle of 150°.

5.5. Other measurements

Micro-air-vehicles (MAV) usually have wings with a flexible surface and a frame. To characterize the deformation of the flexible wings and its effect on aerodynamics, photogrammetric techniques have been used to measure the coordinates of targets distributed on the wing surface as a function of time in wind tunnel testing [87,75,13,54]. In these experiments, three cameras were used for imaging and the commercial software PhotoModeler 6 was used for data processing. Further, to study flapping flight such as bird-like MAV, photogrammetric techniques are particularly desirable to measure the wing kinematics [35]. The complex wing kinematics of a flapping wing of a bat in a wind tunnel was measured by Tian et al. [104] using two high-speed cameras. Recently, Carruthers et al. [30] used six cameras positioned around a measurement volume through which an eagle flew as it approached an elevated perch to capture images of the eagle. The eagle's wing surface in flight was reconstructed via photogrammetry. Shapes and dynamics of flexible structures such as parachute canopy and the Orion Crew Exploration Vehicle airbag landing attenuation systems have been measured using photogrammetry by Jones et al. [59] and Barrows et al. [5], respectively. Photogrammetric recession measurements of ablative materials are reported by Schairer and Heincek [100] and Callaway et al. [29].

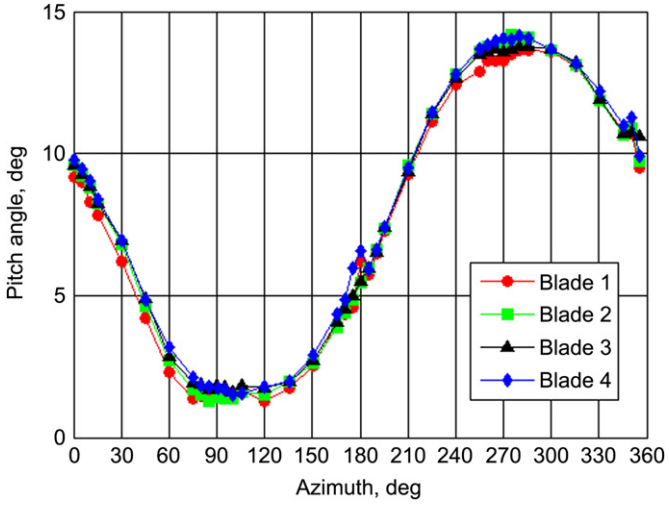

Fig. 5.5. Typical pitch angles over the full azimuth.

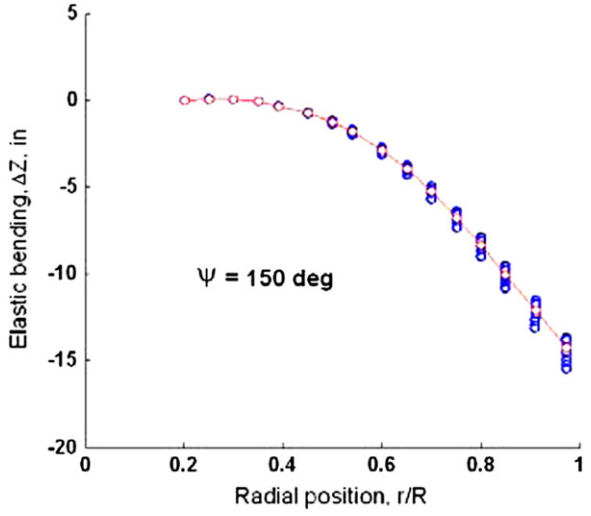

Fig. 5.6. Aeroelastic blade bending for Blade 1 at the azimuth angle of 150°.

6. Measurement uncertainty

Burner et al. [26] gives an uncertainty analysis of photogrammetric (videogrammetric) techniques used for the measurement of static aeroelastic wind tunnel model deformation and wind tunnel model AoA. Sensitivity analyses and geometrical considerations of uncertainty are augmented by analyses of experimental data in which videogrammetric angle measurements were taken simultaneously with precision servo accelerometers corrected for dynamics. Experimental comparisons with a high-accuracy indexing table were presented. It was shown experimentally that, provided the proper constraints necessary for a solution are met, a single-camera solution can be comparable to a two-camera intersection result.

6.1. Sensitivity analysis

In order to obtain (X, Y, Z) from the image coordinates (x, y), one can use the single-camera approach in which the collinearity equations are solved for (X, Y, Z) under a constraint of fixed spanwise location (Y=const.). The single-camera approach is simple, but particularly useful for wind tunnel testing where optical access is very restricted. The two-camera or multi-camera approach simultaneously acquires images and the spatial coordinates (X, Y, Z) are determined from two sets of the image coordinates (x, y). The total uncertainty of metric measurements of (X, Y, Z) is described by the error propagation equation. For simplicity of expression, when (X, Y, Z) is replaced by the index notation (X_1, X_2, X_3), the error propagation equation for the total uncertainty in the coordinate X_k is given by

$$\frac{\mathrm{var}(X_k)}{X_k^2} = \sum_{i,j=1}^{M} S_{ki} S_{kj} \rho_{ij} \frac{[\mathrm{var}(\zeta_i)\mathrm{var}(\zeta_j)]^{1/2}}{\zeta_i \zeta_j}, \tag{6.1}$$

where $\rho_{ij} = \mathrm{cov}(\zeta_i\zeta_j)/[\mathrm{var}(\zeta_i)\mathrm{var}(\zeta_j)]^{1/2}$ is the correlation coefficient between the variables ζ_i and ζ_j, $\mathrm{var}(\zeta_i) = \langle \Delta\zeta_i^2 \rangle$ and $\mathrm{cov}(\zeta_i\zeta_j) = \langle \Delta\zeta_i \Delta\zeta_j \rangle$ are the variance and covariance, respectively, and the notation $\langle\ \rangle$ denotes the statistical assemble average. Here the variables $\{\zeta_i, i=1\ldots M\}$ denote a set of the parameters $(\omega, \phi, \kappa, X_c, Y_c, Z_c)$, (c, x_p, y_p), (K_1, K_2, P_1, P_2), and (x,y). The sensitivity coefficients S_{ki} are defined $S_{ki} = (\zeta_i/X_k)(\partial X_k/\partial \zeta_i)$. Typically the sensitivity analysis of (X_1, X_2, X_3) to these parameters is made for both the single-camera solution and two-camera solution under the assumption that the cross-correlations are zero.

In wind tunnel testing, the local AoA is usually measured to determine the attitude of a model and wing twist. In a right-hand tunnel coordinate system where X is in the freestream direction, Y is in the spanwise direction and Z is in the upward direction, using two targets placed along the freestream direction on the model, the local AoA is given by

$$\theta = \tan^{-1}\left(\frac{Z_{(2)}-Z_{(1)}}{X_{(2)}-X_{(1)}}\right) = \tan^{-1}\left(\frac{\Delta Z}{\Delta X}\right). \tag{6.2}$$

For more targets, a least-squares method is used to calculate the local AoA. The variance of the local AoA (θ) is given by

$$\frac{\mathrm{var}\theta)}{\theta^2} = S_{\theta 1}^2\frac{\mathrm{var}(Z_{(1)})}{Z_{(1)}^2} + S_{\theta 2}^2\frac{\mathrm{var}(Z_{(2)})}{Z_{(2)}^2} + S_{\theta 3}^2\frac{\mathrm{var}(X_{(1)})}{X_{(1)}^2} + S_{\theta 4}^2\frac{\mathrm{var}(X_{(2)})}{X_{(2)}^2} \tag{6.3}$$

where the sensitivity coefficients are

$$S_{\theta 1} = \frac{Z_1}{\theta}\frac{1}{1+(\Delta Z/\Delta X)^2}\frac{1}{X_2-X_1},\ S_{\theta 2} = -\frac{Z_2}{\theta}\frac{1}{1+(\Delta Z/\Delta X)^2}\frac{1}{X_2-X_1}$$
$$S_{\theta 3} = \frac{X_1}{\theta}\frac{1}{1+(\Delta Z/\Delta X)^2}\frac{Z_2-Z_1}{(X_2-X_1)^2},\ S_{\theta 4} = -\frac{X_2}{\theta}\frac{1}{1+(\Delta Z/\Delta X)^2}\frac{Z_2-Z_1}{(X_2-X_1)^2} \tag{6.4}$$

In order to illustrate the sensitivity analysis, we consider a single-camera system in NTF, where the exterior parameters are $(\omega, \phi, \kappa, X_c, Y_c, Z_c) = (61.6^\circ, 0.2^\circ, -90.8^\circ, 0.1\text{ in}, -55.2\text{ in}, 34.5\text{ in})$, the interior parameters are $(c, x_p, y_p) = (26.3, -0.23, 0.33)$ in mm, the lens distortion parameters are $(K_1, K_2, P_1, P_2) = (5.96\times10^{-4}, 4.17\times10^{-5}, -3.72\times10^{-4}, 4.98\times10^{-4})$, and the pixel spacing ratio is $S_h/S_v = 0.422$. For measurement of the local AoA, two targets are placed along the same spanwise location on a wing at $(X, Y, Z) = (1, 20, 5)$ in and $(X, Y, Z) = (2, 20, 4.5)$ in. For given errors $(dx, dy) = (0.05, 0.05)$ pixel in the measurement of the target centroids, the total uncertainty $d\theta$ in the local AoA is estimated in several situations.

Fig. 6.1 shows a schematic of the wind tunnel coordinate system and the typical position of a camera. As shown in Fig. 6.2(a), when the camera moves up along the Z-direction while the camera principal distance c remains invariant, the angular uncertainty $d\theta$ increases with Z_c since not only the distance of the camera from the targets increases, but also the angle ω decreases. When the camera moves from the position 1 to position 2, the camera principal distance c can be adjusted to keep the image scale constant, maintaining a fixed distance between the two targets used for the simulation. Thus, the camera principal distance c_2 at the position 2 is given by $c_2 = c_1R_2/R_1$, where c_1 is camera principal distance at the position 1, and R_1 and R_2 are the distances between the targets and the camera at the positions 1 and 2, respectively. As shown in Fig. 6.2(a), the angular uncertainty $d\theta$ is reduced by compensating the camera principal distance at different positions.

Another case of interest is when the camera moves along the flow direction (X-direction). Fig. 6.2(b) shows the angular uncertainty $d\theta$ as a function of X_c with and without compensation of the camera principal distance c. Note the uncertainty in angle is only weakly dependent on the location of the camera in the X-direction, changing by less than 0.02° over a range of 20 in. Fig. 6.2(c) shows the angular uncertainty $d\theta$ as a function of ω as the camera moves around the model. Fig. 6.2(d)–(g) show the angular uncertainty $d\theta$ as a function of ϕ, κ, x_p and K_1. In the single-camera solution, it is assumed that the spanwise location Y of the targets is a given constant. However, in actual measurements, the given spanwise location Y of the targets may not be accurate. When there is an error in the given location Y, errors occur in the calculated X and Z. The angular uncertainty $d\theta$ is plotted in Fig. 6.3 as a function of error dY for different values of ω. Note that the angular error caused by dY can be partly thought of as a bias error that is largely reduced by zeroing. In addition a systematic error that is produced by dY and that varies as a function of the angle can be lessened considerably by the use of reference polars to calibrate the videogrammetric system in terms of known angles at each semispan station target row.

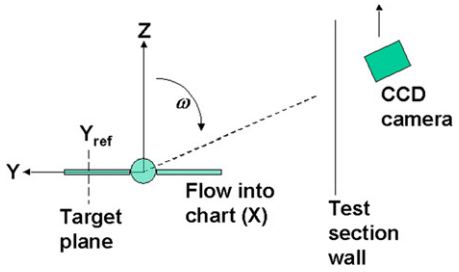

Fig. 6.1. Sketch of coordinate system and motion of camera for first case.

6.2. Target centroiding uncertainty

The uncertainty of the videogrammtric technique is related to the uncertainties in target centroid measurements, camera calibration, and data-reduction (calculations of the coordinates, twist and bending). The uncertainty in target centroid measurement is associated with camera noise, centroid calculation schemes, target size, and spatial quantization of a CCD sensor. The random errors associated with the camera noise can be collectively represented by the centroid variations for spatially fixed targets. Statistics of the target centroid variations have been measured using a standard video-rate CCD camera with a 75 mm lens viewing an array of 1/4-in. diameter circular targets. Fig. 6.4 shows typical histograms of the centroid variations in the horizontal (x) and vertical (y) coordinates on the image plane, where the standard deviations of the centroid variations in the x- and y-directions in images are 0.0081 and 0.0043 pixel, respectively, for the CCD camera with a format of 640×480 pixel. The centroid uncertainties limit the accuracy of videogrammtric measurements in the object space. When the image plane is approximately parallel to the (X, Y) plane in the object space, estimates of the limiting uncertainties in the spatial coordinates associated with the centroid random variations are $(\delta X/L_X)_{\min} = 0.0081/640 = 1.3\times10^{-5}$ and $(\delta Y/L_Y)_{\min} = 0.0043/480 = 0.9\times10^{-5}$. For example, when the characteristic lengths in the object space are $L_X = 7$ in and $L_Y = 9$ in, the corresponding measured length differences are $(\delta X)_{\min} = 182\ \mu$in and $(\delta Y)_{\min} = 162\ \mu$in.

A bias error occurs in the centroid calculation due to perspective imaging and lens distortion since the center of the target image does not coincide with the geometrical center of the target [62]. This deviation may be as large as 0.3% of the target diameter and is dependent on the viewing angle of the camera, target size, sensor size, and focal length. Another error in centroid calculation is sensor quantization, which is inversely proportional to the square root of the number of pixels in the target image. Note that this potential error source indicates larger targets are desirable, whereas the error discussed by Lenz and Fritsch [62] would indicate a need for small targets. Experimentally it has been found that a target pixel diameter of no smaller than around 5 pixel is a good compromise. It is typically better to use targets that are somewhat larger than the recommended 5 pixel diameter for initial lens setup rather than smaller. The larger target sizes may help to compensate for possible unknown image scale during further lens changes that may be necessary to accommodate the test object motion, for instance, pitch angle changes during testing.

6.3. Reference polar analysis

Reference polars of wind tunnel models can be used to periodically to calibrate the videogrammetric measurement

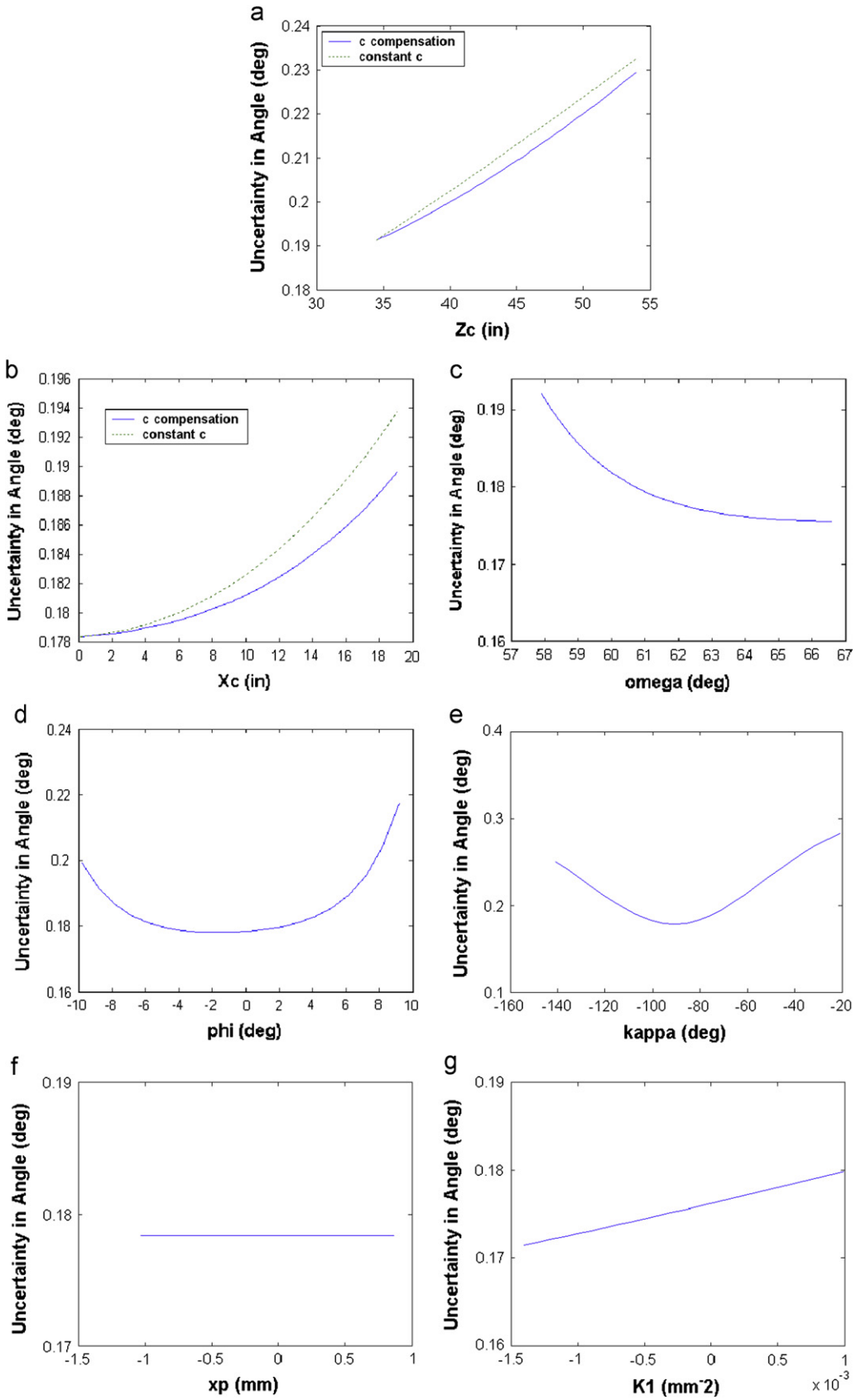

Fig. 6.2. Sensitivities of the uncertainty in angle to the parameters (a) Z_c, (b) X_c, (c) ω, (d) ϕ, (e) κ, (f) x_p, and (g) K_1.

system in terms of the onboard accelerometer used for precision pitch angle measurements. An example of the angular change in zero-shift over 2.5 months at the National Transonic Facility is plotted in Fig. 6.5 as a function of run set number. These 25 data sets contain over 3500 data points. The data is plotted for each of the 6 semispan stations where deformation data were acquired.

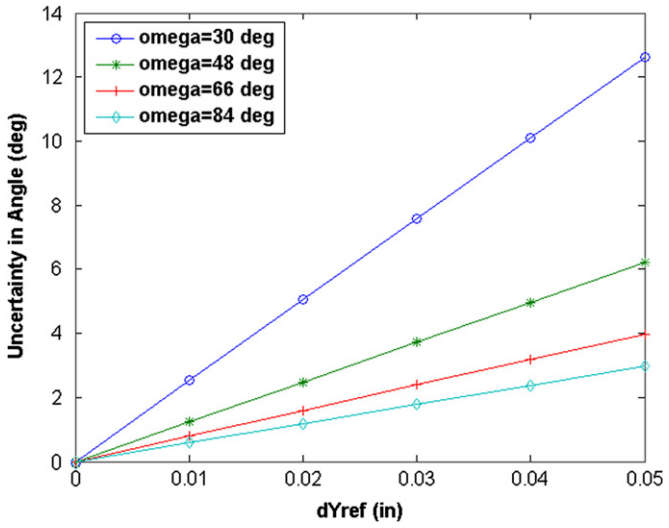

Fig. 6.3. Uncertainty in angle as a function of error in Y_{ref}.

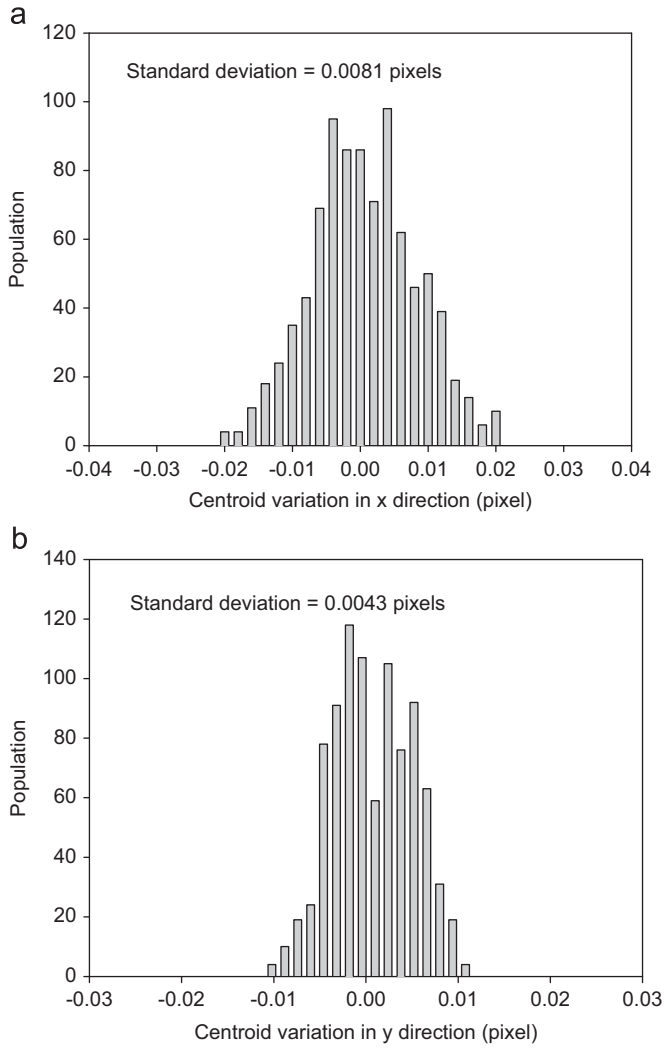

Fig. 6.4. Histograms of centroid variation: (a) horizontal direction x, (b) vertical direction y.

The inboard station at $\eta=-0.05$ was used to remove angular sting bending and any bias error common to all the semispan stations. The relatively large change in zero-shift evident at

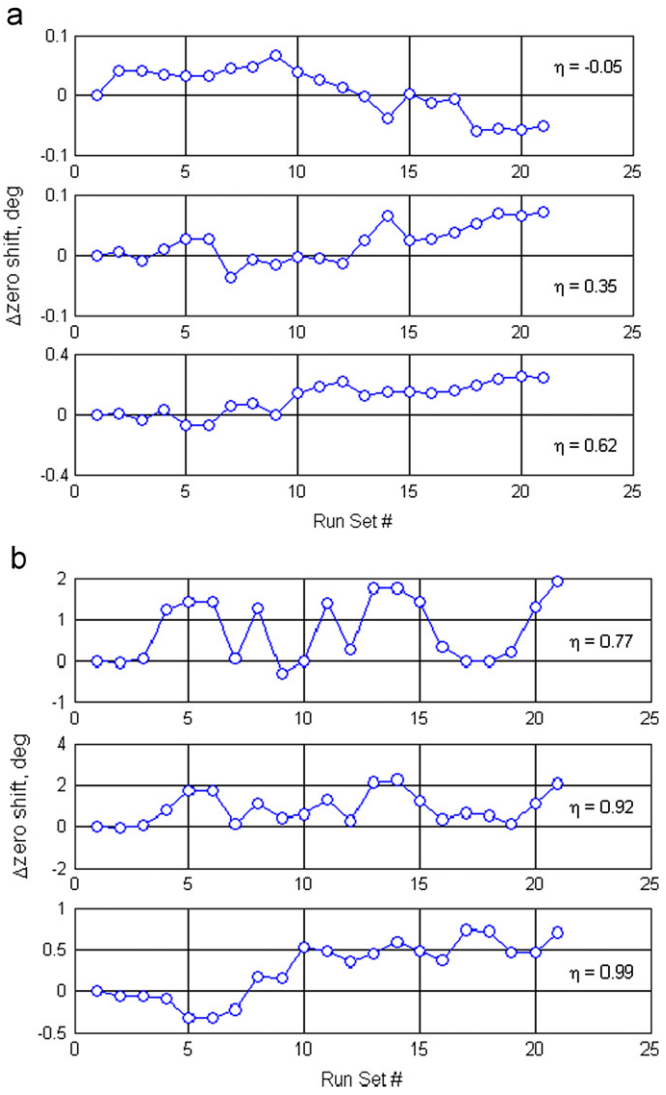

Fig. 6.5. Change in zero-shift as a function of run set number over 2.5 months for (a) inboard semispan stations, and (b) outboard semispan stations.

$\eta=0.77$ and 0.92 occurred due to a part change with corresponding new targets at different local angles. Two targets were present at each semispan station η. Target spacing varies from 6 in at $\eta=-0.05$ to less than 2 in at $\eta=0.99$. Although the change in zero-shift inboard is less than 0.1° throughout the 2.5 month test, changes in zero-shift near the tip approached 1°. The angular changes in zero-shift at the various η stations at different total temperature and total pressure indicate that there is no dramatic correlation with temperature or pressure. Thermal expansion and contraction of the test section that may lead to a non-repeatable orientation in pitch of the video CCD camera may not necessarily be the cause of the zero-shift since that type of orientation change should be observed at all semispan stations (especially for $\eta=-0.05$ and $\eta=0.35$) which is not reflected in the data plots. The values of zero-shift and slope change of the videogrammetric calibration data should be compared to precision servo-accelerometers, which typically have a zero-shift of less than 0.01° and a slope change (at $\alpha=6°$) of 0.001° or less over several months. Fig. 6.5 illustrates the value of periodic zero shift compensation. At the NTF it is common practice to bracket wind-off calibration polars around each wind-on data set at a particular test temperature in order to compensate for zero and slope changes over time.

6.4. Single-camera vs. two-camera

Static angle measurements were conducted in a laboratory to compare the single camera solution and two-camera solution. A two-camera measurement system [66] was used for these tests. Individual camera centroids from the two-camera measurement system were used to compute two sets of single-camera angular results to compare to a single set of two-camera results. A high-accuracy indexing table, which has been calibrated to achieve an accuracy better than 0.0003°, was used as the standard for comparison. The pitch angle was varied over a range of −10° to 30° in 1° increments. A second indexing table was used to introduce roll angles of 0°, ±2°, and ±4° to assess the effect of an unknown roll on the angle data. No correction was made for the roll to simulate the case for wind tunnel models where an unknown roll may be present. Small roll angles are seen to introduce a zero-shift in the measured values. The two-camera measurement results are presented in Fig. 6.6. For this figure and the following two plots, the known set angle is subtracted, leaving the angular error compared to the known standard. Figs. 6.7 and 6.8 show the single-camera measurement results for the image data from the same two cameras as used to acquire the two-camera intersection results. Note the similarity of the two-camera solution and one-camera solution from Camera 1. The one-camera solution from Camera 2 is somewhat better than the results either using Camera 1 or using both cameras. These results suggest that if the constraints of the single camera solution are met, angular measurements with a single camera can be comparable to two-camera intersection.

It is emphasized that the assumption in the single-camera solution is that the Y coordinates of the targets are invariant in wing bending. However, wing bending causes the Y coordinate of wing targets to decrease (moving toward the body) which causes a bias error in the computation of X and Z in the single-camera solution if it is not properly accounted for. Consider the case for simple beam bending given by $\Delta Z = c_1 Y^2 + c_2 Y^3$, where c_1 and c_2 are constants. An arc length computation can be used to estimate the amount of shift as a function of Y. For the case of a single beam bending, an estimate is $\Delta Y \approx (2/3)\, c_1{}^2 (Y - Y_o)^3$, where Y_o is the semispan location at which deflection starts. For example, if $(Y - Y_o) = 30$ in at $\eta = 1$ with a tip deflection of 1 in, then $\Delta Y \approx 0.022$ in. In other words, the correct Y to use for the deflected tip target should be less by this ΔY. A partial correction for this effect can be implemented by first calculating the X and Z coordinates without correction for ΔY, then determine a first estimate of c_1 to get an estimate of the correction ΔY before re-computing X and Z with the single-camera solution. One or two iterations should be sufficient for typical applications.

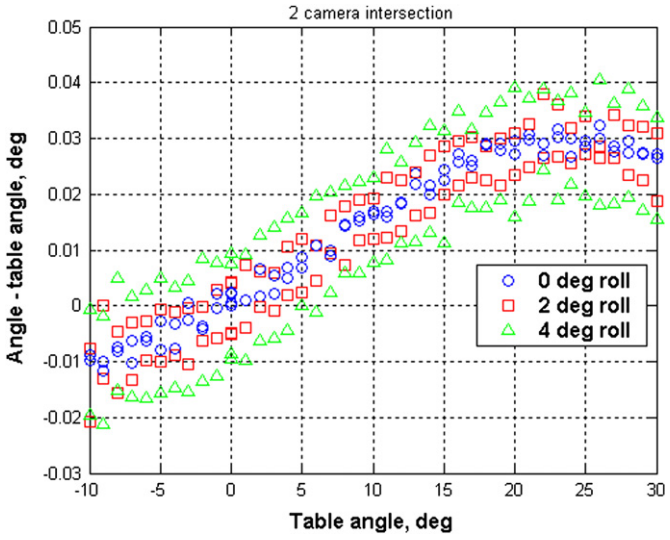

Fig. 6.6. Two-camera intersection with roll angles of 0°, ±2°, ±4°.

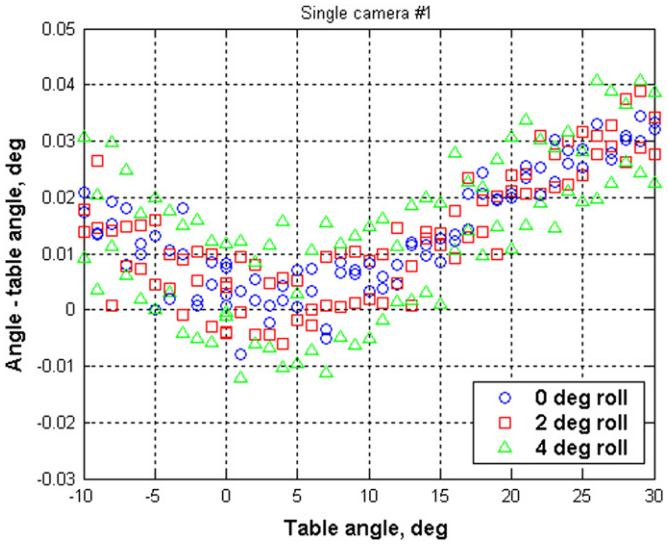

Fig. 6.7. One-camera solution of Camera 1 with roll angles of 0°, ±2°, ±4°.

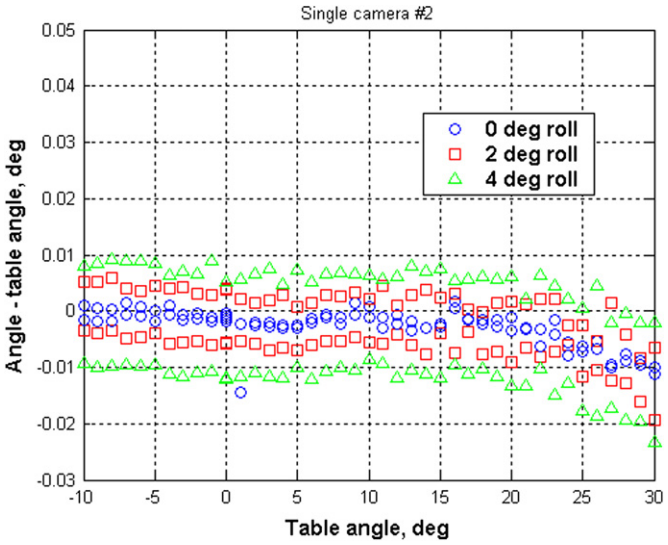

Fig. 6.8. One-camera solution of Camera 2 with roll angles of 0°, ±2°, ±4°.

7. Special measurements in ground facilities and flight

7.1. Smart Wing deformation at Langley TDT

The single-camera videogrammetric model deformation (VMD) technique was used during all four Smart Wing entries in the NASA LaRC TDT to obtain deformation measurements [44]. For the first three tests, the measurements were made at three spanwise locations along the main body of the "smart" wing and at spanwise locations on the "smart" control surface. For the first full-span model entry, measurements were also made on the conventional flap and aileron [42]. The final Smart Wing test in this series of 4 acquired VMD data at only two spanwise locations on the "smart" control surface, and it was the first facility test in which an enhanced model deformation measurement system [51]

was used as a primary measurement system. This system was designed to enhance robustness, accuracy, adaptability and ease of use for facility operations personnel. For the final Smart Wing test, the VMD system was operated in an automated, full frame mode at 60 Hz and acquired over 2000 data points without a major malfunction.

Retro-reflective tape targets were used during all Smart Wing tests to ensure high-contrast imagery. The tape targets are 4 mil (0.004-in) thick. When a light source is positioned near the camera, the light retro-reflected from the tape targets can result in high-contrast images in which the targets are easily discriminated from the background. Such high-contrast images are amenable to automated image processing. For the final Smart Wing test, the hingeless control surface consisted of ten independently controlled segments that were used to produce various control surface shapes. Ten 0.5-in diameter retro-reflective tape targets were placed equally-spaced and centered on the lower surface of two of those segments (segments 3 and 6, shown in Fig. 7.1). There were five targets per segment, with one target of each segment row positioned on the main wing element side of the virtual hingeline (i.e., where a hingeline would be for a conventional control surface) of the "smart" control surface to serve as a reference point. The targets can be seen on the left side of Fig. 7.2. (Other targets visible on the figure were used in the first Phase 2 test.) A more detailed image of the targets on the control surface is shown in Fig. 7.3.

In-tunnel calibration of the VMD system was accomplished using a calibration fixture (a three-step plate). This fixture, which consists of an array of targets with known spatial coordinates, was initially used to determine lens distortion and principal distance, as well as to determine the orientation of the camera in the desired coordinate system. For this phase of the calibration, the fixture was placed to fill the field-of-view of the camera for

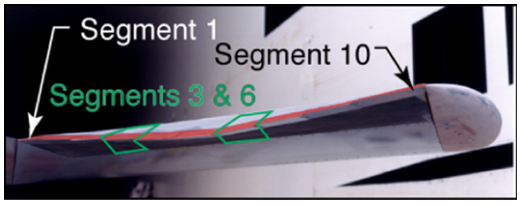

Fig. 7.1. Photograph of the "smart" trailing-edge control surface highlighting the segments monitored by VMD.

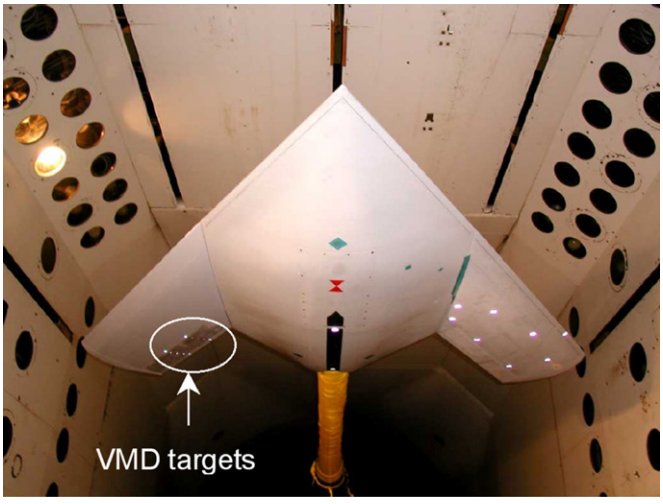

Fig. 7.2. Photograph of the lower surface of the model showing the VMD retro-reflective tape targets on the control surface of the "smart" wing.

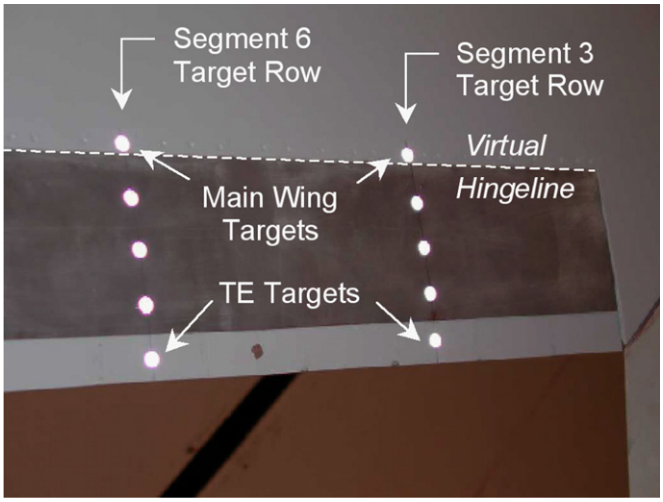

Fig. 7.3. Close-up photograph of the retro-reflective targets on the lower side of the control surface on the right/smart wing.

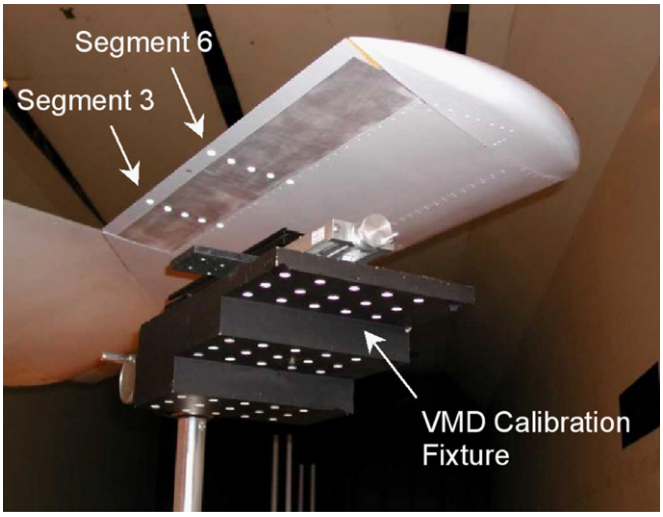

Fig. 7.4. Photograph of the VMD calibration plate/fixture mounted underneath the right "smart" wing.

the distortion computations and was not necessarily aligned to the model. Once the measurement system was set up with the proper view of the model, the calibration fixture was aligned to the control surface of the right "smart" wing (Fig. 7.4) in order to determine the exterior orientation parameters of the camera via photogrammetric space resection. For typical VMD applications where the deformation of the main wing element is the primary interest, the *X*-axis is aligned along the flow direction, the *Y*-axis is aligned along the span, and the *Z*-axis is up. However, for the final Smart Wing test in which the primary interest was the deformation of the control surface, the *Y*-axis of the calibration fixture was aligned with the virtual hingeline of the control surface with the model pitched to an angle of attack (AoA) of 1.6°. The *X*-axis of the orthogonal coordinate system was thus perpendicular to the hingeline at that angle. Consequently, the computed *Z*-coordinates for the targets were only calibrated strictly at model AoAs of 1.6°. At other model AoAs, the *Z*-coordinates would need additional corrections determined as a function of those angles.

After calibration, the VMD measurement process begins with the acquisition and digitization of a live video stream, which for the final Smart Wing test was automatically triggered by the

facility Data Acquisition System (DAS) at 60 Hz for 2 s as each data point was acquired. Once that video sequence was recorded, a blob analysis was used for target detection in the image. A gray-scale centroid calculation with the background level automatically removed provided sub-pixel precision. Single-view photogrammetry was used to determine the X (perpendicular to the control surface virtual hingeline) and Z coordinates (vertical) in the object space, given the known Y coordinates (parallel to control surface hingeline).

During the test, both static and dynamic time histories (2-s records at 60 Hz) of the shapes of segments 3 and 6 were automatically acquired and reduced. A typical plot of mean Z versus mean X of the control surface is presented in Fig. 7.5 for five different control surface deflections acquired at $M=0.6$, $q=150$ psf, and AoA$=1.6^\circ$, where M denotes Mach number and q is the dynamic pressure. This data represents the profiles of the lower surfaces of segments 3 and 6 of the "smart" control surface sampled at the five target locations on each. The ΔX separation of the targets on the main wing element associated with each segment to the target nearest the trailing edge of the control surface is around 5.5 in. The standard deviations of the 60 samples used to compute the means of Z for these targets are typically around 0.01 in.

Since the surfaces are curved as they deflect, any single angle used to describe the deflection of each segment is dependent on how the angle is defined and will not truly capture the external shape. Thus, instead of angular resolution, VMD accuracy will be discussed in terms of the short-term (back-to-back repeat data points) and within-run precision of the coordinate Z describing the contour of the lower surface. The difference, ΔZ, in mean Z between two repeat data points (separated by 45 s and acquired at $M=0.6$, $q=150$ psf, and AoA$=-2.4^\circ$) serves as an indicator of short-term repeatability. For these points, the short-term repeatability was generally better than 0.5 mil (0.0005 in) with a worst-case difference of 0.6 mil (0.0006 in). The standard deviation of 60 samples of Z taken over two seconds for an entire AoA-polar was less than 12 mil with a typical value less than 10 mil.

Wind-off bench tests performed prior to the final Smart Wing test indicated that a target placed on the main wing element near the virtual hingeline would remain essentially stationary during deflections of the control surface. This wind-off behavior was confirmed during the wind-tunnel entry and is demonstrated in Fig. 7.6, where the X and Z coordinates of segments 3 and 6 are plotted for uniform control surface deflections ranging from -14° to 20° with AoA fixed at -0.4°. Analysis showed that the standard deviations for the wing element targets in this data set were 0.8 mil and 2.9 mil for segments 3 and 6, respectively. The maximum Z-displacements for those two targets were 2.4 mil and 8.5 mil, respectively. However, wind-on VMD measurements did not observe the same main wing target stability. This is evident for the wind-on data presented in Fig. 7.5, where the movement of the two wing targets is up to 0.4 in. This motion was nearly 100 times greater than was seen in the wind-off case, and analysis showed that the motion was also over 300 times the standard deviation of mean wind-on repeat data, indicating a real effect.

Analysis of the VMD data for the wind-on conditions also revealed that both the main wing target and the target on the control surface segment nearest the virtual hingeline consistently had Z-deflections of the opposite sign from the remaining three targets nearer the control surface trailing edge for both segments. In the wind-off case, the control surface targets all demonstrated same sign deflections, with the wing target remaining almost stationary as previously discussed. These wind-on effects are most likely due to a combination of flow-induced wing twist and local reaction of the main wing element to the control surface actuation. These aerodynamic and aeroelastic effects could not be measured with traditional onboard gages alone, such as the rotary potentiometers used during the final Smart Wing test. This illustrates the value of both independent remote optical measurements and the acquisition of extensive wind-off data. To better emphasize the lower surface profiles, the VMD surface contour plots shown here have been normalized by zeroing the main wing element Z-coordinate. Fig. 7.7, for example, shows the normalized data plots corresponding to Fig. 7.5, respectively. The change in the profiles as the surfaces are deflected is clearly evident.

As previously mentioned, quantifying an angular value for the deflection of a contoured surface depends on how that angle is defined. The onboard rotary potentiometer angles were determined via a wind-off calibration using a 2-point arctangent computation in (X, Z) control surface centerline coordinates of the hingeline and the trailing edge. For comparison purposes, the videogrammetric angles were determined by four different methods for a wind-off control surface deflection sweep of -15° to 20°

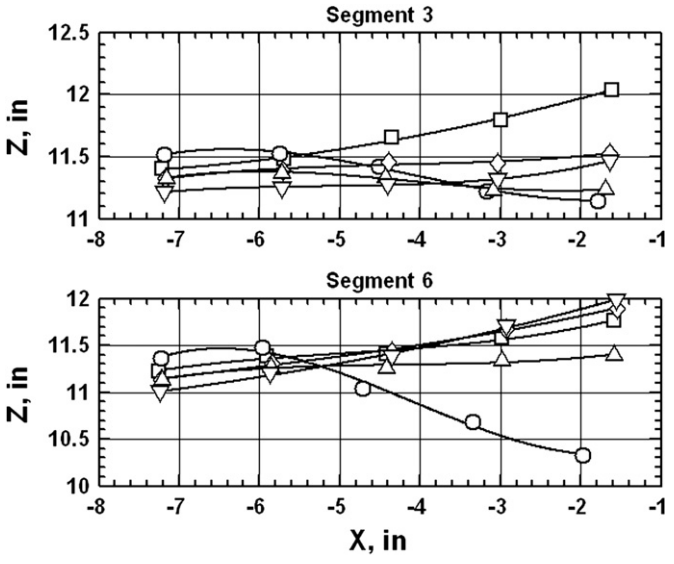

Fig. 7.5. Typical VMD plot layout showing five different control surface deflections acquired at $M=0.8$, $q=150$ psf, and AoA$=1.6^\circ$.

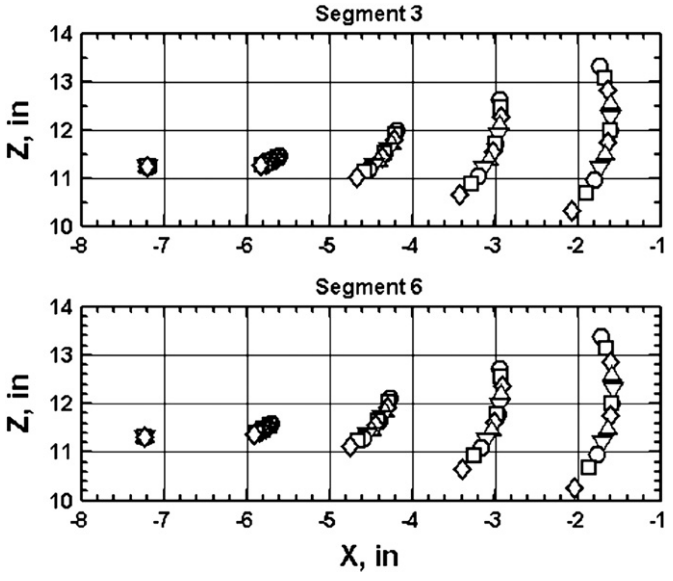

Fig. 7.6. Coordinates as smart control surface segments were deflected uniformly from -14° to 20° in the wind-off case at AoA$=-0.4^\circ$.

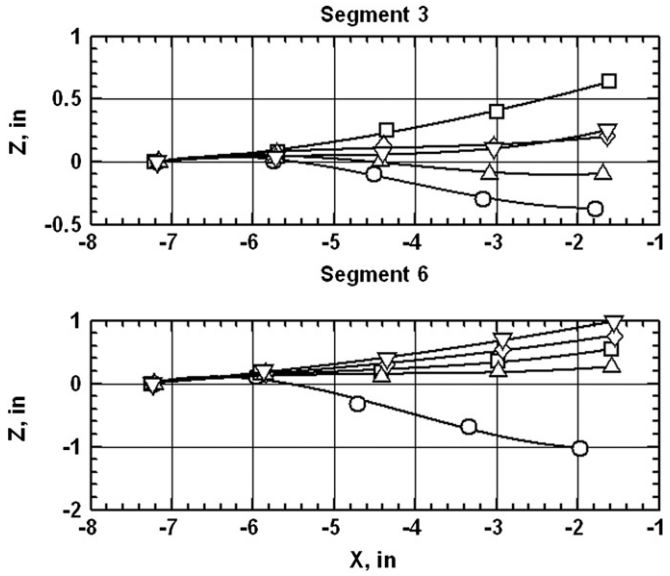

Fig. 7.7. Data plot corresponding to Fig. 7.5 with Z coordinates normalized by the main wing target Z values.

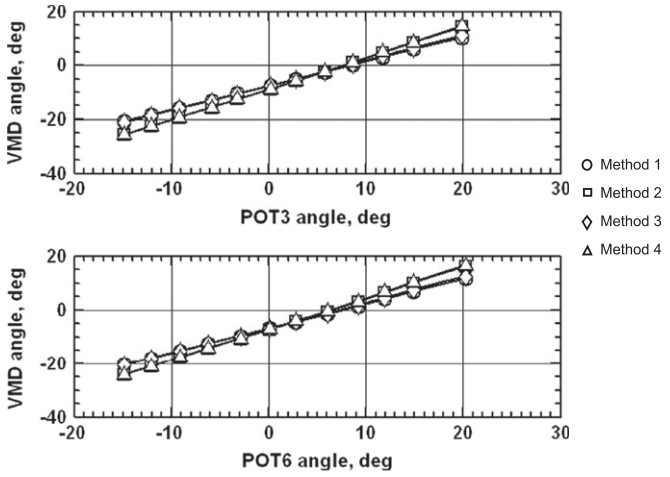

Fig. 7.8. VMD angles versus angles from onboard potentiometers for the wind-off uniform smart control surface deflections at AoA$=-0.4^\circ$.

at AoA$=-0.4^\circ$, with sign chosen to make trailing-edge down positive. Two of the methods consisted of 2-point arctangent computations in the (X, Z) coordinates using (1) the trailing-edge and main wing element targets and (2) the trailing-edge target and target nearest the hingeline, but still on the movable flap. The other two methods consisted of linear least squares fits to (3) all the targets and (4) all targets except the main wing element target. The resulting videogrammetric angles are plotted against the corresponding potentiometer angles in Fig. 7.8. Methods (1) and (3) yield very similar results, as do methods (2) and (4).

Note that there is a negative bias of about 8° for the VMD angles since they were measured from targets on the lower surface, which has a negative inclination to the control surface centerline used by the potentiometers. Compared to the potentiometer data, methods (1) and (3) tend to underestimate the flap segment angle by about 6% to 11%, whereas methods (2) and (4) tend to overestimate by about 13%. However, due to the high precision of the videogrammetric data, calibration based on the potentiometers at a given AoA is possible. A fifth-order fit to the data yields residuals with a standard deviation of 0.11° and 0.08° for segments 3 and 6, respectively. In most cases, the residuals based on the four methods are equal to within 0.01°, with worst-case agreement of 0.02°. Thus the four methods are essentially equivalent after calibration. The maximum deviations of the residuals after calibration are 0.3° and 0.2° for segments 3 and 6, respectively. Thus the videogrammetric data can be calibrated to within several tenths of a degree if a single parameter (such as segment deflection angle as defined by the potentiometers) is desired to describe the flap deflection at each segment. Note that the linearity and repeatability specifications of the rotary potentiometers are 0.1% and 0.01% of full scale (340°), or 0.34° and 0.034°, respectively. Thus it is expected that a large fraction of the residuals may be due to inaccuracies in the potentiometers. Since the repeatability of the videogrammetric data is around several hundredths of a degree, it is possible to calibrate to those levels at specific AoAs and control surface settings.

7.2. In-flight aeroelastic deformation

A low-cost, adaptable videogrammetric method was developed for the measurement of static and dynamical aeroelastic deformation of aircraft wings during flight testing [27]. The method was adapted from a proven technique used in wind tunnel testing. Measurements included the change in wing twist and deflection as a function of time of an F/A-18 research aircraft at NASA's Dryden Flight Research Center (DFRC). The Active Aeroelastic Wing (AAW) F/A-18 research aircraft at DFRC is shown in Fig. 7.9. The camera pod housing the Flight Deflection Measurement System (FDMS) and video camera can be seen on the top of the fuselage overlooking the left wing. The camera pod as viewed from the right side of the aircraft is shown in Fig. 7.9, with a close-up of the camera pod highlighting the FDMS and video camera viewports also depicted in Fig. 7.9. A planform of the aircraft showing the locations of the video camera, FDMS receivers, and FDMS targets (indicated with red circles) is shown in Fig. 7.9. The AAW F/A-18 project envisioned the application of in-flight structural deflection measurement from its earliest formation. Provisions were designed in the test aircraft to accommodate the FDMS. This included a dorsally mounted receiver pod with window, 16 infrared LED targets on the upper left-hand wing surface with lead wires to a target driver box, a control unit box, power supplies, data telemetry interface circuit, and a cockpit-mounted on/off switch. As the FDMS installation was being designed, additional provisions were built in to support a developmental deflection measurement system. These provisions include additional space in the FDMS receiver pod and a longer window. Additionally, a pod heater was provided. These additional provisions made the AAW aircraft an ideal test-bed for the flight testing of new deflection measurement approaches.

There are several notable differences between measuring wing deformation of a wind tunnel model compared with an aircraft in flight. For instance, the in-flight data camera would likely be mounted on the fuselage of the aircraft, thus the view presented to the data camera would be essentially the same throughout testing (except of course for any deformation or scale changes due to varying refractive index). The measurement of wing deformation in flight is closer to a differential measurement, can make better use of the available image area, and is affected less by rigid body motion because the camera is on the body (fuselage). Dynamics may also be less of an issue for in-flight testing because the camera moves with the fuselage, thus any dynamics common to the fuselage and wing would tend to cancel. Differences also occur with targeting. The wind tunnel model is typically viewed at an angle to the wing of about 30°, whereas for aircraft in flight, the data camera located on the fuselage would likely have an angle-of-view to the wing closer to 10° or less. Because the light return from retro-reflective material drops significantly as the

F/A – 18 Active Aeroelastic Wing research aircraft.

Camera pod and left wing.

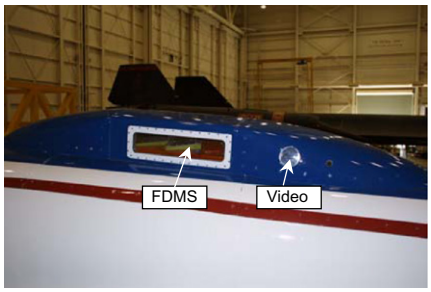

Camera pod viewports.

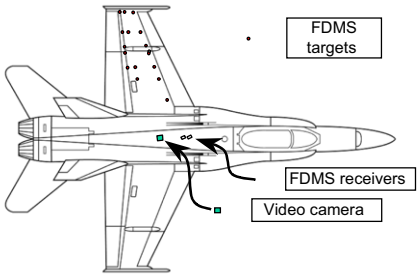

Planview with video camera, FDMS receivers and targets (circles) indicated

Fig. 7.9. F/A-18 Active Aeroelastic Wing research aircraft and cameras/targets positions.

angle of incidence moves away from normal, the retro-reflection for aircraft with a shallow angle of incidence would be reduced. In addition, the space required for a light source for retro-reflective targets, along with its additional wiring, mounting, and operational concerns, limits the desirability of an additional light source for in-flight testing. The use of natural features or passive targets that do not require additional wiring or special mounting is very desirable for in-flight testing. Flight-hardened hardware is a major concern for any in-flight test technique. Flight hardware must be able to endure a variable and hostile environment and still continue to function. Ambient temperature can vary over a range of up to 270 °F or more. Air pressure can go so low as to allow electrical circuits to arc. Structural vibrations can sometimes shake electrical or mechanical components to pieces. Moisture can be present as well as jet fuel. Further, flight systems must be able to run unattended.

In order to apply single-camera, single-view photogrammetry, the Euler angles (ω, ϕ, κ) and the effective perspective center (X_c, Y_c, Z_c) of the data camera must be determined in the aircraft coordinate system. This was accomplished with photogrammetric space resection. The principal point, (x_p, y_p), was approximated as a fixed location near the center of the digital image extracted from the DVD recordings at a resolution of 704 horizontal pixels by 480 vertical pixels. In pixel space, the coordinates for (x_p, y_p) were taken to be (352, 240) pixel, which during the conversion from pixel space to millimeters on the image plane corresponded to (x_p, y_p)=(0, 0). The principal distance was estimated based on an assumed focus toward the outboard portion of the wing and an effective focal length.

The FDMS targets were used as reference for camera resection because their locations had been measured with a precision theodolite before flight testing began. The effective pixel spacings S_h and S_v were adjusted from repeated photogrammetric resections until the computed location of the video camera from resection was in reasonable agreement with its assumed location (to within a tolerance of several centimeters). The horizontal pixel spacing was further adjusted to minimize image plane resection residuals to yield the reasonable estimates of S_h, and S_v. Once the start values for the resection were tweaked closer to the correct values, the correct global minimum was found.

The standard resolution flight-hardened video camera normally used for surveillance was used to record the image sequences for processing. This camera is normally used for surveillance of the left wing, provided the image sequences for processing. Once all the camera orientation parameters are known, two of three coordinates (with the third coordinate known) can then be computed from a single-camera view. To determine deflection, the vertical coordinates at a reference condition are subtracted from the vertical coordinates at the condition of interest. Angles are determined from the slope of the computed coordinates in chordwise planes at the various spanwise locations where targets or suitable image patches exist. Local angles at various span stations at the reference condition are subtracted from the condition of interest to yield the change in angle (induced twist) due to aeroelastic loading.

A total of 361 digital images at a resolution of 704×480 pixel were extracted from a DVD image sequence recorded from a flight-hardened video-monitoring camera that views the left wing of the AAW F/A-18 research aircraft. Of these, 31 images were from a 1-s time history while the aircraft was on the runway. The remaining 330 images covered the aircraft from level flight (M=0.95, q=750 psf, altitude=15,000 ft) through a 90° bank-and-return maneuver over a time period of 11 s. Because some of the FDMS LED target housings, especially outboard toward the trailing edge of the wing, were barely distinguishable from the background, the image locations of the targets for the three images were manually selected. Although the red, green, and blue components of each digital image could be analyzed separately, the red component was found to have highest contrast for most of the images and was used for further analyses. The estimated precision of manual image coordinate location is at best a pixel or so whereas centroiding of high-contrast targets with proper background removal can yield a precision of 0.01 pixel.

Fig. 7.10 shows a vector representation of the relative Z-deflection of the 16 FDMS targets from a level flight condition

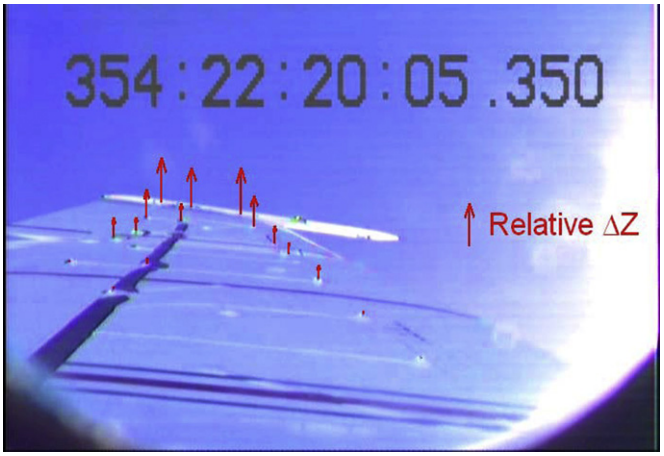

Fig. 7.10. Relative *Z*-deflection from level flight to maneuver.

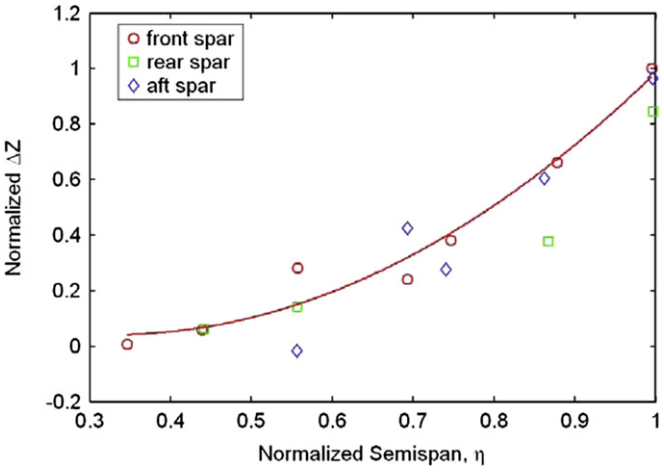

Fig. 7.11. Normalized deflection along the semispan location.

to a maneuver. The computed *Z*-values of the level flight image were subtracted from the maneuver image to arrive at the ΔZ-values. For Fig. 7.10, the deflection represented by the arrows is not influenced by the distance of targets from the camera. In other words, the amount of deflection indicated by the arrows is independent of where on the image the arrows are located. The most inboard targets exhibit very little deflection, as expected. The deflection increases as one moves outboard toward the wing tip. The housings nearest the leading edge and closest to the front wing spar had higher contrast, with corresponding better precision than the rest of the housings. The corresponding normalized (to maximum deflection) ΔZ is plotted in Fig. 7.11 versus the normalized semispan location. The solid line in Fig. 7.11 is a second-order polynomial fit to the seven targets nearest the leading edge, indicated by circles, which lie along the front wing spar. The midchord row targets (near the rear spar) are indicated with squares and the targets nearest the trailing edge (aft spar) are indicated with diamonds. Although the scatter in these data is relatively large, it does indicate the correct trend and illustrates the potential of useful measurements given low-contrast non-ideal targets, even with low-resolution video. It is estimated that an improvement approaching a factor of 10 could be achieved in data precision with larger, better defined, high-contrast targets, even with relatively low-resolution video recording.

The wing tip angles, while on the runway, in level flight and at maneuver, are shown in Fig. 7.12. Flow is from left to right. The

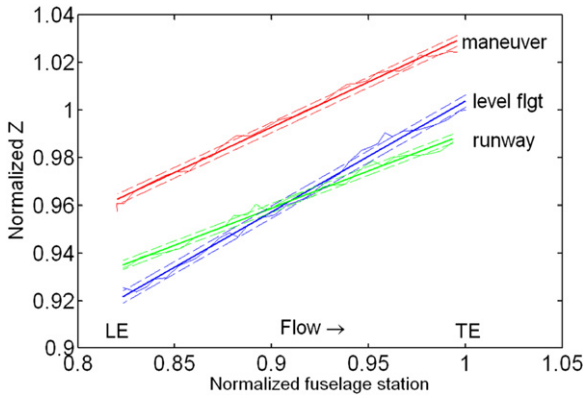

Fig. 7.12. Launcher rail relative position for runway, level flight, and maneuver.

solid lines are first-order linear least-squares fits to each (*Y*, *Z*) data set for each of the three digital images. The dotted lines are ± 1 standard deviation of the polynomial fits. The characteristic negatively induced wing twist due to aerodynamic loading is evident upon comparing the runway data with level flight data. Very little vertical deflection at the wing tip is noted when comparing runway with level flight data. The main effect of the maneuver is upward deflection of the wing tip and a slight increase in wing twist at the tip. The relatively stable image locations (and corresponding stable spatial object locations) of the most inboard targets give credibility that the nature of the wing tip deformation is effectively depicted in Fig. 7.12 rather than camera movement, which would have caused image plane motion of the most inboard targets as well.

7.3. *Determining load from beam deformation*

The feasibility of determining steady-state aerodynamic load in wind tunnel testing has been studied based on beam (sting) deformation measurements using a two-camera videogrammetic system as an alternative to internal strain gauge balances [68]. The deformation of a cantilever beam was utilized in this study to calculate the normal force and pitching moment. Here a model support string is considered as a cantilever beam. Fig. 7.13 shows a three-force beam with targets and a calibration rig and two-camera videogrammetric system for beam deformation measurement. Data reduction methods were developed to extract the normal force and pitching moment from beam deformation data. The local displacement δv and the slope change δv_x of a cantilever beam are

$$\begin{pmatrix} \delta v \\ \delta v_x \end{pmatrix} = \begin{pmatrix} x^3/6EI & -x^2/2EI \\ x^2/2EI & -x/EI \end{pmatrix} \begin{pmatrix} F \\ M_c \end{pmatrix}, \tag{7.1}$$

where M_c is the moment with respect to a moment center. Eq. (7.1) gives a linear relation between the deformation (δv, δv_x) and the force and moment (F,M_c), indicating that the force F and moment M_c depend on the local displacement δv and the change of slope δv_x. Therefore, (F,M_c) can be determined from measurements of (δv, δv_x). Fig. 7.14 shows the local displacement and slope change (δv, δv_x) as a function of the normal force for a brass beam at four different loading positions. It has been found that the dependence of both the local displacement and slope change on the pitching moment is linear when the moment center is suitably chosen. The linear relations are clearly shown in Fig. 7.15 for a brass beam, where the moment center is determined by an optimization scheme to minimize the fitting error. This linearity is utilized in the simple model method for data reduction. Typically, the relative errors in extracting the normal force and pitching moment are

roughly within $\pm 10\%$ and $\pm 5\%$ in the calibration ranges, respectively.

Another data-reduction method is based on global deformation. From Eq. (7.1), one knows that the displacement δv along the beam axis can be described by the theoretical relation $\delta v(x)=a\,x^2+b\,x^3$, where x is the coordinate along the beam axis and the coefficients a and b are related to F and M_c. In reality, however, the relation between (a, b) and (F,M_c) is not as simple as that given by Eq. (7.1). The empirical relations are symbolically expressed as $F=f_1(a,b)$ and $M_c=f_2(a,b)$. For a given data point (a,b), a local 2nd-order polynomial fit to a group of calibration data points is used to recover (F,M_c). The method based on global deformation profile is used to recover the normal force and pitching moment for a beam. Fig. 7.16 shows measured deformation profiles of a brass beam for different loads. These measured data can be well fit by the theoretical solution $\delta v(x)=a\,x^2+b\,x^3$. Compared to the first method based on the local displacement and slope change, the method based on the global deformation profile gives smaller relative errors in the normal force (within $\pm 5\%$) and pitching moment (within $\pm 3\%$) for the brass beam.

A steel sting-model combination used in the Unitary Tunnel at NASA Langley was calibrated, as shown in Fig. 7.17. In calibration tests, the maximum displacement of the sting is about 0.03 in and the maximum change of the local bending angle is about 0.23°.

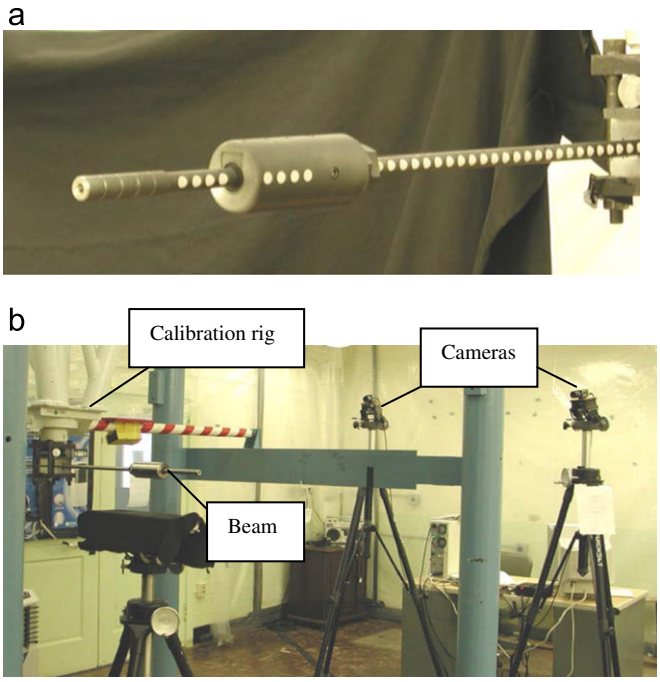

Fig. 7.13. (a) Three-force beam with targets, and calibration rig, and (b) two-camera videogrammetric system.

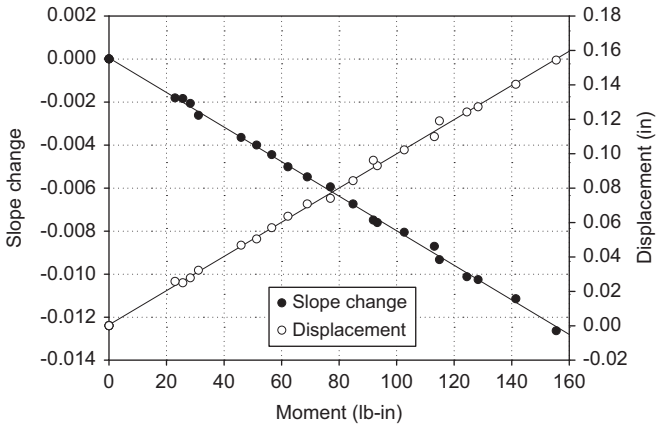

Fig. 7.15. Local displacement and slope change as a function of the pitching moment for a beam.

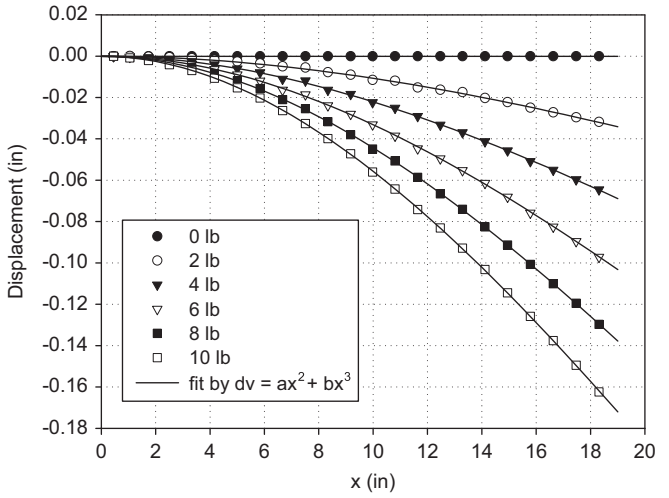

Fig. 7.16. The measured deformation profiles of a beam and the fit by $\delta\ v(x)=a\,x^2+b\,x^3$ at the loading position $L=28.069$ in.

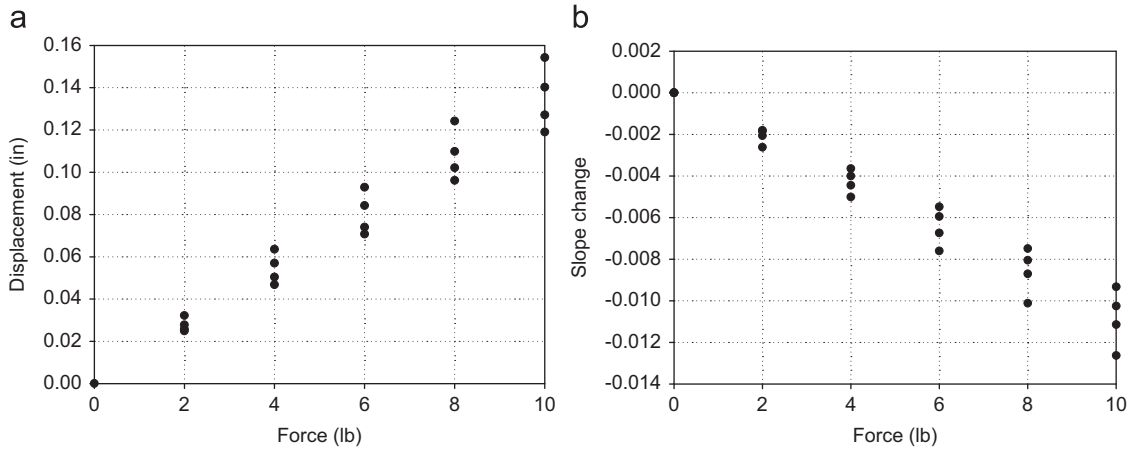

Fig. 7.14. Local displacement and local slope change as a function of the normal force at four loading positions for a beam.

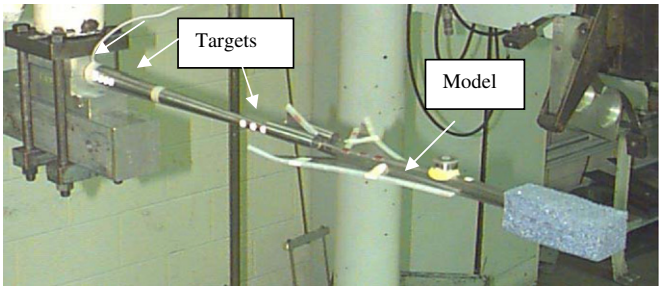

Fig. 7.17. The sting-model configuration with targets.

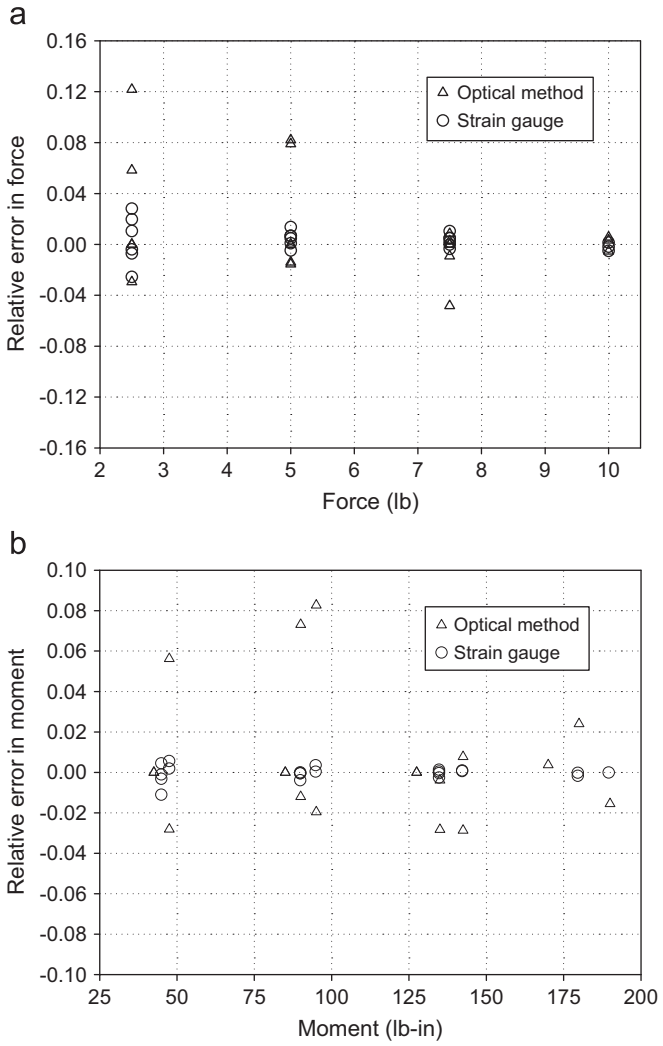

Fig. 7.18. Comparison between the optical method and strain gauges in measurements of (a) the normal force and (b) pitching moment for the steel sting-model configuration.

Two strain gauge bridges were also installed on the sting for measurement of the normal force and pitching moment, allowing a direct comparison between the strain gauge method and the optical method. The local deformation quantities (δv, δv_x) were measured using the two-camera videogrammetric system. The method based on the local displacement and slope change was used to determine the normal force and pitching moment. As shown in Fig. 7.18, the relative errors in the normal force and pitching moment obtained by the optical method are about $\pm 5\%$ in comparison with $\pm 2\%$ given by the strain gauges.

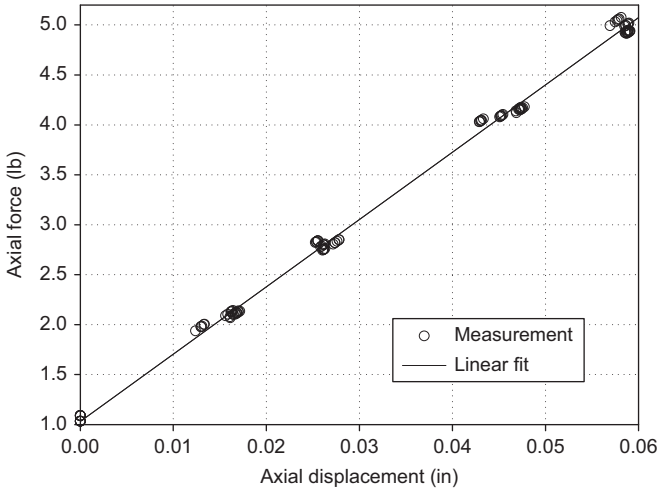

Fig. 7.19. The axial force as a function of the axial displacement.

In order to measure the axial force along with the normal force and pitching moment, a three-force beam was designed and fabricated. As shown in Fig. 7.13(a), the three-force beam consists of a simple beam and a spring/bearing device that only allows translational motion along the beam axis. A number of retro-reflecting targets are placed on the simple beam for measuring the beam deformation. Four targets are placed on the spring/bearing device as a reference and another four targets are placed on the movable shaft for measuring the axial translational motion relative to the reference targets. Fig. 7.19 shows the linear relation between the axial force and the measured axial displacement. The measurement errors in the normal force, pitching moment and axial force are $\pm 4\%$, $\pm 3\%$ and $\pm 8\%$, respectively.

7.4. Dynamic aeroelastic deformation

Dynamic deformation of a rectangular plate (wing) placed vertically in flow was measured and further the dynamic force was extracted by Roy et al., [91]. The plate experienced flutter as a dynamic instability [11]. Flutter of a plate is typically described by a combination of the bending and torsion modes. As shown in Appendix C, the displacement w of a vibrating plate is given by an expansion based on the eigenfunctions $w_r(x,y)$ $(r=1,2,3\ldots)$. The first nine eigenfunctions or mode shapes are illustrated in Fig. 7.20. The main eigenfunctions, particularly the first and second bending modes and the first torsion mode, can be extracted from videogrammetric deformation measurements [91,96].

A high-speed two-camera videogrammetric system was used, consisting of two Canadian Photonic Labs MS1000 CCD cameras with 8 mm lenses and two variable intensity light sources directed through fiber optic bundles. The CCD cameras were operated with a resolution of 640 by 480 pixel at about 140 frames per second. The system is capable of tracking light targets on a dark background or dark targets on a light background. For this test, retro-reflective targets were used on a flat black plate, scattering light predominantly back to its source. The two light sources supplied the lighting through fiber optic bundles. The end of the bundles was attached to the top of the cameras, which allowed the light to be reflected from the targets into the camera. The ability to adjust the light intensity allowed the amount of reflected light to be maximized without creating over saturation of the images. The cameras are calibrated by placing a block with known target coordinates in front of or in place of the model.

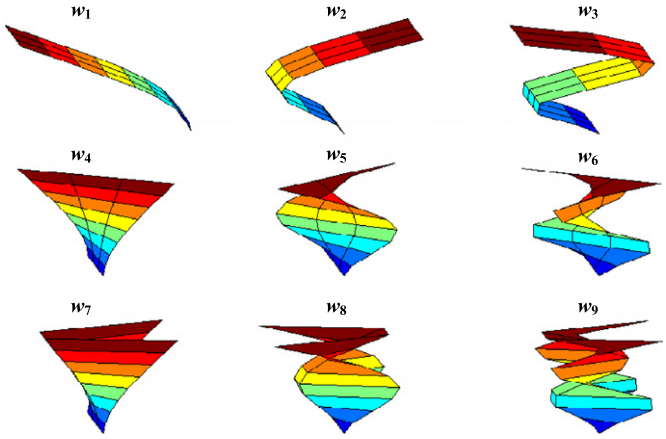

Fig. 7.20. Theoretical mode shapes.

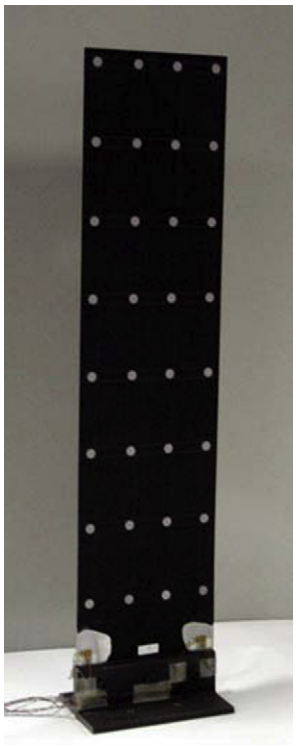

Fig. 7.21. The 24-in flutter test plate.

The orientation of the calibration block determines the reference coordinate system for all tests using that calibration block.

All results are for three cantilever aluminum plates mounted vertically. Fig. 7.21 shows the 24-in plate. All plates have a chord of 6 in and thickness of 0.04 in. The plates have lengths of 24, 18, and 12 in and contain 32, 28, and 24 targets, respectively. Four fictitious targets were added in the calculations to represent the base of the plates, which was clamped between two pieces of angle. The base was securely bolted to the turntable on the floor of the wind tunnel that was used to adjust the plate to zero angle of attack.

First, using an impact hammer to excite each of the plates (impulse excitation), the combination of natural frequencies was captured by the videogrammetric system. To determine the damping factors ζ_r and the natural frequencies ω_r, the method for the impulse transient solution is utilized to determine the time-dependant amplitude, $\eta_r(t)$, for each of the modes. The following relation $\eta_r(t) \propto \exp(-\zeta_r \omega_r t)\sin\omega_{rd} t$ is then used. The use of Fourier Transform analysis for $\eta_r(t)$ gives the frequency of damped oscillation, $\omega_{rd} = \omega_r(1-\zeta_r^2)^{1/2}$. It is assumed that the exponential decay rate is $\zeta_r\omega_r$, ignoring aerodynamic damping effects. Using this assumption and knowing the natural frequency, the damping factor, ζ_r, can be determined. In general, once ζ_r and ω_r are known, the generalized force, $N_r(t)$, can be determined from the measured magnitudes $\eta_r(t)$ of forced vibration by using Eq. (C7) in Appendix C.

The time-dependant amplitudes of the first and second bending modes [$w_1(x,y)$ and $w_2(x,y)$] and the first torsion mode [$w_4(x,y)$], which are recovered from the impact hammer tests, are shown in Fig. 7.22 for the 24-in plate. The plot on the left shows a global view of the amplitudes of the three modes while the plot on the right focuses on the second bending and first torsion modes. The natural frequencies measured for each of the plates are summarized in Table 7.1 in comparison with the theoretical values of Warburton [107]. The theoretical frequencies are systematically higher than the measured values. Warburton [107] noted that the greatest errors occurred for cantilever plates and the calculated frequencies for a cantilever plate with an aspect ratio of 5 were 27 and 12 percent too high for the first two bending modes, respectively. Fig. 7.23 shows typical power spectra for the three mode amplitudes for the 24-in plate. For more accurate comparison, a laser velocimetry system was used to compare natural frequency results. This system measures the Doppler shift of the laser wavelength to determine the velocity of the object. The results agreed within 2% with the videogrammetric measurements.

It was experimentally determined in a low-speed wind tunnel that the plate would sustain flutter over a range of speeds beginning at the critical flutter speed. Beyond this range, the plates become stabilized. The flutter speed range for each of the plates was examined. It was assumed that the flutter mode for each plate could be represented by the modes for which natural frequencies and damping factors were found. To investigate the effect of velocity on flutter, tests were performed at several velocities within the range of sustained flutter. Fig. 7.24 shows the effect of velocity on the flutter frequency of each of the plates. The effect of velocity on the flutter frequency of each of the plates was studied. Interestingly, the flutter frequency of the 18-in and 12-in plates increases at a similar rate with increase in velocity. The 24-in plate increases slightly then begins to decrease in frequency. It was expected that the flutter frequency would increase as the aspect ratio decreased. Fig. 7.25 shows the deformation of the 24-in plates through one oscillation at the wind speed of 44.05 ft/s. The recovered distributed force using Eq. (C8) in Appendix C is represented by the color scale superimposed on the plate. The deformation is greatly exaggerated by the scaling of the axis. The animation of the deformation easily shows the contribution of the modes chosen to model the flutter in each case, where the elapsed time between each frame is 0.005 s.

7.5. Aircraft and spacecraft impact testing

Non-intrusive optical measurement techniques that are based on the principals of digital close-range photogrammetry are providing valuable analytical support for studies conducted on impact dynamics research vehicles. The vehicles being mentioned have all been tested at the Landing and Impact Research Facility (LandIR) at NASA Langley Research Center in Hampton, Virginia. This facility, also known as the gantry, is a 240-ft high A-frame structure used for testing full-scale and sub-scale crash vehicles. It was originally built in 1965 to support the NASA Apollo Space Program and to simulate mock landings on the moon. More recently, the gantry is known for crash testing aircraft for the sake of air safety. In addition to this line of work, since the recent retirement of the Space Shuttle, the gantry is also being used to

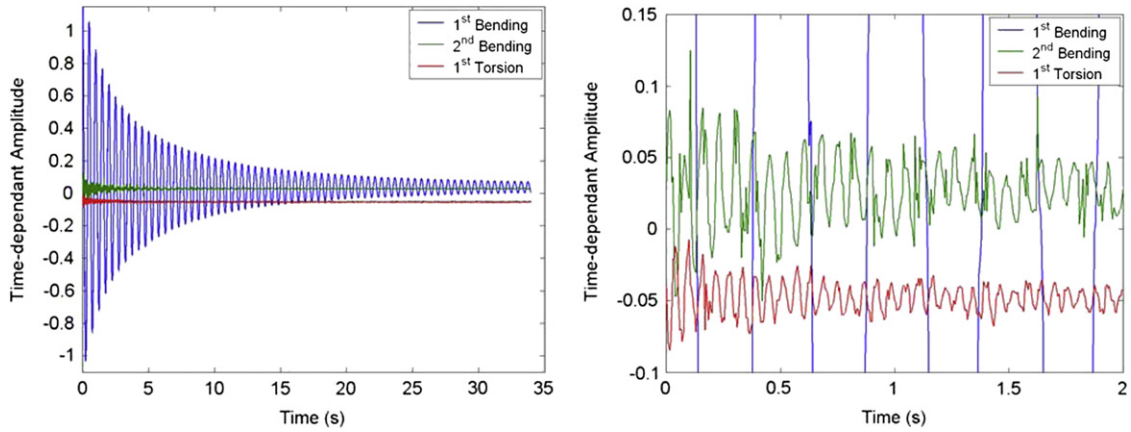

Fig. 7.22. The amplitudes of the first and second bending and first torsion modes of the 24-in plate. Note that the left figure is an enlarged view to show the second bending and the first torsion mode.

Table 7.1
Natural frequencies (Hz).

	Videogrammetry	theoretical value
24-in plate		
First bending	2	2.389
Second bending	13.42	14.964
First torsion	16.667	23.613
18-in plate		
First bending	3.54	4.248
Second bending	23.33	26.603
First torsion	22.833	31.609
12-in plate		
First bending	8.53	9.558
First torsion	35.42	47.945

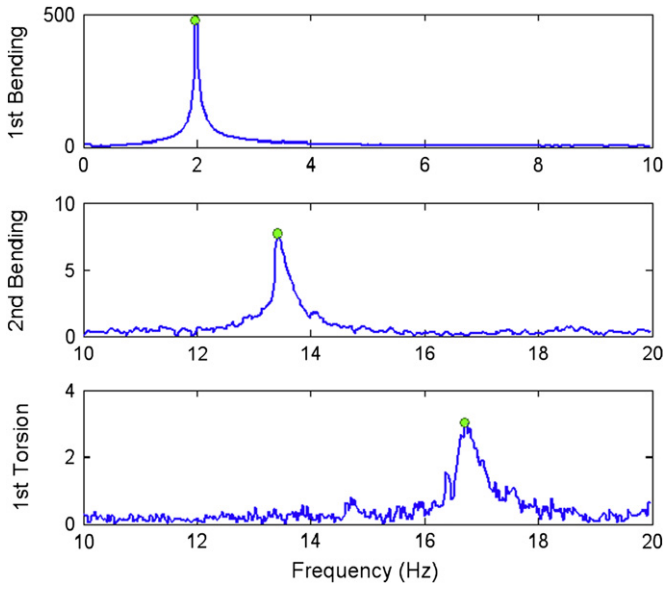

Fig. 7.23. Power spectra of the first and second bending and first torsion modes for the 24-in plate.

test new crew exploration space vehicles to ensure their safe returns back to earth. This has included both, land and water landings over a variety of landing scenarios.

Measurements being made at the gantry have included the resolution of 2D and 3D object space coordinates, determined from 2D images. Most of this imaging work has been obtained from high-speed cameras that record the flight and impact sequences. Numerous Phantom (Vision Research, Inc.) high-speed video cameras are generally used at frame rates of 1000 frames per second and image resolutions up to 1632×1200. For applications of the 2D measurements at the gantry, cameras are placed perpendicular to the pendulum drop swing plane of the test article for side views, and parallel to the drop swing plane for front and rear views. Each camera is mounted on its own tripod and leveled in two directions with bubble levels to help ensure near orthogonal views. All of the cameras are also temporally synchronized and simultaneously triggered to begin the video acquisition. The test articles are outfitted with diffuse white targets on a black background or black targets on a white background, depending on the contrasting color scheme of the test article. Automated frame-by-frame target tracking is used where the position of each target within each video frame is determined to $\sim$0.1-pixel accuracy by computing the grayscale-weighted target centroid location. On occasion target views can be disrupted by gantry guide wires, tether ropes, and dust debris that is kicked up on impact. For this, additional custom target centroid coding was developed to handle the anomalies.

Measurements from 2D target tracking make use of orthogonal camera setups where the test article and its targets are not rolling or yawing out of plane during flight. A known target separation between a pair of reference targets on the test article is used to determine the scaling multiplier that converts image plane pixels to engineering units. The image scaling multiplier can be determined from any video frame, and for the gantry testing the chosen frame is at the time of impact. A good choice for a pair of reference targets are targets situated on the centerline cross-section of the vehicle that represent the outer most target pair. Target separations are often determined to within a few thousandths of an inch using a commercial photogrammetry measurement system, VSTARS, developed by Geodetic Systems Inc. However, linear types of (pullout) scales can also be used to measure target separations to within an estimated ± 0.2 in (0.5 cm). These errors in length measurement of the reference target spacing can be larger than normally expected when there is no clear line-of-sight path from target-to-target due to blockage by model structural components. An example of this, as seen in Fig. 7.26, is a full-scale gantry drop model being used to test a prototype airbag landing assembly for the NASA Orion Crew Exploration Vehicle (CEV). The targets on this vehicle labeled 1 and 2 are the reference targets and the line-of-sight between them is being blocked by part of the vehicle the structure, in the vicinity of targets 10, 11, and 12. Hard to measure targets with structural blockage, such as these, is a classic case for when a

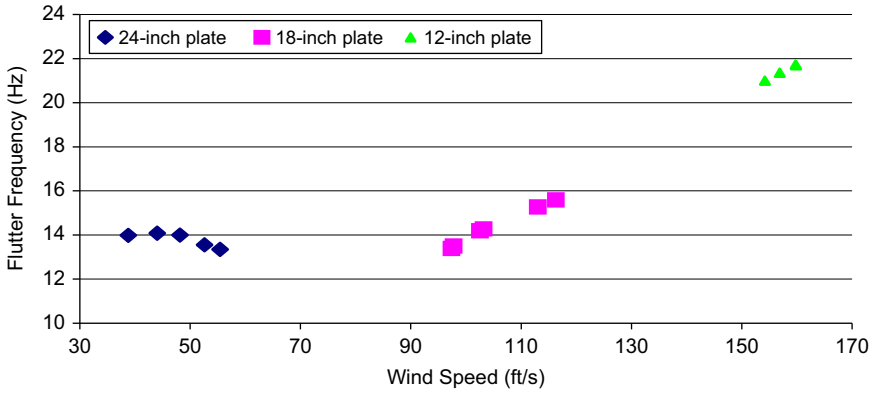

Fig. 7.24. Flutter frequency vs. wind speed.

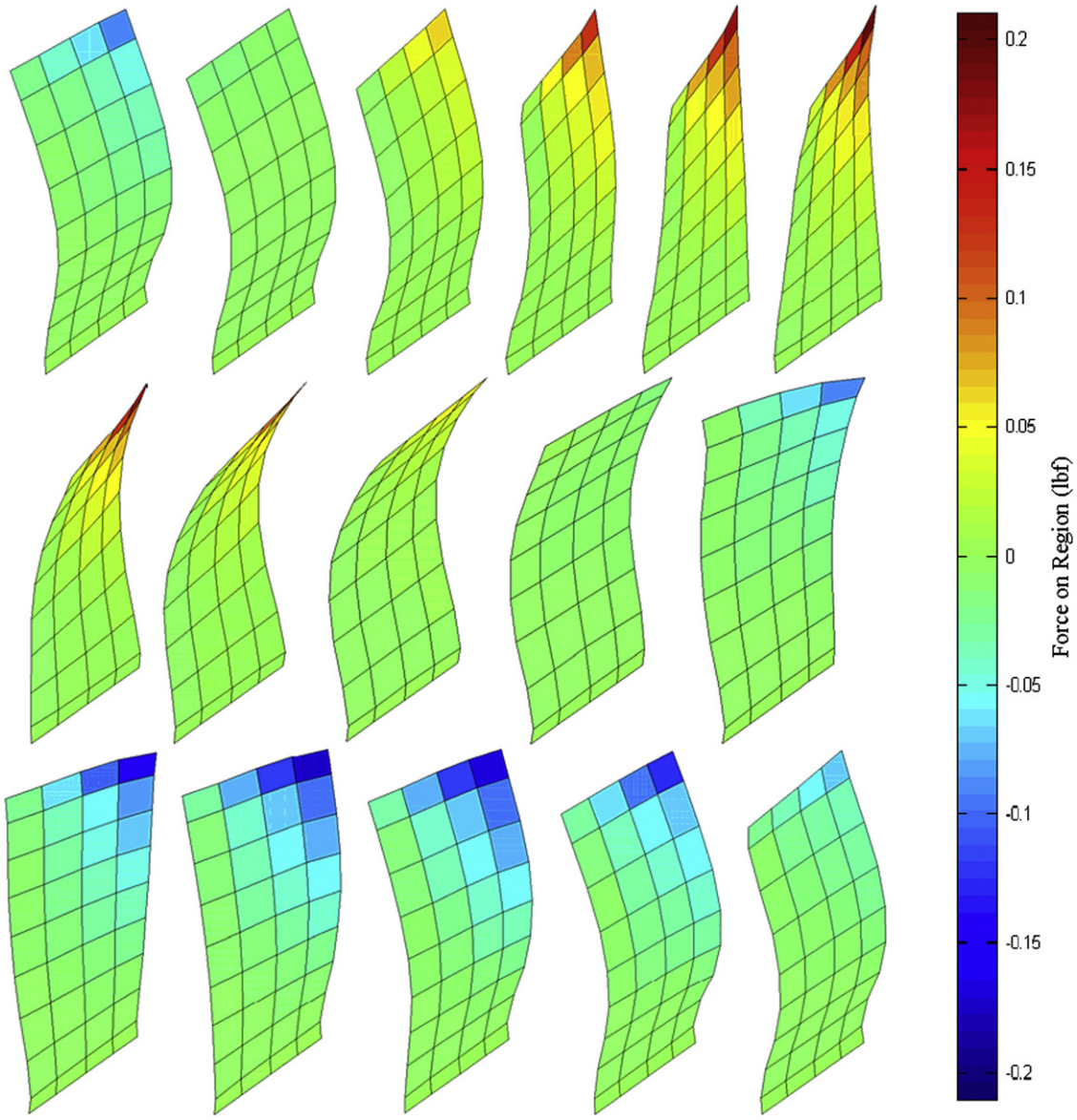

Fig. 7.25. The 24-in plate flutter reconstructed from videogrammetric measurements and force distributions.

system such as VSTARS becomes the better alternative when making the reference measurements.

An application of 3D photogrammetry is being used at the gantry, LandIR facility that uses two cameras in a stereo pair setup, typically separated by approximately 30-ft while tracking test articles at distances of approximately 60-ft. The advantage to using a stereo pair of cameras over a single camera application is the third dimension (in stereo) is triangulated, which gives a full

6 degree-of-freedom solution. Both full field strain digital image correlation (DIC) photogrammetry and target tracking photogrammetry are currently in use. The photogrammetry system uses a grid of coded targets when camera calibrations are being performed. This grid is photographed at various locations by each camera before the start of any new measurements to ensure the respective measurement volume is calibrated. Calibration and resection techniques use a least-squares method to locate the cameras in space, while also providing a calibrated volume for measurement. Calibration coded target grids are custom made and usually reside in the camera field of view during a test. There are two main grid platforms in use at the LandIR facility. The first is a 48-ft long by 37-ft high grid permanently mounted on the gantry large white backdrop mainframe. Also laid out on the face of the white backdrop is a 1-m lattice, typically used to support land impacts. The second coded grid platform is a 40-ft long by 12-ft high arrangement mounted in a semi-permanent structure for use with the Hydro Impact Basin (HIB) Testing. Fig. 7.27 shows the two gantry calibration grids.

Photogrammetry methods have been used to successfully track aerospace-related vehicles such as the Orion/MPCV Boilerplate Test Article (BTA) during a series of water impact tests at the LandIR HIB (see Fig. 7.28). When tracking the impact conditions, pitch, roll and yaw angle calculations of the test vehicles are a particular interest of the researchers. The angle measurements are extracted by examining the differences between created artificial lines on the vehicle and a horizontal line created from the calibration panel. By using a combination of horizontal and vertical lines with projected angles, all three impact angles can be resolved. Fig. 7.29 shows an example of the pitch angle time history for a BTA water impact test.

Full-field strain digital image correlation photogrammetry has been demonstrated on the crash test of a small MD-500 helicopter at the NASA gantry [60]. The purpose of this test was to evaluate an external deployable energy absorbing concept in which the outcome of much of the airframe deformation was of interest. Two,

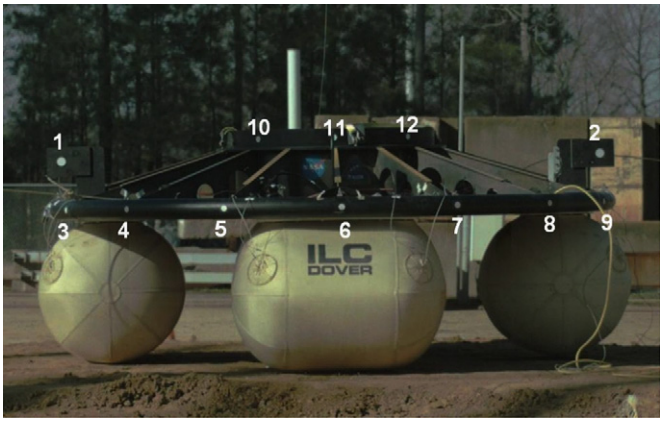

Fig. 7.26. Photogrammetry targets on airbag drop model and a typical target numbering convention.

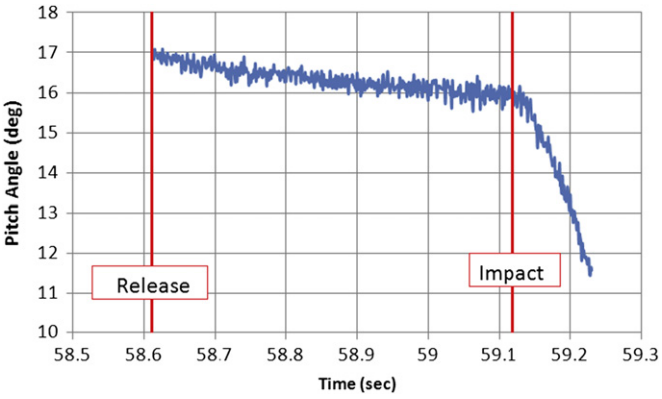

Fig. 7.29. Pitch angle time history for BTA water impact test.

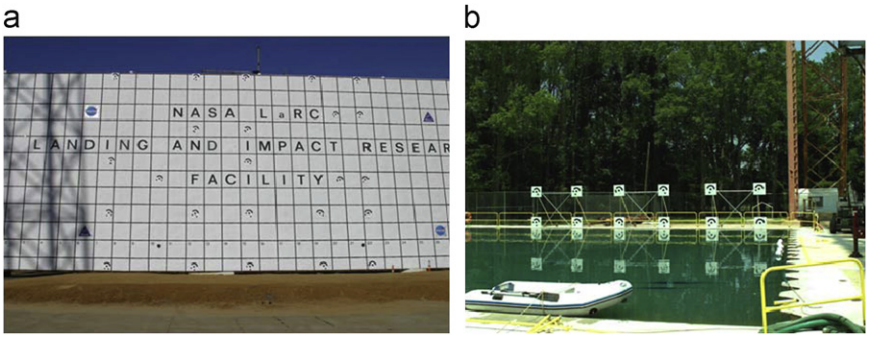

Fig. 7.27. Photogrammetry coded target calibration grids, (a) the land landing grid, and (b) water landing grid (right).

Fig. 7.28. Two different camera perspectives of two different water impact BTA tests.

nearly identical full-scale crash tests using the same MD-500 fuselage body were successfully demonstrated (see Fig. 7.30), with and without deployable energy absorbers (DEA). For this test, a small portion of the tail section was painted with a typical speckle pattern for use with the DIC. Fig. 7.31 shows a sample fringe plot of major strain during impact. Target tracking photogrammetry has been demonstrated on multiple types of full- and sub-scale impact vehicles [64]. Each discrete target is tracked throughout the impact, and the results can be reported as a time history of the rigid body average of all of the points, or they can be reported for each point individually. Results typically include impact velocities, and however if large amounts of deformation occur (as with the MD-500 helicopter mentioned above), the relative change between points can also be reported. Fig. 7.32 demonstrates the velocity time history for the MD-500 helicopter test. Note that a large amount of the data occurs after the impact time.

Survivability studies from anthropomorphic data of a Human Surrogate Torso Model (HSTM), along with three other passenger crash dummies, were part of the main test objectives for the MD-500 helicopter test. The first crash landing test included the vehicle with DEAs on it because the expectancy of survivability with the vehicle and its occupants were much greater than without the DEAs. Data results from the second crash landing test, without DEAs, proved this theory correct. Deflection data from multi-axial strain gages, four crash dummies, and photogrammetric measurement results indicated the airframe structural components and its occupants, after the flight with DEAs, survived with relatively little or no damage. Only minor repairs were required for the airframe after the first drop. After the following, second crash test, significant damage was reported to the airframe and to the well being of the instrumented crash dummies inside.

Fig. 7.30. MD-500 helicopter airframe being prepared for crash test with 4 crash dummies inside and 2 deployable energy absorbers beneath.

Fig. 7.31. MD-500 helicopter tail major strain at impact.

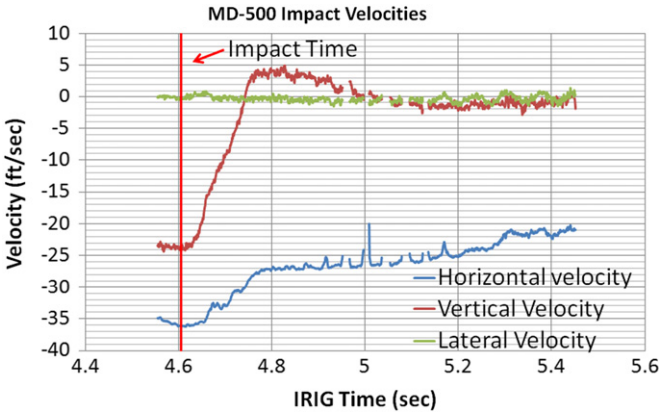

Fig. 7.32. Impact velocities of MD-500 helicopter.

8. Quantitative flow diagnostics

Photogrammetry provides the relationship between the image plane and the object space, which is an essential part in all quantitative image-based flow diagnostic and visualization techniques. In particular, flow visualizations on a surface (either a solid surface or a virtual plane like a laser sheet) require mapping of data extracted from images onto the surface in the object space. These techniques include pressure and temperature sensitive paints, oil-film skin friction measurements, projection Moiré interferometry, Doppler global velocimetry, particle image velocimetry, and planar laser induced fluorescence.

8.1. Relationship between image plane and surface

8.1.1. Point correspondence

As pointed out in Appendix B, to establish the point correspondence between images, at least four cameras (or four images) are needed. However, when an object-space point is constrained on a surface, the point correspondence is one-to-one for calibrated/oriented cameras. A surface in the 3D object space that has the one-to-one correspondence to the image plane, as illustrated in Fig. 8.1, could be a solid surface or a virtual surface like laser sheet. Consider a surface in the object space $X^3=F(X^1,X^2)$ that is, imposed as a surface constraint in the perspective projection transformation. Therefore, Eq. (B3) in Appendix B becomes

$$\begin{aligned} w_{11}X^1+w_{12}X^2+w_{13}F(X^1,X^2)&=\boldsymbol{W_1}\bullet\boldsymbol{X}_c \\ w_{21}X^1+w_{22}X^2+w_{23}F(X^1,X^2)&=\boldsymbol{W_2}\bullet\boldsymbol{X}_c, \end{aligned} \tag{8.1}$$

where w_{ij} ($i=1,2$ and $j=1,2,3$) are the elements of the vectors $\boldsymbol{W}_1=(w_{11}, w_{12}, w_{13})^T$ and $\boldsymbol{W}_2=(w_{21}, w_{22}, w_{23})^T$. For the given surface $X^3=F(X^1,X^2)$, the coordinates $(X^1, X^2)^T$ can be obtained from the image coordinates $\boldsymbol{x}=(x^1, x^2)^T$ by solving Eq. (8.1). Thus, the coordinates $\boldsymbol{X}=(X^1, X^2, X^3)^T$ on a surface in the object space can be symbolically expressed as a function of the image coordinates $x=(x^1, x^2)^T$ by $\boldsymbol{X}=\boldsymbol{f_S}(\boldsymbol{x})$. In fact, this is a parametric representation of the surface using the image coordinates $x=(x^1, x^2)^T$ as the parameters. Generally, the function $\boldsymbol{f_S}(\boldsymbol{x})$ cannot

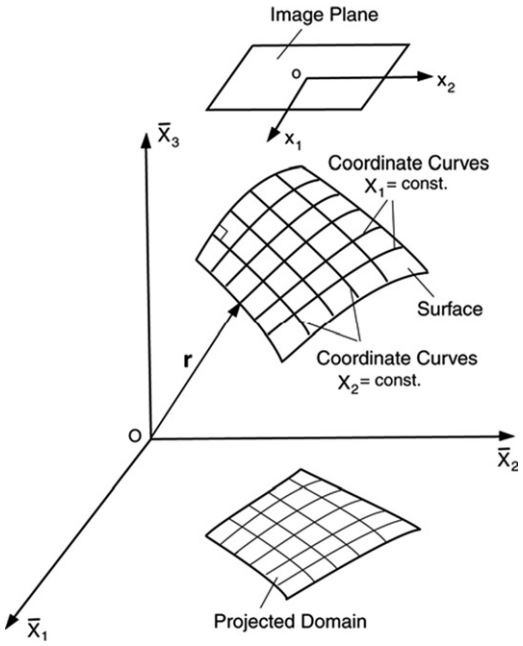

Fig. 8.1. One-to-one correspondence between the image plane and a surface in the object space.

be written as a closed-form solution except for some simple surfaces such as a plane and a cylindrical surface.

8.1.2. Velocity correspondence

Differentiating Eq. (B3) in Appendix B leads to $d\boldsymbol{W}_{1(n)}\bullet X+\boldsymbol{W}_{1(n)}\bullet dX=d\boldsymbol{W}_{1(n)}\bullet X_{c(n)}$ and $d\boldsymbol{W}_{2(n)}\bullet X+\boldsymbol{W}_{2(n)}\bullet dX=d\boldsymbol{W}_{2(n)}\bullet X_{c(n)}$, where the subscript index (n) denotes the nth camera, and $\boldsymbol{W}_1=(x^1-x_p^1+\delta x^1)\boldsymbol{m}_3+c\boldsymbol{m}_1$ and $\boldsymbol{W}_2=(x^2-x_p^2+\delta x^2)\boldsymbol{m}_3+c\boldsymbol{m}_2$ are the vectors discussed in Appendix B. For the fixed lens distortion terms, since $d\boldsymbol{W}_{1(\boldsymbol{n})}=dx^1_{(\boldsymbol{n})}\boldsymbol{m}_{3(\boldsymbol{n})}$ and $d\boldsymbol{W}_{2(\boldsymbol{n})}=dx^2_{(\boldsymbol{n})}\boldsymbol{m}_{3(\boldsymbol{n})}$, we have

$$\boldsymbol{W}_{1(\boldsymbol{n})}\bullet\boldsymbol{U}=\boldsymbol{m}_{3(\boldsymbol{n})}\bullet[\boldsymbol{X}-\boldsymbol{X}_{\boldsymbol{c}(\boldsymbol{n})}]u^1_{(n)},$$
$$\boldsymbol{W}_{2(\boldsymbol{n})}\bullet\boldsymbol{U}=\boldsymbol{m}_{3(\boldsymbol{n})}\bullet[\boldsymbol{X}-\boldsymbol{X}_{\boldsymbol{c}(\boldsymbol{n})}]u^2_{(n)}, \tag{8.2}$$

where $d\boldsymbol{X}/dt=\boldsymbol{U}(\boldsymbol{X})=(U_1,U_2,U_3)^T$ is the velocity field in the 3D object space and $\boldsymbol{u}_{(\boldsymbol{n})}=d\boldsymbol{x}_{(n)}/dt=d/dt[x^1_{(n)},x^2_{(n)}]^T$ is the optical flow that is defined as the velocity field in the image plane that transforms one image into the next image in a time sequence. The physical meaning and the mathematical definition of the optical flow in various flow visualizations have been discussed by Liu and Shen [73]. For particle images, the optical flow can be determined by correlation-based methods [89,2] and particle tracking method [39,76]. For continuous passive scalar images and other flow visualization images, the optical flow can be determined by solving the physics-based optical flow equation [73].

If the correspondence between the image coordinates $\boldsymbol{x}_{(n)}=[x^1_{(n)},x^2_{(n)}]^T$ in at least two cameras ($n\geq 2$) is known, the corresponding object-space point $\boldsymbol{X}$ of a particle can be determined by photogrammetric intersection. In general, as pointed out in Section 3.5, at least four cameras are needed for determining the point correspondence based on the Longuet-Higgins equations. If the optical flow $\boldsymbol{u}_{(\boldsymbol{n})}$ in the nth image is determined by tracking individual particles, the right-hand-side terms of Eq. (8.2) can be known for calibrated/oriented cameras. Thus, the 3D velocity field $\boldsymbol{U}(\boldsymbol{X})$ can be determined by solving Eq. (8.2) using a least-square method. This corresponds to 3D particle tracking velocimetry [39]. In another case, if particles in flow are illuminated by a suitably thick laser sheet, there is the one-to-one point correspondence between particle images and the laser sheet plane in a certain average sense since the laser sheet has a finite thickness. Therefore, once the optical flow $\boldsymbol{u}_{(\boldsymbol{n})}$ is obtained by a correlation-based method in particles images taken by at least two cameras with different viewing angles, the velocity $\boldsymbol{U}(\boldsymbol{X})$ on the laser sheet plane can be determined, which corresponds to stereoscopic PIV [3,88]. For volumetric flow visualizations in tomographic velocimetry, Eq. (8.2) cannot be directly used since the optical flow $\boldsymbol{u}_{(\boldsymbol{n})}$ is interpreted as the path-averaged velocity that is not exclusively associated with an object-space point X in this case [73].

8.2. Pressure and temperature sensitive paints

Pressure- and temperature-sensitive paints (PSP and TSP) are global techniques for surface pressure and temperature measurements [65,70,10]. After the results of pressure and temperature are extracted from images of PSP and TSP, it is necessary to map the data in the image plane onto a surface grid in the 3D object space to make the results more useful for aeronautical engineers and researchers. The collinearity equations in photogrammetry provide the perspective relationship between the 3D coordinates in the object space and corresponding 2D coordinates in the image plane. The known object space coordinates $\boldsymbol{X}=(X,Y,Z)$ $[\boldsymbol{X}=(X^1,X^2,X^3)^T]$ on a given model surface are mapped into the image coordinates (x,y) using Eq. (8.1), and then PSP and TSP data at the image points are associated with those at the corresponding points on the surface. Fig. 8.2 shows a pressure distribution mapped onto an aircraft model surface from PSP images in a transonic flow [40]. Further, this mapping is necessary for calculating aerodynamic loads and surface heat transfer and for comparison with CFD results.

From the standpoint of photogrammetry, a key of this procedure is geometric camera calibration/orientation by solving the collinearity equations to determine the camera interior and exterior orientation parameters, and lens distortion parameters. Simpler resection methods have been used in PSP and TSP systems to determine the camera exterior orientation parameters when the interior orientation and lens distortion parameters are set [37,63,92]. The DLT was also used [8]. The optimization method for comprehensive camera calibration was developed by

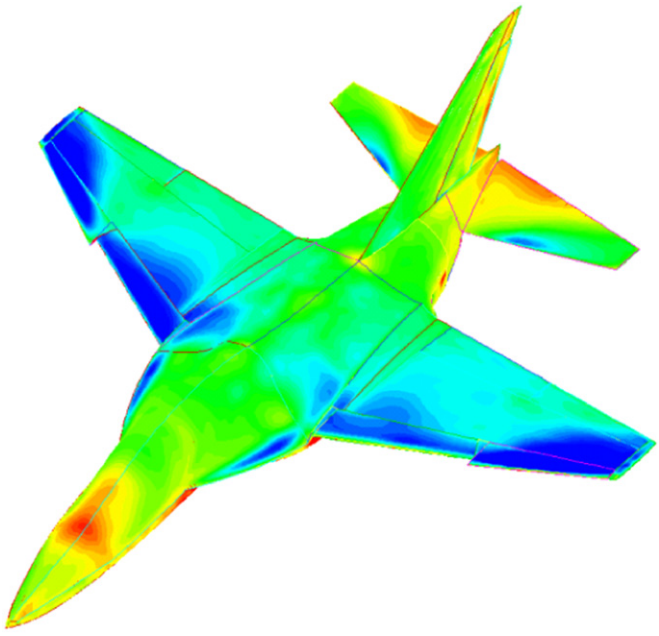

Fig. 8.2. Typical pressure distribution mapped onto a surface grid of the model. From Engler et al. [40].

Liu et al. [67], which can determine the exterior orientation, interior orientation and lens distortion parameters (as well as the pixel aspect ratio of a CCD array) from a single image of a 3D target field. As pointed out before, the optimization method, combined with the DLT, allows automatic camera calibration without an initial guess of the orientation parameters; this feature particularly facilitates PSP and TSP measurements in wind tunnels. Besides the DLT, a closed-form resection solution given by Zeng and Wang [111] is also useful for initial estimation of the exterior orientation parameters of a camera based on three known targets.

Cattafesta et al. [31] and Cattafesta and Moore [32] presented a photogrammetric application to boundary layer transition detection on a three-dimensional model. A TSP system has been developed for the purpose of transition detection and applied to several three-dimensional models over a wide speed range. TSP detects transition by visualizing the temperature change caused by different heat transfer rates in laminar and turbulent flow regimes in a transient thermal process. A key element of the system development has been photogrammetric tools for mapping temperature (or heat transfer rate) to a three-dimensional grid of the model surface. Fig. 8.3 illustrates reconstruction of a transition image of a swept-wing model in Mach 3.5 flow mapped onto the half of the model surface grid by using photogrammetry. The bright region corresponds to the turbulent boundary layer where the heat transfer rate is higher than that in the laminar boundary layer. The onset of transition is demarcated in the image as a bright parabolic band on the wing where the cross-flow instability mechanism dominates the transition process. However, no transition is observed near the centerline of the model. This is because near the symmetric plane of

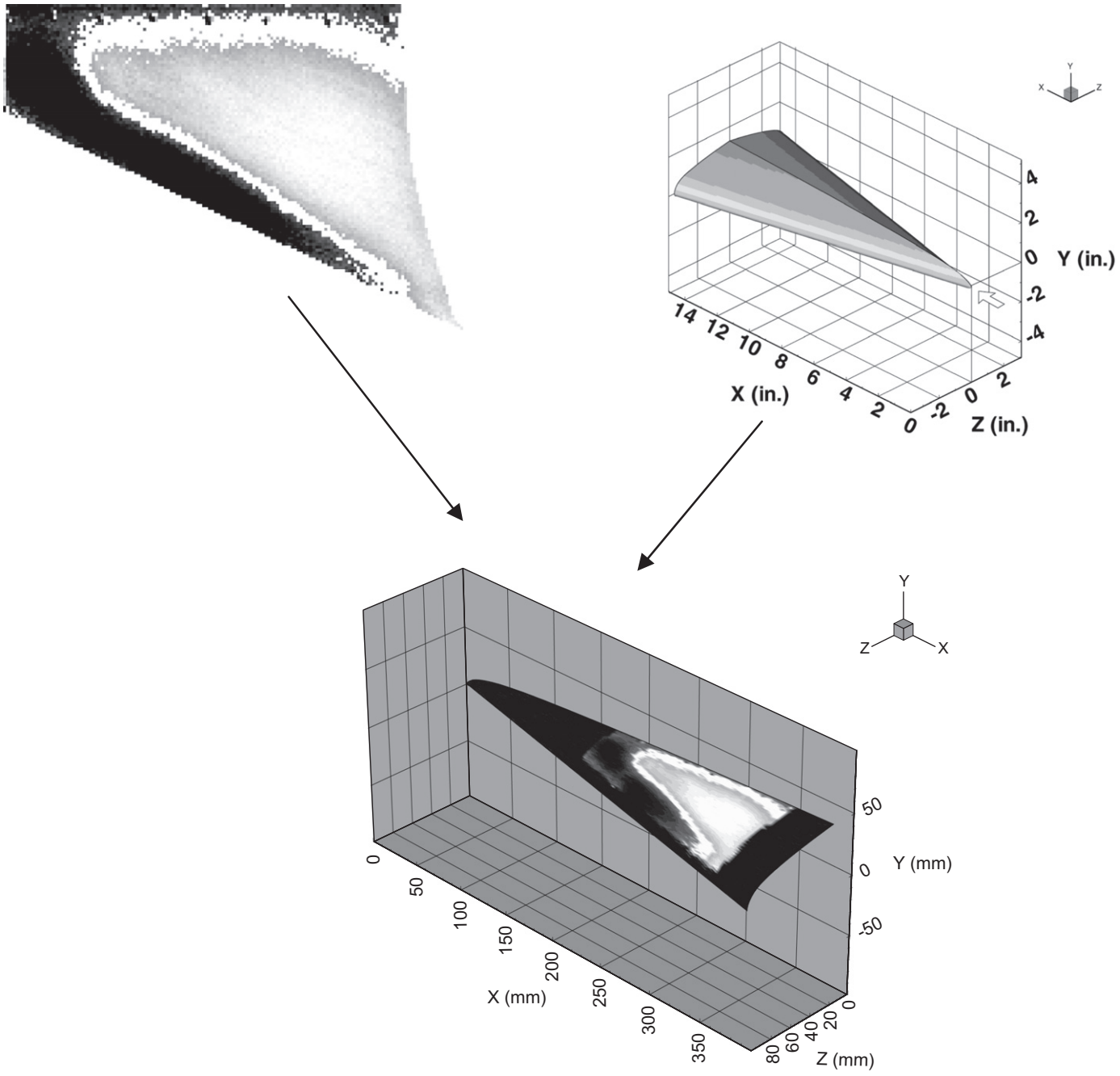

Fig. 8.3. Heat transfer distribution visualizing transition mapped onto a half of a CFD grid of a swept-wing model at Mach 3.5. From Cattafesta et al. (1996).

the model the stability is dominated by the Tollmien–Schlichting instability mechanism that is weaker than the cross-flow instability mechanism.

8.3. Oil-film interferometry

Image-based oil-film interferometry provides measurements of wall shear stress or skin friction that can be obtained relatively quickly and with good accuracy in wind tunnels [82]. Oil-film interferometry measures the thinning rate of a thin oil film applied to a test surface to determine the skin friction on the surface. Fig. 8.4 shows how the interference process occurs in a thin film. Light striking the oil surface is partially transmitted and partially reflected from the oil/air interface. The transmitted light passes through the oil and strikes the oil/surface interface, where it is partially reflected and partially absorbed. The reflected light passes back through the oil and exits the oil film with a phase difference from the light that was reflected from the air/oil interface. When the two beams pass though a lens to create an image, they constructively or destructively interfere depending on their phase difference as shown in Fig. 8.4. The interference between many such beams produces a fringe pattern. As the oil film thins, the interference pattern will shift, and the spacing between the fringes will grow as shown by the interference pattern in Fig. 8.4(a). The height of the oil is related to the fringe pattern through the phase difference ϕ

$$h = \frac{\lambda\phi}{4\pi}\frac{1}{\sqrt{n_f^2 - n_a^2\sin^2\theta_i}}, \tag{8.3}$$

where λ is the wavelength of the illuminating light, n_f and n_a are the indices of refraction of the oil and air, respectively, and θ_i is the local incidence angle of the light. Knowing the oil height, the wall shear stress can be determined using one of the several analysis methods [82], which are all based on some form of (or simplified form of) Eq. (8.3).

Accompanying the increased use of oil-film interferometry has been a demand for higher accuracy and less time-intensive analysis.

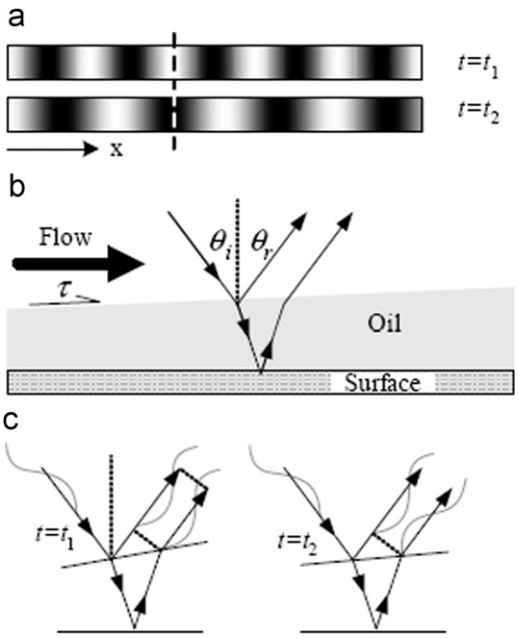

Fig. 8.4. Schematic depicting amplitude-splitting or Fizeau interferometry in oil-film interferometry: (a) fringe patterns at two different times, (b) the interference process, and (c) constructive and destructive interference. The dashed line in (a) corresponds to the location where the interference in (c) is given.

One way that these two issues can be addressed is through the use of photogrammetry [82]. Perhaps most obvious is the need for one-to-one mapping of the image plane to the model surface in the object space. To analyze the interferograms for skin friction, the height distribution versus a spatial coordinate is needed as indicated by Eq. (8.3). Less obvious, and what makes the need for photogrammetry for oil-film interferometry unique, is the need to know the light incidence angle θ_i in Eq. (8.3). As evident in Fig. 8.5 for the NASA Hump model, surface curvature plays a large role in determining the incidence angle. However, when cameras are used in close proximity to the model surface in most implementations of oil-film interferometry in wind tunnels, the camera's perspective can also play a large role. When the camera is in close proximity to the model surface, even flat surfaces will have significant changes in incidence angle across the region imaged. Photogrammetry can be effectively used to address both model curvature and camera perspective issues. A final justification for photogrammetry is that it automatically handles the geometrical issues in imaging, which saves time and simplifies the requirements for measuring the geometric placements of the optical components of the oil-film interferometry system.

To demonstrate the importance of photogrammetry in the interferogram analysis process, an experiment was performed at NASA Langley on a hump mounted on a splitter plate, providing significant challenges due to model curvature and camera proximity. Fig. 8.5 shows the complex geometry for this test case. Due to limited optical access, the camera and light source had to be inserted into the wind tunnel after each test. This resulted in an extremely close proximity of the camera to the model surface. The combined effects of camera proximity and model curvature make photogrammetry critical to calculating accurate skin friction values. One case is an interferogram taken on the splitter plate downstream of the hump where the boundary layer is recovering from separation. The surface here is flat, so all of the angle variations are due to a close proximity. Fig. 8.6(a) shows the original interferogram with an overlaid grid with 6.35 mm spacing. The convergence of the almost vertical lines toward the top of the figure is quite evident, although all the lines appear straight as they should on a planar surface. The corresponding variation in the incidence angle is shown in Fig. 8.6(b) where angles from 22° to 30° are observed in the region containing fringes. The measured camera angle (relative to the splitter plate) was 23°. The skin friction distribution from this interferogram has been determined using the measured camera angle and the distribution calculated from photogrammetry. The two distributions are shown in Fig. 8.7 where it is evident that the difference between the two calculated results decreases as x/c increases. The point where the error drops toward zero corresponds to the lower

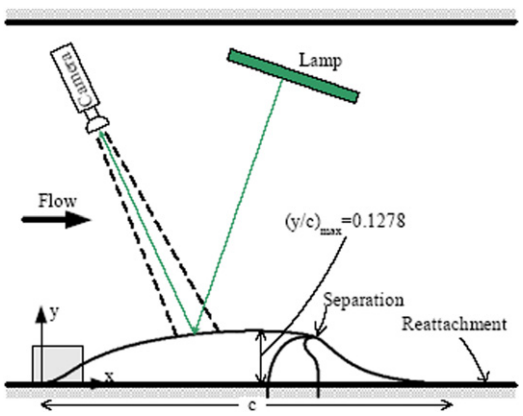

Fig. 8.5. Schematic of the NASA Hump model and oil-film interferometry setup.

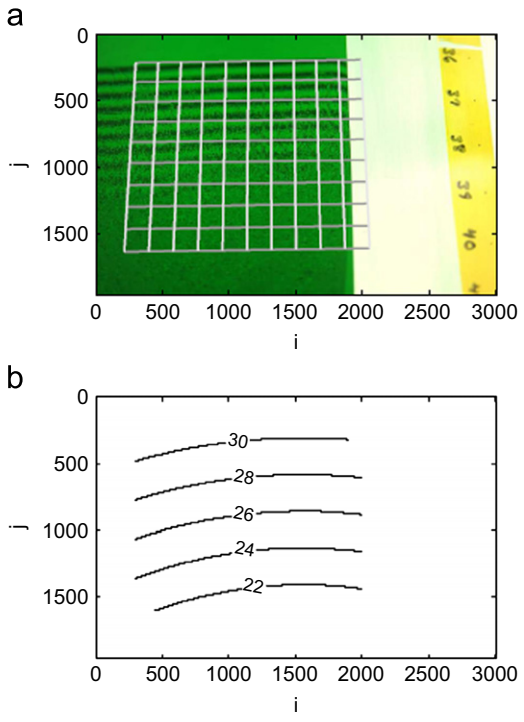

Fig. 8.6. Photogrammetry results for a location on the splitter plate downstream of the hump: (a) original interferogram with grid overlain, and (b) incidence angle.

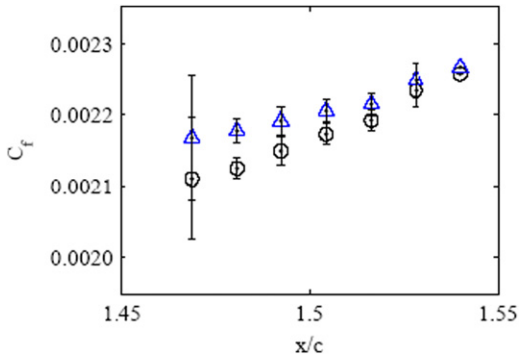

Fig. 8.7. Averaged skin friction values from a location downstream of reattachment where the model surface is flat: triangle - θ_i set to measured camera angle; and circle - θ_i determined from photogrammetry results.

portion of the grid in Fig. 8.6(a) where photogrammetry estimates the angle to be approaching 23° as shown in Fig. 8.6(b). At the lowest x/c point in Fig. 8.7, the difference in the calculated skin friction values is just under 3%. Although this may not sound like a lot, it is only one contribution to the uncertainty and alone may be unacceptable when high accuracy measurements are required.

9. Vision-vased autonomous landing of aircraft

9.1. Two-camera method

Autonomous landing requires the accurate determination of the aircraft position and attitude relative to the ground coordinate system. A vision-based system has been developed to determine the aircraft position and attitude based on visible features like runway edges on the ground [71,105]. The vision-based system is applicable to small general aviation aircraft as well as unmanned-air-vehicles (UAVs) and micro-air-vehicles (MAVs). The vision system contains two (or multiple) CCD cameras located at suitable positions on an aircraft (such as wing tips). Fig. 9.1 shows the NASA LaRC OV-10 experimental aircraft with two cameras at the wing tips and one camera at the top of the left vertical tail. With effective image processing and videogrammetric algorithms, the vision system is able to track natural patterns and artificial targets on a standard runway and determine in real time the aircraft position, attitude and velocity relative to a fixed ground coordinate system. The distinct patterns and targets on the ground should be identified in images in order to determine the position of an aircraft using videogrammetric methods. A distinct pattern of a runway is its edges that are identified as high-contrast lines between the runway and its surrounding ground (see Fig. 9.2). The high-contrast lines on images could be interpreted in a sense of either the gray level or statistical characteristics of patterns. After the points (or targets) are correctly identified and their coordinates are accurately measured in images, the position and attitude of a landing aircraft in the fixed ground coordinate system can be determined in real time using two calibrated/oriented cameras in a vision system. The velocity can be also determined from a time sequence of position data.

In order to determine the camera exterior and interior orientation parameters, field camera calibration/orientation should be done for flight tests, requiring a large target field with the known coordinates in an appropriate aircraft body system. As shown in Fig. 9.3, the aircraft calibration target field is set on the east side of

Fig. 9.1. The NASA LaRC OV-10 experimental aircraft with two cameras at the wing tips and one camera at the top of the left vertical tail.

Fig. 9.2. Runway with high-contrast edges.

the NASA Langley Hanger Building. Eight targets (2 ft diameter) are placed on the east wall of the hanger annex. The targets are fabricated from 1/8-in thick aluminum sheet, painted white with a black circle. Also, eight smaller targets (one foot diameter) are placed on the ground; several of these are located on the grass regions next to the east wall of the hanger annex. A team from the NASA Langley GIS group takes careful measurements of the relative locations of the centriods of each target with respect to the aircraft nose wheel marking on the tarmac. The horizontal reference plane will be aligned perpendicular to the gravity vector. Thus, the target field for camera calibration/orientation is established. Pre-flight and post-flight tests should be carried out to examine the repeatability of camera calibration and orientation.

In Appendix D, a method based on two cameras mounted on an aircraft is described. As shown in Fig. 9.4, there are three relevant coordinate systems: the ground, aircraft and image coordinate systems. In the right-handed aircraft coordinate system (X_{ac}, Y_{ac}, Z_{ac}), the X_{ac} axis directs from the head to the tail along the fuselage, the Y_{ac} axis directs along the right wing and the Z_{ac} axis points upward. The ground coordinate system (X_g, Y_g, Z_g) is located at the end of a runway. The position and orientation of the image coordinate system is fixed relative to the aircraft coordinate system when an aircraft is rigid. The relationship between the image and aircraft coordinate system is determined by camera calibration/orientation on the ground. By contrast, the position and orientation of the aircraft coordinate system are time-dependent relative to the ground coordinate system during landing.

Fig. 9.3. Target field for camera calibration/orientation.

The main objective is to recover the position and attitude of an aircraft relative to the ground coordinate system. As shown in Fig. 9.4(a), two points P_1 and P_2 on the right edge of a runway and third point P_3 on the left edge (viewed from the aircraft) are selected. The coordinates of the points P_1, P_2 and P_3 in the aircraft coordinate system (X_{ac}, Y_{ac}, Z_{ac}) are determined by photogrammetric intersection in a calibrated two-camera vision system mounted on an aircraft. Thus, the triangle $P_1P_2P_3$ defines three unit orthogonal vectors on the ground expressed in the aircraft coordinate system. The vectors $\boldsymbol{e_{ig}}$ ($i=1,2,3$) constitute a local coordinate system on the ground. It is assumed that this local system is just a translated ground coordinate system (X_g, Y_g, Z_g). The relation between $\boldsymbol{e_{ig}}$ ($i=1,2,3$) in the ground coordinate system and $\boldsymbol{e_{iac}}$ (i=1,2,3) in the aircraft coordinate system determines the Euler angles ϕ, θ, and ψ that are the roll, pitch and yaw angles of an aircraft relative to the ground coordinate system (see Appendix D). Further when the runway is flat and the runway width is given, the aircraft latitude and the lateral position of the aircraft relative to the runway centerline can be determined. In general, the two-camera (or multiple-camera) approach gives the position and attitude of a landing flight vehicle (aircraft or spacecraft) in the ground coordinate system defined by three selected points.

To estimate the effects of random noise in images on the position and attitude calculation, sensitivity simulation is conducted for typical cases of landing on a 4100-ft long and 70-ft wide runway. The attitude of an aircraft is given by the Euler angles $\phi=-2^\circ$, $\theta=5^\circ$, and $\psi=3^\circ$. Three aircraft positions during landing are considered, and for example, in Case 2, $(X_{gO_{ac}}, Y_{gO_{ac}}, Z_{gO_{ac}}) = (4477, 40, 118)$ ft. When the wingspan is 32 ft, the camera orientation parameters for the camera on the left wing are $(\omega,\phi,\kappa,X_c,Y_c,Z_c)=(85^\circ,-88^\circ,0^\circ,0,0,16$ ft) and $c, x_p, y_p, K_1, K_2, P_1, P_2$, $S_h/S_v = 12$ mm, 0, 0, 0, 0, 0, 0, 12/13). For the camera on the right wing, the camera orientation parameters are $(\omega,\phi,\kappa,X_c,Y_c,Z_c)=(85^\circ,-88^\circ,0^\circ,0,0,-16$ ft) and (c, x_p, y_p, K_1, K_2, P_1, P_2, $S_h/S_v = (12$ mm, 0, 0, 0, 0, 0, 0, 0, 12/13). The camera

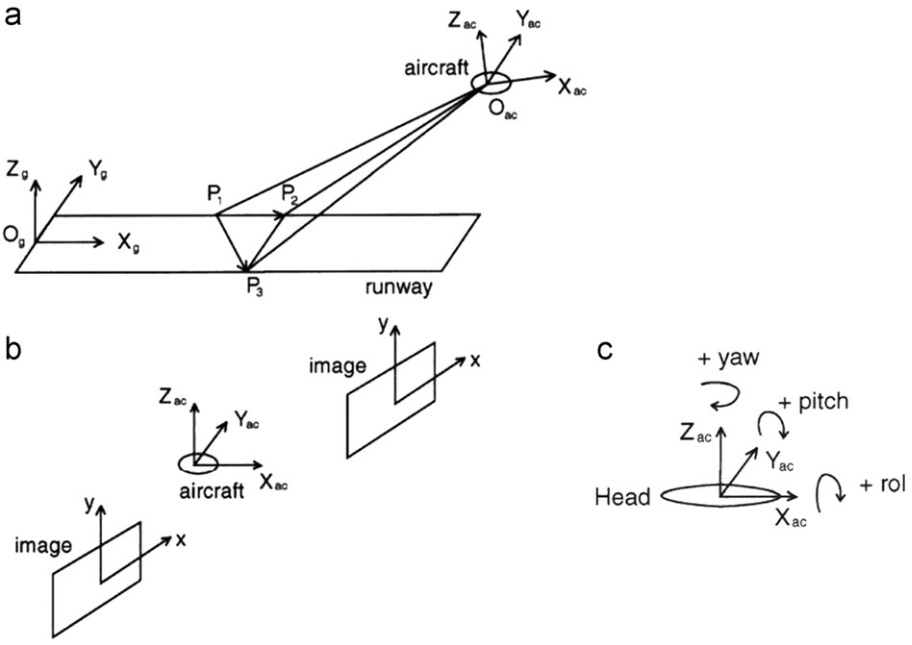

Fig. 9.4. (a) The ground and aircraft coordinate systems, (b) the aircraft and image coordinate systems, (c) the attitude of an aircraft.

format is 640×480 pixel and the horizontal and vertical pixel spacings are 0.012 and 0.013 mm/pixel. Three selected points P_1, P_2 and P_3 on the edges for position and attitude determination are $(X_g,Y_g,Z_g)=(1990,35,0)$, $(3490,35,0)$ and $(2990,-35,0)$ ft, respectively.

The effect of random noise in images on the accuracy of determining the position and attitude of an aircraft is examined. The random noise has a Gaussian distribution with a standard deviation σ. Fig. 9.5 shows the simulated negative images of the edges of the runway taken from cameras on the left and right wings for Case 2, where the Gaussian random noise with $\sigma=1$ pixel is added to the edge images. The runway edges are fit using a linear function. The average horizontal scale of the runway in images is about 23.9 pixel. The points P_1, P_2 and P_3 are selected in the image from the right-wing camera and the corresponding points in the image from the left-wing camera are determined by intersecting the epipolar lines with the runway edges. The errors in estimation of the position and attitude due to the random noise are shown in Fig. 9.6 for Case 2, where the normalized random noise is the noise level σ normalized by the average horizontal scale of the runway. The aircraft position in the X_g coordinate (along the runway) is particularly sensitive to the noise; the error could be about 40 ft when the noise is 1 pixel. The large errors are due to a small viewing angle of the cameras relative to the ground. The errors in the latitude and lateral position are less than one foot when the noise is 1 pixel. The attitude estimation is less sensitive to the random noise. When the noise is 1 pixel, the error in the roll angle is about 2° and the errors in the pitch and yaw angles are less than 0.2°. Similar results are obtained for c other two position cases. Except the X_g position of the aircraft, the absolute accuracy of estimation of the position and attitude of the aircraft in the presence of the random noise is improved when the aircraft is approaching the runway. This is because the runway looks larger in images and the relative noise is smaller. However, the error in the X_g position of the aircraft does not change much in these three cases.

9.2. Single-camera method

A single-camera method was suggested by Sasa et al. [98] to determine the aircraft position and attitude based on the runway edges and horizon. In Appendix D, the problem is reformulated. The effects of random noise in images on the position and attitude calculation using the single-camera method for the three cases are examined. Fig. 9.7 shows a simulated image of the runway

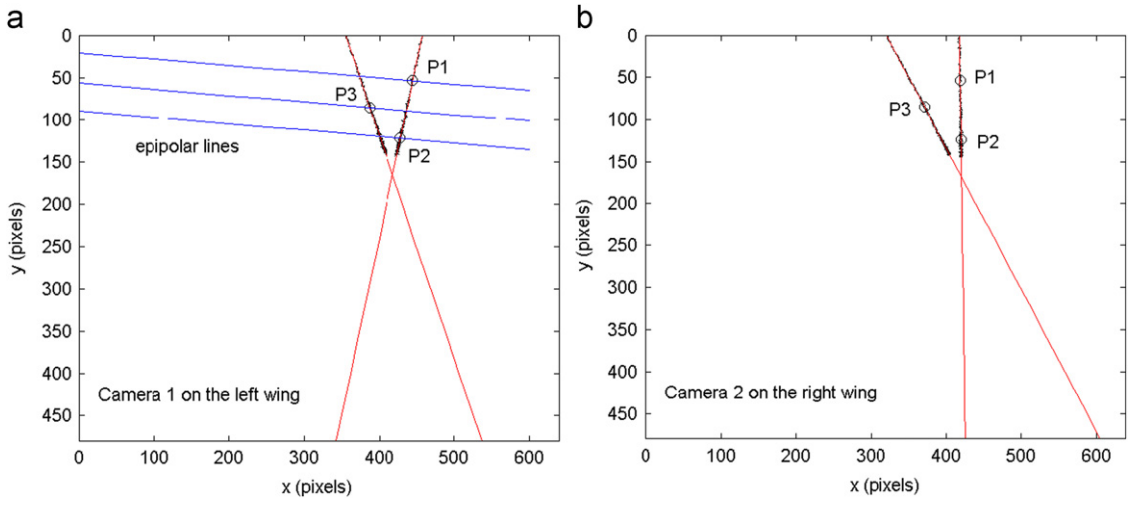

Fig. 9.5. Simulated images in Case 2: $(X_{gO_{ac}},Y_{gO_{ac}},Z_{gO_{ac}})=(4477,40,118)$ ft.

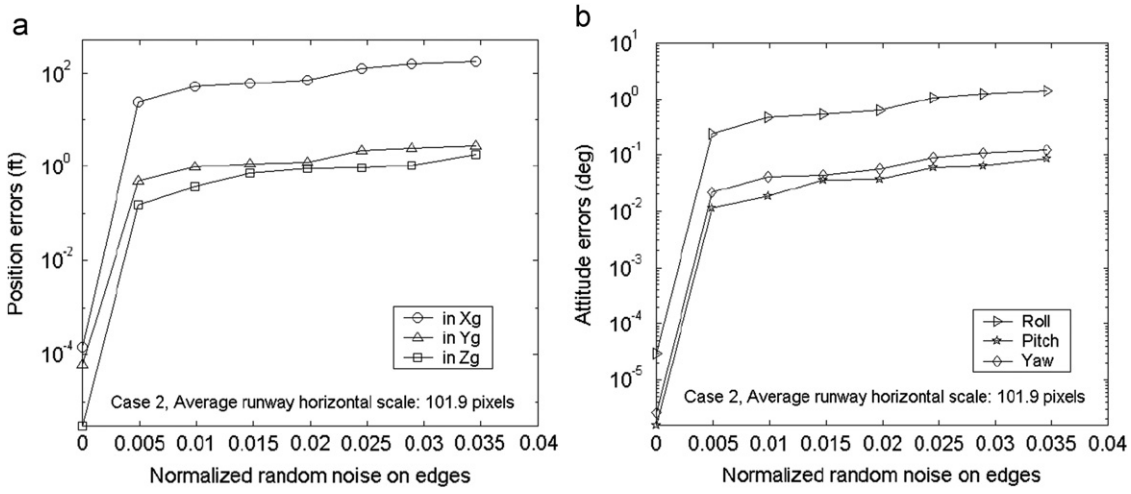

Fig. 9.6. Errors in position and attitude estimations due to random noise in images for Case 2 (the two-camera approach).

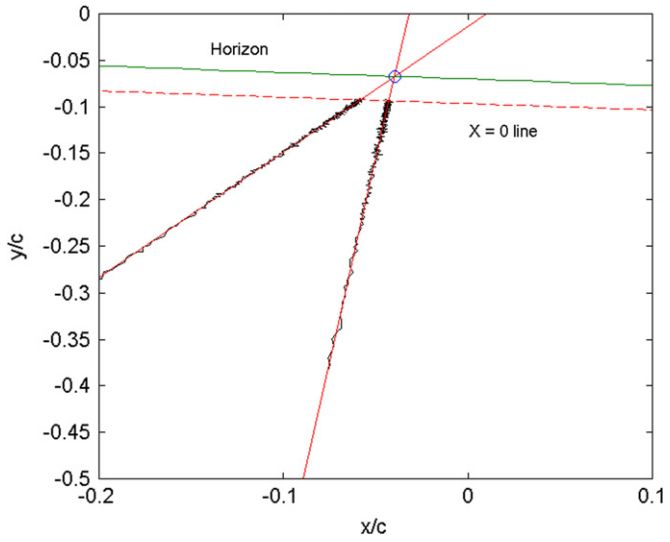

Fig. 9.7. Runway edges, horizon and horizontal line in the image plane.

edges, horizon and horizontal line $X_g=0$. The errors in estimation of the aircraft position and attitude due to the random noise are shown in Fig. 9.8 for Case 2, where the normalized random noise in the image plane is the noise level normalized by the principal distance c. Here, the noise is not added to the horizon such that the roll angle is independent of the noise. The errors in estimation of the position and attitude due to the random noise are also calculated for Cases 1 and 3. Given the noise level in the image plane, the errors in estimation of the position and attitude are reduced when the aircraft approaches to the runway.

The estimation of the roll angle mainly depends on the horizon. When the horizon cannot be identified, an artificial horizontal line (an array of targets located at a sufficiently far location) can be used to estimate the roll angle. The accuracy in estimation of the roll angle is related to the relative aircraft height to the horizontal line that is characterized by $|Z_{gO_{ac}}/X_{gO_{ac}}|$. Note that when $X_{gO_{ac}}\to-\infty$, the horizontal line approaches to the horizon. Fig. 9.9 shows the effects of $|Z_{gO_{ac}}/X_{gO_{ac}}|$ on estimation of the aircraft position and attitude. The error in the roll angle linearly depends on $|Z_{gO_{ac}}/X_{gO_{ac}}|$; the pitch and yaw angles are almost independent of $|Z_{gO_{ac}}/X_{gO_{ac}}|$.

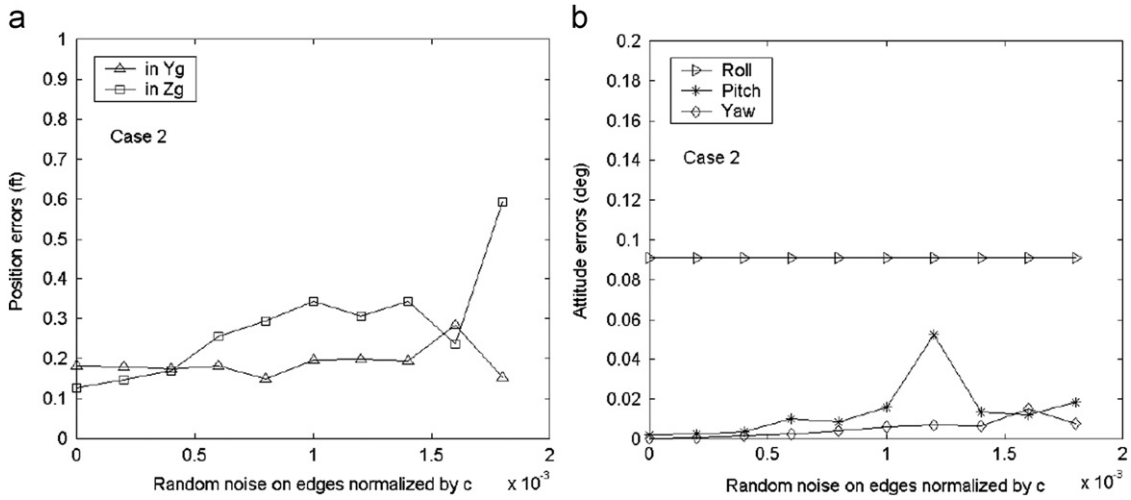

Fig. 9.8. Errors in position and attitude estimations due to random noise in images for Case 2 (the single-camera approach).

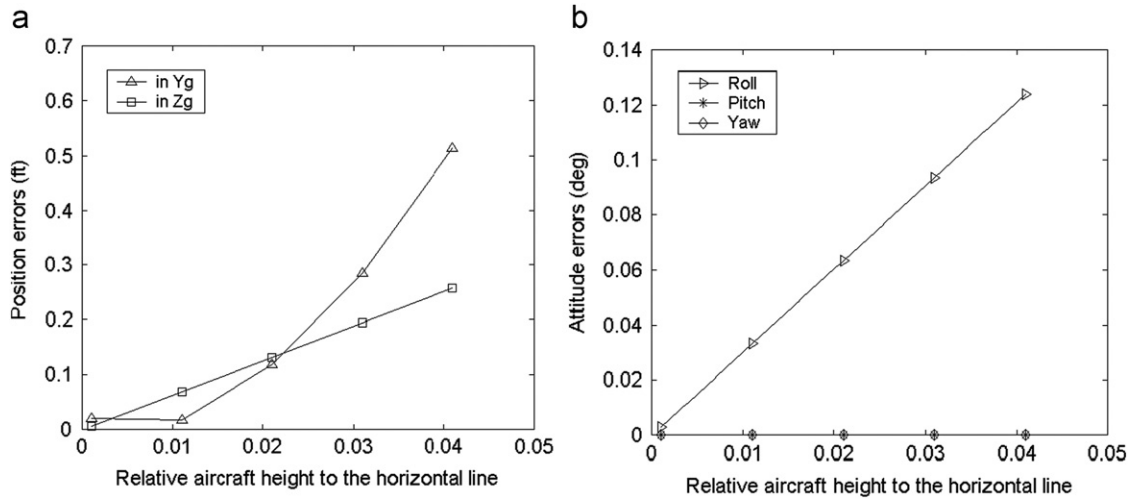

Fig. 9.9. Sensitivity of position and attitude estimations to the relative aircraft location to the horizontal line.

10. Measurements for gossamer space structures

The term "gossamer" is generally applied to ultra-low-mass space structures. Frequently these structures are designed to be tightly packaged for launch, and then to deploy or inflate once in space. These properties will allow for in-space construction of very large structures 10 to 1000 m in size such as solar sails, inflatable antennae, and space solar power stations using a single launch. Most gossamer space structures rely on ultra-thin membranes and inflatable tubes to achieve a reduction, compared to standard space hardware, in launch mass by a factor of 10 and in launch volume by a factor of 50. The technology has been adapted for possible use in a wide variety of applications, including deployable ballutes for aerobraking on Mars, telescope sunshields, and membrane space solar arrays [55,33,78,108]. Gossamer structure research has reached the stage where measurements of the surface profile and dynamic behavior has become an integral part of the design process. Furthermore, measurements of both ground test and in-flight structures are essential for continued gossamer development.

The primary reason to perform surface profiling measurements on gossamer structures is to validate computational models. Once these models are validated they become reliable design tools for future spacecraft systems. To obtain high fidelity data that will be useful for validating computational models, the measurement techniques used to quantify the behavior of gossamer structures must ideally be non-invasive, and consequently the metrology requirements for gossamer structures require special design considerations. Non-contact instrumentation is preferred because gossamer structures are (1) delicate, thin and ultra-low mass, and (2) typically transparent or specularly reflective. There are several non-invasive or minimally invasive techniques and instruments available to quantify the shape and/or dynamic behavior of gossamer structures, including projection moiré interferometry, light detection and ranging systems, capacitive type displacement sensors, laser vibrometry, and photogrammetry. Photogrammetry (or videogrammetry) is a relatively simple and inexpensive technique. Particularly, combined with dot projection techniques, it can provide completely non-contact surface measurements suitable for near real-time applications. Based on the projection of a dense dot pattern (targets), images from two or more video cameras are collected and processed to yield the three-dimensional shape of the object based on the spatial coordinates of the projected dots.

10.1. Static measurements of 2-m Kapton solar sail

The applications discussed in this section were conducted for dual purposes: to develop measurement methods suitable for use on actual solar sail spacecraft and to obtain measurements for validation of structural analytical models. The experiments used low-fidelity, generic solar sail test articles at NASA Langley Research Center. These low-fidelity test articles are sub-scale models manufactured from solar sail quality materials but are not directly scalable to full size solar sails. The developed methods could be applied to other current and future high-fidelity gossamer test structures and space missions.

10.1.1. Low density field

This experiment was designed to assess the feasibility of using projected circular targets instead of attached retro-reflective targets on highly reflective membrane surfaces. The 2 m per side, square, aluminized Kapton solar sail test article shown in Fig. 10.1(a) was selected for static shape measurement because of its continuity (other test articles are divided into four quadrants). A pattern of approximately 400 dots was projected onto the membrane and imaged by four consumer digital cameras. The cameras were positioned at approximately 90° separation at the corners of the sail and simultaneously photographed it to avoid possible membrane movement between images, as shown in Fig. 10.1(b). Fig. 10.2 shows an actual image used in the photogrammetric processing, with the dot pattern clearly visible on the

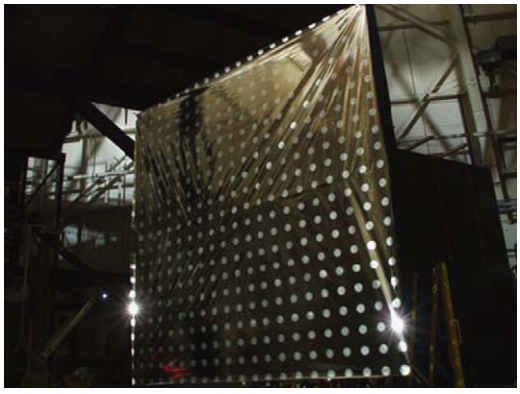

Fig. 10.2. Image used in photogrammetric processing.

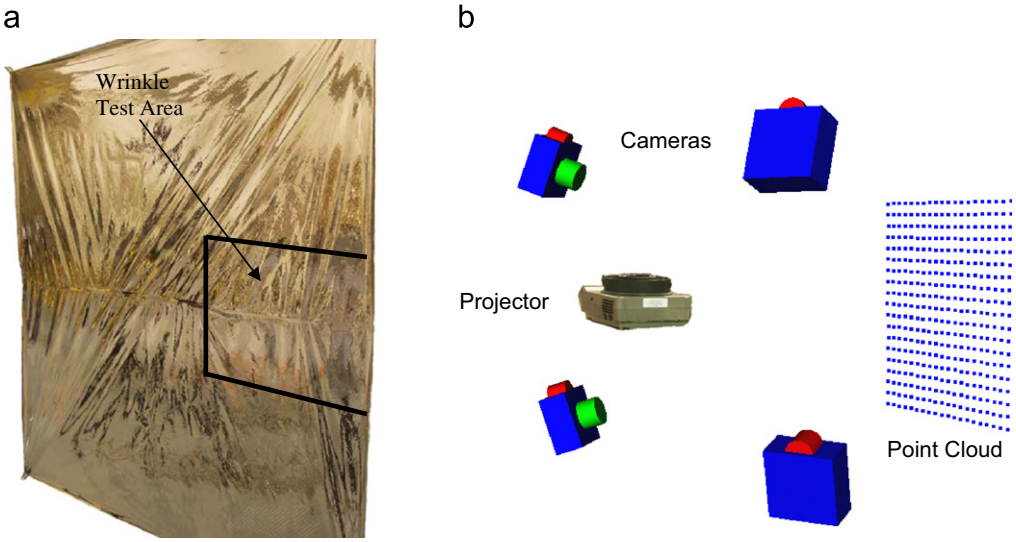

Fig. 10.1. (a) Two-meter Kapton single quadrant solar sail, (b) full field test setup.

surface of the sail. The image is underexposed to create high-contrast targets optimal for photogrammetric measurement.

Several trouble spots are evident in the image in Fig. 10.2. The long exposure time (30 s) required to obtain the images due to the reflective nature of the membrane allowed ambient light to also image on the sail, causing the background to appear much brighter than desired. In the image in Fig. 10.2, ambient light imaging on the upper right corner of the sail drastically reduced the contrast between the dots and the membrane in that area, leading to a loss of target information. Also, there are several "hot spots" in areas where the sail curled, reflecting much more light into the camera than in the rest of image and washing out all data (i.e., targets) in that particular region. Two hot spots are visible in both bottom corners of the image in Fig. 10.2. The low density of the dot pattern creates a low resolution measurement condition, meaning that only the overall shape and not the intricate wrinkle pattern seen in Fig. 10.2 can be adequately characterized from these images. While the long exposure time, hot spots, and low resolution do not preclude measurement, they detract from the achievable accuracy and precision of the process.

Fig. 10.1(b) shows an image of the point cloud and camera locations created from the 3D viewer in the photogrammetry software, which can be studied to verify that the project processed correctly and that the setup and result are as expected. The four camera stations (one in each corner of the sail) and the final point cloud are positioned as expected. This result demonstrates that the camera positions have been calculated successfully and that the point location calculations have produced a nearly planer three-dimensional cloud, expected when measuring a predominantly flat membrane.

Fig. 10.2 demonstrates how the imperfections on the upper right corner in the image affect the photogrammetric processing of the project. Some targets in the area are not visible and therefore could not be marked (marked targets are identified by an asterisk). Several other targets do not have sufficient contrast to be marked using the automatic LSM process and therefore were marked by hand, reducing precision. The greatest amount of wrinkling occurs at the corners of the membrane making them important in the measurement. The ambient light, therefore, has caused a loss of accuracy and data in one of the most critical areas of the sail.

The photogrammetry software estimates precision using error propagation techniques. The average of all the precision values for all of the points in the project was calculated to be 0.16 mm, meaning that overall for the two meter sail, the measurements were precise to one part in 12,500 (1:12,500). The three-dimensional point cloud corresponding to centers (centriods) of the targets was imported into a contour mapping program, which was used to visualize the membrane shape. The first step in the visualization involved the creation of a continuous surface from the imported, discrete data; a process called gridding. Several different algorithms are available to the user during grid creation, depending on the amount of smoothing and interpolation desired. Subsequently the grid was displayed as a shaded surface representing the out of plane deflection of the membrane surface.

The results of the mapping for the gathered photogrammetry data are shown in Fig. 10.3. The shaded surface shows the overall low-resolution shape of the membrane. This type of surface measurement is useful for assessing the overall shape of the structure (e.g., is it warped or flat), but is of little value for characterizing wrinkle patterns, which requires high-resolution data. However this experiment does demonstrate the feasibility of using non-contact dot projection photogrammetry to obtain surface shape models of highly reflective aluminized membranes. A test to measure wrinkle pattern and amplitudes of this same test article is detailed in the following section.

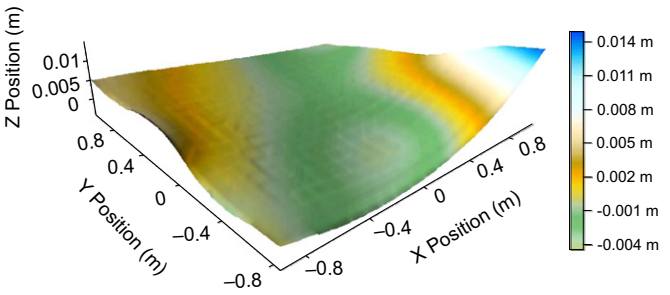

Fig. 10.3. Shaded surface for low density measurements of the solar sail test article (*Z* position amplified).

Fig. 10.4. Two-meter Kapton solar sail test article rotated slightly with gravity-induced billow.

10.1.2. High density field

The high density full-field test described here was designed to generate measurements of comparable resolution to the results in the above high resolution wrinkle test over the entire surface of the two meter Kapton solar sail. The same test article was used once again, however the sail was rotated slightly, as shown in Fig. 10.4, to create a small gravity-induced billow in the bottom half of the membrane. The billow was used to demonstrate the ability of the method to simultaneously measure both medium-amplitude wrinkles and global non-planar shapes. Four professional digital cameras at 90° angles of separation at the corners of the membrane simultaneously photographed a grid of approximately 10,800 targets created by high power industrial flash projector. The use of the professional cameras and turn-key projector signify a transition to professional grade hardware designed to yield full-field, high-resolution, high precision measurements the 2 msolar sail structure.

One image used in the photogrammetric processing is shown in Fig. 10.5. Ambient room lighting was minimized, but data was still lost due to the intensity of the flash projector. Because of the billow in the sail and the angles involved, a percentage of the light reflected by the membrane fell onto the floor. The high intensity of the projector meant a large amount of light, when scattered in all directions by the floor, imaged back onto the membrane. These images of the light on the floor were of sufficient intensity to wash out the original points. Curling of the membrane and the large distances involved again led to hot spots in the images;

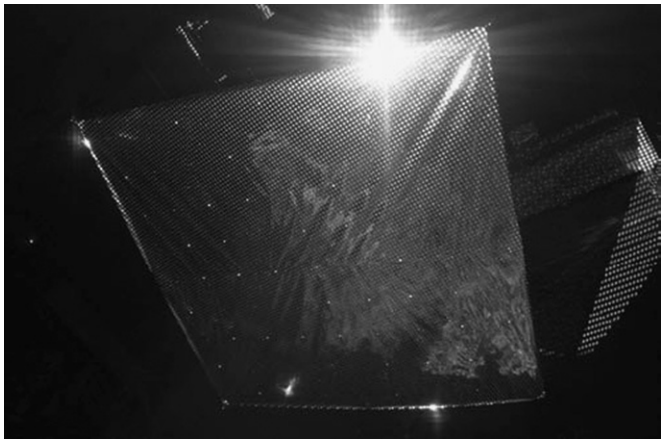

Fig. 10.5. Image used in photogrammetric processing.

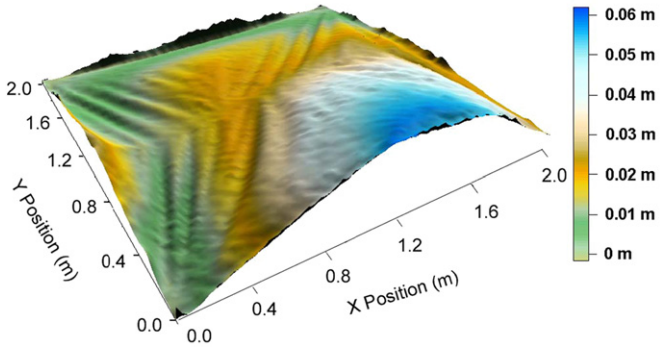

Fig. 10.6. Two views of the contour surface generated.

however all of the data loss was compensated for again by the redundancy of four cameras.

A three dimensional point cloud again resulted from the photogrammetric processing. The time required to generate the final results, however, was much greater than in the two previous examples (three weeks vs. one). The current photogrammetry software was not designed to process such a large number of points, over 10,000 in this measurement, or to handle such close point spacing. Approximately 10,800 dots were projected onto the membrane, and with the small size of the targets and the distance from the test article to the cameras (approximately 3 m), some dots appeared as small as 5 pixel in diameter with as little as 5 pixel spacing. Higher pattern resolution or larger dots are therefore impractical for this measurement given the current hardware configuration. The most important improvement of this measurement over the previous one is evident in the precision numbers. Over the four square meters of membrane area imaged, the professional system was precise to 59 μm versus 62 μm over less than 0.5 m^2 imaged previously, meaning that the overall precision increased from 1:32,300 to 1:50,800.

The shaded surface shown in Fig. 10.6 clearly characterizes all the medium-amplitude wrinkles, the seam, and the billow seen in Fig. 10.4. This plot details the entire surface of the test article instead of just a small area as in the previous application. The wrinkles are clearly evident, but in addition it is possible to see the true size of the billow compared to the wrinkles. The measured wrinkles are on average 5 mm in amplitude, matching the measurement in the previous section, while the billow is almost ten times that size. Also apparent in Fig. 10.4 is the tendency of the membrane to curl at the edges. The shape characterization produced here is unique. A realistic solar sail model has never before been achieved in a full-field, totally non-contact manner to this resolution. This surface model is of sufficient quality to be used for validation of analytical models and for supporting development of hardware and software tools for future measurements and use in space, achieving both of the stated goals.

10.2. Dynamic analysis of 2-m Vellum solar sail

Structural dynamic characterization is also important for the development and validation of analytical models supporting future designs of gossamer structures in general and solar sails in particular. In the dynamic analysis of these structures, as in the static characterization, non-contact measurement is necessary to avoid altering the responses of the objects being measured. Videogrammetry expands the methods and techniques of photogrammetry to multiple time steps yielding dynamic data. While other non-contact dynamic measurement techniques exist, they are not full-field. It was hoped that the dynamic data generated would be useful in simply tracking the overall shape of the membrane as a function of time. The accuracy of the measurement of the resonant frequencies and operating deflection shapes that were extracted, however, surpassed all expectations [12].

Fig. 10.7. Two-meter four quadrant Vellum solar sail test article.

Fig. 10.7 shows the two meter solar sail test article measured in this application. The test article membranes are 100 μm thick Vellum, a diffuse white material ideal for dot projection since it scatters light almost equally in all directions regardless of the angle of incidence. This property enables the Vellum to yield a grid of uniform contrast from any camera angle. The test article is not designed to approximate actual solar sail material as is the test article used in the first three applications, but is designed as a research tool for measurement method development. Fig. 10.8 shows the test setup used in the experiment. A grid of 49 dots was created on the right quadrant of the four quadrant solar sail by a digital projector and retro-reflective targets were attached to the booms. A long-stroke electrodynamic shaker attached to the tip of the lower right boom excited the structure with a pseudo-random forcing function. A turn-key scanning laser vibrometer measured the frequency response function of the sail quadrant and its

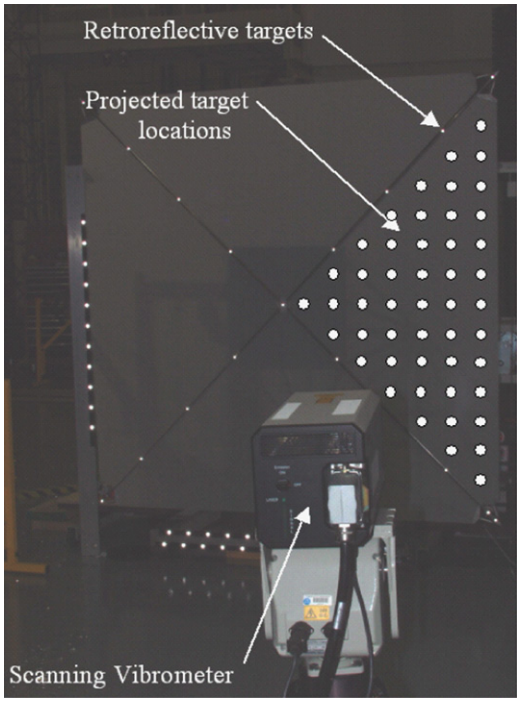

Fig. 10.8. Test setup for dynamic characterization.

corresponding operating deflection shapes, and is used as a standard against which to compare and determine the validity of the videogrammetric results.

At high resolutions, the vibrometer measures thousands of FFT lines at each point, 1600 in this application, to produce detailed results. However this form of data acquisition by scanning each point individually is slow at low frequencies, requiring several hours to run one test. Videogrammetry is attractive because of its ability to measure all of the points simultaneously. For the results presented here, the cameras recorded data for approximately 10 s gathering a total of only 384 frames each instead of several sets of 3200 samples (twice the number of FFT lines) taken by the vibrometer at each point. While the videogrammetric results shown below are arguably not as clean as the vibrometer data, they are full-field, simultaneous measurements taken in just a few seconds instead of hours.

The time-dependent videogrammetric data of the positions was loaded into modal analysis software for interpretation where two different computational methods were used. The first involved overlaying the time histories of individual points and calculating the Fourier transform of the joint history. The software then animated the operating deflection shapes (ODS) at each peak in the frequency domain. The second method of analysis calculated frequency response functions (FRF). Here only one degree of freedom was used, the out-of-plane displacement in the *Z* direction, identical to that used by the vibrometer. For the videogrammetry experiment the input signal was not measured, so a non-node reference point on the membrane was specified enabling the software to calculate the FRF's and animate shapes again at the peaks in the frequency domain. The combined results of both of these methods of analysis are compared against the results of the laser vibrometer measurements in Table 10.1. While neither the ODS or FRF method is currently considered to be entirely accurate, some combination of the two will likely capture all dynamics below 5 Hz. Note that the non-linear nature of the deflection shapes, their coupling, and the inability to compensate for atmospheric damping mean that the shapes shown in Figs. 10.9–10.13 are not actually mode shapes, and that the

Table 10.1
Identified resonant frequencies of the 2 m Vellum solar sail.

Laser vibrometer (Hz)	Videogrammetry
1.75	1.77 Hz (ODS)
2.65	2.49 Hz (FRF, ODS)
	2.81 Hz (ODS)
3.34	3.28 Hz (FRF)
3.67	3.69 Hz (ODS, FRF)
4.74	4.75 Hz (ODS, FRF)

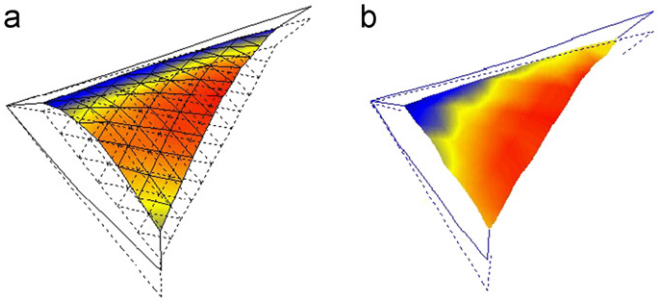

Fig. 10.9. First deflection shape comparison for Vellum solar sail test article, (a) 1.75 Hz Laser Vibrometer, and (b) 1.77 Hz Videogrammetry (ODS).

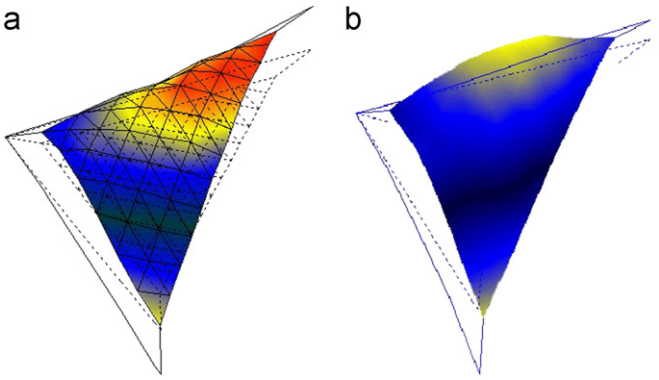

Fig. 10.10. Second deflection shape comparison for Vellum solar sail test article, (a) 2.65 Hz Laser Vibrometer, and (b) 2.49 Hz Videogrammetry (FRF).

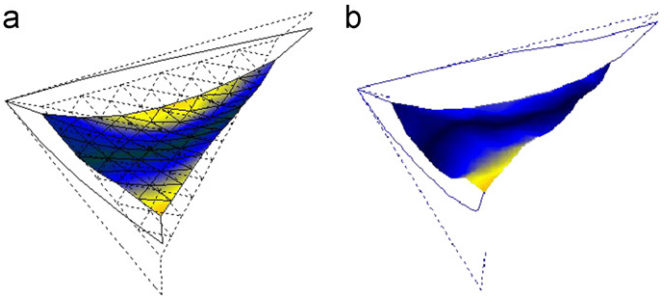

Fig. 10.11. Third deflection shape comparison for Vellum solar sail test article, (a) 3.34 Hz Laser Vibrometer, and (b) 3.28 Hz Videogrammetry (FRF).

frequencies listed in Table 10.1 are not actually modal frequencies. These can alternatively be referred to as "structural resonances" and "resonant frequencies [14,7].

Examination of Table 10.1 reveals good correlation between the results found using laser vibrometry and videogrammetry. While several inconsistencies are evident, overall the resonant frequencies were measured to within 0.2 Hz of each other. The deflection shapes are shown in Figs. 10.9–10.13.

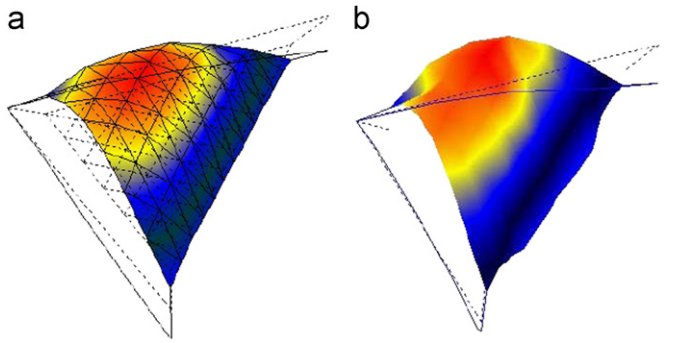

Fig. 10.12. Fourth deflection shape comparison for Vellum solar sail test article, (a) 3.67 Hz Laser Vibrometer, and (b) 3.69 Hz Videogrammetry (FRF).

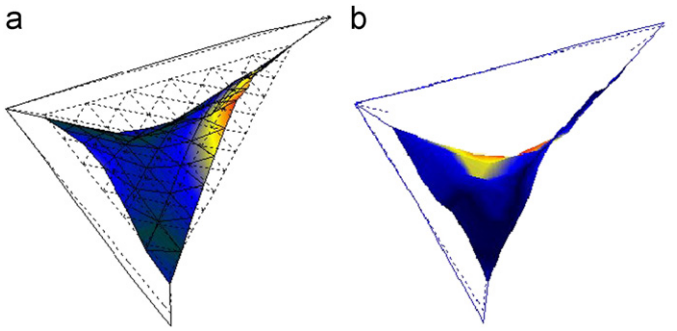

Fig. 10.13. Fifth deflection shape comparison for Vellum solar sail test article, (a) 4.74 Hz Laser Vibrometer, and (b) 4.75 Hz Videogrammetry (FRF).

The first two shapes shown in Figs. 10.9 and 10.10 are basically boom driven modes. The first deflection shape shows that the booms are in phase, and the second shows the booms to be out of phase with the membrane following in a first order fashion. Fig. 10.11 shows the third deflection shape of the system, with the booms in phase and the membrane in a second order configuration. The fourth deflection shape (see Fig. 10.12) shows the booms to be in phase with a large amplitude first order billow of the membrane. Finally, the fifth deflection shape in Fig. 10.13 shows a saddle configuration for the membrane. In all of the figures videogrammetry produced similar shapes at similar frequencies as the vibrometer, demonstrating the potential of the full-field non-contact dynamic characterization technique.

Videogrammetry can only measure frequencies up to approximately one half of the frame rate of the cameras without using stroboscopic flashes. This limitation will not generally be a hindrance for use on gossamer structures because the dominant modes will occur below 5.0 Hz. Also, the displacement of the test article must be large enough to be detected by the cameras, whereas the vibrometer is much more sensitive. The above results show videogrammetry to be capable of achieving full-field non-contact dynamic measurements of solar sail structures.

11. Conclusions

Photogrammetric techniques are useful image-based tools in aerospace application to measure the physical quantities relevant to flight vehicles such wing deformation, model attitude/position, surface shape and dynamics. The theoretical foundation is the perspective projection transformation, i.e., the collinearity equations, that establishes the relationship between the image plane and the 3D object space. Camera calibration/orientation is the key procedure to determine the exterior and interior orientation parameters in the collinearity equations. Due to limited optical access in most aerospace facilities, single-view camera calibration/orientation is highly desirable, and therefore the optimization method coupled with the direct linear transformation (DLT) or a closed-form resection solution is developed for various experiments at NASA. Aeroelastic wing and blade deformation and model attitude measurements have been routinely conducted in large wind tunnels at NASA and AEDC. In addition, special measurements have been made on smart wing deformation, in-flight wing deformation, aerodynamic load determination, and dynamics of thin-plate-wing flutter. In fact, photogrammetry is essential to all quantitative image-based flow diagnostic and visualization techniques since it provides the relationship between the image plane and the object space. Pressure and temperature sensitive paints (PSP and TSP) and other surface measurement techniques require mapping data from images onto a 3D surface of an object. The perspective projection transformation is critical to reconstruct 3D displacement (or velocity) vectors in stereoscopic and tomographic particle image velocimetry (PIV). Photogrammetry is used in accurate determination of the aircraft position and attitude for vision-based autonomous landing and navigation. Such vision-based systems are applicable to small general aviation aircraft as well as unmanned-air-vehicles (UAVs) and micro-air-vehicles (MAVs). Photogrammetry is particularly suitable for non-contact measurements of surface shapes and dynamics of gossamer space structures like deployable ballutes for aerobraking on Mars, telescope sunshields and membrane space solar arrays. Commercial photogrammetric systems and software have been used in ground-based laboratory tests. However, since most gossamer space structures rely on ultra-thin membranes, high-density projected targets and laser-induced fluorescence targets are preferred.

Acknowledgments:

Richard S. Pappa, NASA Langley Research Center, is acknowledged for contributions, especially in the sections on gossamer space structures. The staffs of NASA Langley, Ames, and Dryden, as well as AEDC are acknowledged for testing in the various facilities mentioned here. Test team members from The Boeing Company and the former McDonnell Douglas Aircraft, especially the late Frank Wright, are acknowledged for discussions and explanations regarding the use and value of wind tunnel model deformation data. The authors also thank Justin Littell, ATK Space Systems, Inc for his contributions on the studies reported at the NASA LandIR (gantry) on impact dynamics research vehicles.

Appendix A. Analytical techniques for camera calibration/orientation

A1. Direct linear transformation (DLT)

Rearranging the terms in the collinearity Eq. (2.3) leads to the DLT equations

$$L_1X+L_2Y+L_3Z+L_4-(x+\mathrm{d}x)(L_9X+L_{10}Y+L_{11}Z+1)=0$$
$$L_5X+L_6Y+L_7Z+L_8-(y+\mathrm{d}y)(L_9X+L_{10}Y+L_{11}Z+1)=0 \quad \text{(A1)}$$

The DLT parameters $L_1,\ldots L_{11}$ are related to the camera exterior and interior orientation parameters $(\omega,\phi,\kappa, X_c, Y_c, Z_c)$ and (c, x_p, y_p) [77]. Unlike the standard collinearity equations, Eq. (A1) is linear for the DLT parameters when the lens distortion terms dx and dy are neglected. In fact, the DLT is a linear treatment of what is essentially a non-linear problem at the cost of introducing two additional parameters. The matrix form of the linear DLT equations for M targets is $\boldsymbol{B}\ \boldsymbol{L}=\boldsymbol{C}$, where $\boldsymbol{L}=(L_1,\ldots L_{11})^T$,

$\boldsymbol{C}=(x_1,y_1,\ldots x_M,y_M)^T$, and $\boldsymbol{B}$ is the $2M\times 11$ configuration matrix that can be directly obtained from Eq. (A1). Without using an initial guess, a least-squares solution for $\boldsymbol{L}$ is formally given by $\boldsymbol{L}=(\boldsymbol{B^TB})^{-1}\boldsymbol{B^TC}$. The camera orientation parameters can be extracted from the DLT parameters from the following expressions

$$x_p=(L_1L_9+L_2L_{10}+L_3L_{11})L^2,\ y_p=(L_5L_9+L_6L_{10}+L_7L_{11})L^2,$$
$$c=\sqrt{(L_1^2+L_2^2+L_3^2)L^2-x_p^2},\ \phi=\sin^{-1}(L_9L),$$
$$\omega=\tan^{-1}(-L_{10}/L_{11}),\ \kappa=\cos^{-1}(m_{11}/\cos(\phi)),$$
$$m_{11}=L(x_pL_9-L_1)/c,\ L=-(L_9^2+L_{10}^2+L_{11}^2)^{-1/2},$$
$$\begin{pmatrix}X_c\\Y_c\\Z_c\end{pmatrix}=-\begin{pmatrix}L_1&L_2&L_3\\L_5&L_6&L_7\\L_9&L_{10}&L_{11}\end{pmatrix}\begin{pmatrix}L_4\\L_8\\1\end{pmatrix}. \tag{A2}$$

A2. Closed-form resection solution

The closed-form resection solution given by Zeng and Wang [111] based on three points is recapitulated in a more concise index notation, which is useful for initial estimates of the exterior orientation parameters. When the principal point is at $(x_p,y_p)=(0,0)$, without lens distortion, the collinearity equations for three targets can be rewritten as $x_i^1=-c\overline{X}_i^1/\overline{X}_i^3$ and $x_i^2=-c\overline{X}_i^2/\overline{X}_i^3$ $(i=1,2,3)$. The coordinates $\overline{\boldsymbol{X}}_i=(\overline{X}_i^1,\overline{X}_i^2,\overline{X}_i^3)^T$ or $\overline{X}_i^j=\boldsymbol{m_j}\bullet(\boldsymbol{X_i}-\boldsymbol{X_c})$ are the projections of the object space position vector $\boldsymbol{X}-\boldsymbol{X_c}$ in a local object space coordinate frame $(\boldsymbol{m}_1,\boldsymbol{m}_2,-\boldsymbol{m}_3)$ located at the optical center $\boldsymbol{X_c}$. Here, the coordinate system $(\boldsymbol{m}_1,\boldsymbol{m}_2,-\boldsymbol{m}_3)$ is used such that it is consistent with that used by Zeng and Wang [111]. The index 'i' denotes a particular target. The corresponding image point of the target 'i' is $\boldsymbol{x}_i=(x_i^1,x_i^2)^T$. The vectors $\boldsymbol{m}_1=(m_{11},m_{12},m_{13})^T$ and $\boldsymbol{m}_2=(m_{21},m_{22},m_{23})^T$ are the directional cosine vectors parallel to the x^1-axis, x^2-axis in the image plane, respectively. The vector $\boldsymbol{m}_3=(m_{31},m_{32},m_{33})^T$ is normal to the image plane, directing from the principal point to the optical center along the optical axis. The distances between two of three targets are $\sum_{j=1}^3[\overline{X}_1^j-\overline{X}_2^j]^2=L_3^2$, $\sum_{j=1}^3[\overline{X}_2^j-\overline{X}_3^j]^2=L_1^2$, and $\sum_{j=1}^3[\overline{X}_3^j-\overline{X}_1^j]^2=L_2^2$, where L_1, L_2 and L_3 are the distances between two targets that are known when the coordinates of the three targets are given. Eliminating $\overline{X}_i^1$ and $\overline{X}_i^2$ in the above equations, we have

$$A_{11}(\overline{X}_1^3)^2-2A_{12}\overline{X}_1^3\overline{X}_2^3+A_{22}(\overline{X}_2^3)^2=L_3^2, \tag{A3}$$

$$A_{22}(\overline{X}_2^3)^2-2A_{23}\overline{X}_2^3\overline{X}_3^3+A_{33}(\overline{X}_3^3)^2=L_1^2, \tag{A4}$$

$$A_{33}(\overline{X}_3^3)^2-2A_{31}\overline{X}_3^3\overline{X}_1^3+A_{11}(\overline{X}_1^3)^2=L_2^2. \tag{A5}$$

The coefficients in Eqs. (A3)–(A5) are given by $A_{ij}=\boldsymbol{r}_i\bullet\boldsymbol{r}_j/c^2$, where $\boldsymbol{r}_i=(x_i^1,x_i^2,c)$ is the position vector that points to the target 'i' on the image from the origin (optical center) of the frame $(\boldsymbol{m}_1,\boldsymbol{m}_2,-\boldsymbol{m}_3)$. Further, we know $\overline{X}_i^3=-\boldsymbol{m_3}\bullet(\boldsymbol{X_i}-\boldsymbol{X_c})=-R_i\cos\Theta_i$, where $R_i=|\boldsymbol{X_i}-\boldsymbol{X_c}|$ is the distance between the target "i" and the optical center and Θ_i is the angle between $\boldsymbol{X_i}-\boldsymbol{X_c}$ and $\boldsymbol{m}_3$. Since the vectors $\boldsymbol{X_i}-\boldsymbol{X_c}$ and $\boldsymbol{r}_i=(x_i^1,x_i^2,c)$ are collinear in a perfect perspective projection, we have $\cos^2\Theta_i=c^2/|\boldsymbol{r}_i|^2=1/A_{ii}$ and $\overline{X}_i^3=-R_i/\sqrt{A_{ii}}$. Substituting these relations into Eqs. (A3)–(A5) yields

$$R_1^2-D_1R_1R_2+R_2^2=L_3^2, \tag{A6}$$

$$R_2^2-E_1R_2R_3+R_3^2=L_1^2, \tag{A7}$$

$$R_3^2-F_1R_3R_1+R_1^2=L_2^2. \tag{A8}$$

The coefficients in Eqs. (A6)–(A8) are defined as $D_1=D_{12}$, $E_1=D_{23}$ and $F_1=D_{31}$, where $D_{ij}=2A_{ij}/(A_{ii}A_{jj})^{1/2}$. Since L_i and A_{ij} are known, the distances R_i can be obtained by solving Eqs. (A6)–(A8).

Combining Eqs. (A6)–(A8) and introducing $R_1/p=1$ and $R_3/p=n$ yield a fourth-order algebraic equation for n

$$N_1n^4+N_2n^3+N_3n^2+N_4n+N_5=0, \tag{A9}$$

where

$$N_1=(1-K_{12})^2+K_{32}^2-2(1-K_{12})K_{32}-K_{32}E_1^2+4K_{32}(1-K_{12}),$$
$$N_2=K_{32}F_1(-2-2K_{32}+4K_{12}+E_1^2)+K_{12}(E_1D_1+2F_1-2K_{12}F_1)+E_1D_1(K_{32}-1),$$
$$N_3=K_{32}(K_{32}F_1^2-F_1D_1E_1-4K_{12}+2K_{32}-E_1^2-2K_{12}F_1^2)+K_{12}(K_{12}F_1^2+2K_{12}-F_1E_1D_1-D_1^2)+D_1^2-2+E_1^2,$$
$$N_4=K_{32}(2F_1-2K_{32}F_1+E_1D_1+4K_{12}F_1)+K_{12}(E_1D_1-2K_{12}F_1+F_1D_1^2-2F_1)-D_1E_1,$$
$$N_5=K_{32}(K_{32}-2-2K_{12})+K_{12}(K_{12}-D_1^2+2)+1.$$

Eq. (A9) has either two or four real roots for n since the complex roots are always in conjugate pair. Typically, there are two real roots in photogrammetric applications. Once n is known, R_1 and R_3 can be given by $R_1=L_2(n^2-F_1n+1)^{-1/2}$ and $R_3=nR_1$. There are two solutions for R_2 from Eq. (A6) $R_2=(D_1R_1\pm\sqrt{D_1^2R_1^2-4(R_1^2-L_3^2)})/2$, and two other solutions from Eq. (A7) $R_2=(E_1R_3\pm\sqrt{E_1^2R_3^2-4(R_3^2-L_1^2)})/2$. If R_2 is correct, the values of R_2 given by these two equations should be consistent. Therefore, to satisfy this condition, the number of sets of (R_1,R_2,R_3) can be reduced, and typically two sets of (R_1,R_2,R_3) are selected.

For a given set of (R_1, R_2, R_3), three equations for the camera location $X_c=(X_c, Y_c, Z_c)$ are

$$(X_1-X_c)^2+(Y_1-Y_c)^2+(Z_1-Z_c)^2=R_1^2, \tag{A10}$$

$$(X_2-X_c)^2+(Y_2-Y_c)^2+(Z_2-Z_c)^2=R_2^2, \tag{A11}$$

$$(X_3-X_c)^2+(Y_3-Y_c)^2+(Z_3-Z_c)^2=R_3^2. \tag{A12}$$

For convenience in writing the following expressions, the notations $\boldsymbol{X_c}=(X_c^1, X_c^2, X_c^3)$ and $\boldsymbol{X_i}=(X_i^1, X_i^2, X_i^3)$ are replaced by $\boldsymbol{X_c}=(X_c, Y_c, Z_c)$ and $\boldsymbol{X_i}=(X_i, Y_i, Z_i)$, respectively. The solution to this problem is to find intersection of three spheres, and generally there are two solutions. Eliminating the terms containing X_c^2, Y_c^2 and Z_c^2, we have

$$\Delta X_{21}X_c+\Delta Y_{21}Y_c=C_1,\ \Delta X_{32}X_c+\Delta Y_{32}Y_c=C_2 \tag{A13}$$

where $\Delta X_{21}=X_2-X_1$, $\Delta Y_{21}=Y_2-Y_1$, $\Delta X_{32}=X_3-X_2$, $\Delta Y_{32}=Y_3-Y_2$, $C_1=g_1-\Delta Z_{21}Z_c$, $C_2=g_2-\Delta Z_{32}Z_c$, $\Delta Z_{21}=Z_2-Z_1$, $\Delta Z_{32}=Z_3-Z_2$,

$$g_1=[R_1^2-R_2^2+(X_2^2+Y_2^2+Z_2^2)-(X_1^2+Y_1^2+Z_1^2)]/2,$$
$$g_2=[R_2^2-R_3^2+(X_3^2+Y_3^2+Z_3^2)-(X_2^2+Y_2^2+Z_2^2)]/2.$$

The solutions of Eq. (A13) for X_c and Y_c are related linearly to Z_c, i.e.,

$$X_c=h_{X1}-h_{X2}Z_c,\ Y_c=h_{Y1}-h_{Y2}Z_c, \tag{A14}$$

where

$$h_{X1}=(g_1\Delta Y_{32}-g_2\Delta Y_{21})/\Delta,\ h_{X2}=(\Delta Z_{21}\Delta Y_{32}-\Delta Z_{32}\Delta Y_{21})/\Delta,$$
$$h_{Y1}=(g_2\Delta X_{21}-g_1\Delta X_{32})/\Delta,\ h_{Y2}=(\Delta Z_{32}\Delta X_{21}-\Delta Z_{21}\Delta X_{32})/\Delta,$$
$$\Delta=\Delta X_{21}\Delta Y_{32}-\Delta X_{32}\Delta Y_{21}.$$

Substitution of Eq. (A14) into Eq. (A10) yields a quadratic algebraic equation

$$aZ_c^2+bZ_c+c=0, \tag{A15}$$

where $a=h_{X2}^2+h_{Y2}^2+1$,

$b=2X_1h_{X2}+2Y_1h_{Y2}-2Z_1-2h_{X1}h_{X2}-2h_{Y1}h_{Y2}$,

$c=-R_1^2+(X_1^2+Y_1^2+Z_1^2)-2X_1h_{X1}-2Y_1h_{Y1}+h_{X1}^2+h_{Y1}^2$.

Therefore, for a given set of (R_1, R_2, R_3), we obtain two sets of (X_c, Y_c, Z_c). In order to select the appropriate sets of (X_c,Y_c,Z_c), three targets (1, 2, 3) are numbered in the counterclockwise fashion in both the image plane and object space (viewed from a camera). In this case, the vector $(\boldsymbol{X_2}-\boldsymbol{X_1})\times(\boldsymbol{X_3}-\boldsymbol{X_1})$ is generally in the same direction of the vector $\boldsymbol{X_c}-\boldsymbol{X_1}$. A criterion for the correct perspective relationship is $(\boldsymbol{X_c}-\boldsymbol{X_1})\bullet[(\boldsymbol{X_2}-\boldsymbol{X_1})\times(\boldsymbol{X_3}-\boldsymbol{X_1})]>0$. After the criterion is applied to four sets of (X_c, Y_c, Z_c) obtained from the two sets of (R_1,R_2,R_3), two candidate sets of (X_c, Y_c, Z_c) are typically selected.

The three elements of the vector $\boldsymbol{m}_3$ can be directly obtained by solving the linear system of equations $\boldsymbol{m_3}\bullet(\boldsymbol{X_i}-\boldsymbol{X_c})=-R_i/\sqrt{A_{ii}}$ (i=1,2,3). Similarly, other two vectors $\boldsymbol{m}_1$ and $\boldsymbol{m}_2$ can be determined by solving $\boldsymbol{m_1}\bullet(\boldsymbol{X_i}-\boldsymbol{X_c})=(x_i^1/c)(R_i/\sqrt{A_{ii}})$ and $\boldsymbol{m_2}\bullet(\boldsymbol{X_i}-\boldsymbol{X_c})=(x_i^2/c)(R_i/\sqrt{A_{ii}})$ (i=1,2,3). Therefore, the Euler rotational angles (ω,ϕ,κ) can be extracted using $\omega=\tan^{-1}(-m_{32}/m_{33})$, $\phi=\sin^{-1}(m_{31})$, and $\kappa=\sin^{-1}(-m_{21}/\cos\phi)$. Finally, two sets of the exterior orientation parameters (ω,ϕ,κ, X_c, Y_c, Z_c) are obtained from three known targets. At this stage, however, the unique solution cannot be determined without additional information. When an extra known target is added, two groups of three targets can be used to obtain four sets of the exterior orientation parameters. The correct exterior orientation parameters should remain invariant for two different groups of three targets. Hence, if two sets of the exterior orientation parameters are the same, they should be the correct exterior orientation parameters. In general, this four-point method is able to give a unique solution. The closed-form resection solution, assuming that lens distortion is negligible, the principal point coincides at the geometrical center of the image plane and the principal distance is given, provides an initial estimate of the exterior orientation parameters.

A3. Optimization method

Liu et al. [67] developed an optimization method to cope with strong correlation between the interior and exterior orientation parameters that leads to the singularity of the normal-equation-matrix in least-squares estimation for a complete set of the camera parameters. This method contains two separate but interacting procedures: resection for the exterior orientation parameters and optimization for the interior orientation and lens distortion parameters.

A3.1. Resection for exterior orientation parameters

Resection for the exterior orientation parameters is first carried out for a given set of the interior orientation parameters. When the image coordinates (x_n,y_n) of the nth target are in pixels, the collinearity equations are expressed as

$$f_1=S_hx_n-x_p-\mathrm{d}x+cU/W=0$$
$$f_2=S_vy_n-y_p-\mathrm{d}y+cV/W=0, \tag{A16}$$

where $U=\boldsymbol{m}_1\bullet(\boldsymbol{X_n}-\boldsymbol{X_c})$, $V=\boldsymbol{m}_2\bullet(\boldsymbol{X_n}-\boldsymbol{X_c})$, $W=\boldsymbol{m}_3\bullet(\boldsymbol{X_n}-\boldsymbol{X_c})$, and S_h and S_v are the horizontal and vertical pixel spacings (mm/pixel) of a CCD camera, respectively. In general, the vertical pixel spacing is fixed and known for a CCD camera, but the effective horizontal spacing may be variable depending on the frame grabber used to digitize the image. Thus, an additional parameter, the pixel-spacing-aspect-ratio S_h/S_v, is introduced. We define $\boldsymbol{\Pi_{ex}}=(\omega,\phi,\kappa,\ X_c,\ Y_c,\ Z_c)^T$ for exterior orientation parameters and $\boldsymbol{\Pi_{in}}=(c,\ x_p,\ y_p,\ K_1,\ K_2,\ P_1,\ P_2,\ S_h/S_v)^{\mathrm{T}}$ for the interior orientation and lens distortion parameters. For given values of $\boldsymbol{\Pi_{in}}$, and sets of $\boldsymbol{p_n}=(x_n,\ y_n)^T$ and $\boldsymbol{P_n}=(X_n,\ Y_n,\ Z_n)^T$, $\boldsymbol{\Pi_{ex}}$ in Eq. (A16) can be found by an iterative least-squares solution, referred to in photogrammetry as "resection".

The linearized collinearity equations for targets (n=1, 2,…, M) are written as $\boldsymbol{V}=\boldsymbol{A}(\ \Delta\boldsymbol{\Pi_{ex}}\ )-\boldsymbol{l}$, where $\Delta\boldsymbol{\Pi_{ex}}$ is the correction term for the exterior orientation parameters, $\boldsymbol{V}$ is the $2M\times1$ residual vector, $\boldsymbol{A}$ is the $2M\times6$ configuration matrix, and $\boldsymbol{l}$ is the $2M\times1$ observation vector. The configuration matrix $\boldsymbol{A}$ and observation vector $\boldsymbol{l}$ in the linearized collinearity equations are

$$\boldsymbol{A}=[(\partial f_1/\partial\boldsymbol{\Pi}_{\mathrm{ex}})_1(\partial f_2/\partial\boldsymbol{\Pi}_{\mathrm{ex}})_1\cdots(\partial f_1/\partial\boldsymbol{\Pi}_{\mathrm{ex}})_M\ \ (\partial f_2/\partial\boldsymbol{\Pi}_{\mathrm{ex}})_M]^T,$$
$$\boldsymbol{l}=-[(f_1)_1(f_2)_1\cdots(f_1)_M(f_2)_M]^T,$$

where the operator $\partial/\partial\ \boldsymbol{\Pi_{ex}}$ is defined as $(\partial/\partial\omega,\partial/\partial\varphi,\partial/\partial\kappa,\partial/\partial X_c,\ \partial/\partial Y_c,\partial/\partial Z_c)$ and the subscript denotes the target. The components of the vectors $\partial f_1/\partial\ \boldsymbol{\Pi_{ex}}$ and $\partial f_2/\partial\ \boldsymbol{\Pi_{ex}}$ are

$$\frac{\partial f_1}{\partial\omega}=\frac{c}{W}\left\{m_{12}(Z-Z_c)-m_{13}(Y-Y_c)-\frac{U}{W}[m_{32}(Z-Z_c)-m_{33}(Y-Y_c)]\right\},$$
$$\frac{\partial f_1}{\partial\phi}=\frac{c}{W}\left[-\cos\kappa\ W-\frac{U}{W}(\cos\kappa\ U-\sin\kappa\ V)\right],\ \frac{\partial f_1}{\partial\kappa}=\frac{cV}{W},$$
$$\frac{\partial f_1}{\partial X_c}=\frac{c}{W}\left(-m_{11}+\frac{U}{W}m_{31}\right),\ \frac{\partial f_1}{\partial Y_c}=\frac{c}{W}\left(-m_{12}+\frac{U}{W}m_{32}\right),$$
$$\frac{\partial f_1}{\partial Z_c}=\frac{c}{W}\left(-m_{13}+\frac{U}{W}m_{33}\right),$$
$$\frac{\partial f_2}{\partial\omega}=\frac{c}{W}\left\{m_{22}(Z-Z_c)-m_{23}(Y-Y_c)-\frac{V}{W}[m_{32}(Z-Z_c)-m_{33}(Y-Y_c)]\right\},$$
$$\frac{\partial f_2}{\partial\phi}=\frac{c}{W}\left[\sin\kappa\ W-\frac{V}{W}(\cos\kappa\ U-\sin\kappa\ V)\right],\ \frac{\partial f_2}{\partial\kappa}=-\frac{cU}{W},$$
$$\frac{\partial f_2}{\partial X_c}=\frac{c}{W}\left(-m_{21}+\frac{V}{W}m_{31}\right),\ \frac{\partial f_2}{\partial Y_c}=\frac{c}{W}\left(-m_{22}+\frac{V}{W}m_{32}\right),$$
$$\frac{\partial f_2}{\partial Z_c}=\frac{c}{W}\left(-m_{23}+\frac{V}{W}m_{33}\right).$$

A least-squares solution to minimize the residuals $\boldsymbol{V}$ for the correction term is $\Delta\boldsymbol{\Pi_{ex}}=(\boldsymbol{A^TA})^{-1}\boldsymbol{A^Tl}$. In general, the 6×6 normal-equation-matrix ($\boldsymbol{A^TA}$) can be inverted without singularity since the interior orientation and lens distortion parameters are not included in the least-squares estimation. To obtain such $\boldsymbol{\Pi_{ex}}$ that the correction term becomes zero, the Newton-Raphson iterative method is used for solving the non-linear equation $(\boldsymbol{A^TA})^{-1}\boldsymbol{A^T}l=0$ for $\boldsymbol{\Pi_{ex}}$. This approach converges over considerable ranges of the initial values of $\boldsymbol{\Pi_{ex}}$.

Therefore, for a given $\boldsymbol{\Pi_{in}}$, the corresponding exterior orientation parameter $\boldsymbol{\Pi_{ex}}$ can be obtained and are symbolically expressed as

$$\boldsymbol{\Pi}_{\mathrm{ex}}=\mathrm{RESECTION}(\boldsymbol{\Pi}_{\mathrm{in}}). \tag{A17}$$

At this stage, the exterior orientation parameters $\boldsymbol{\Pi_{ex}}$ obtained from Eq. (A17) are not necessarily correct unless the given interior orientation and lens distortion parameters $\boldsymbol{\Pi_{in}}$ are accurate. Obviously, an extra condition is needed to obtain correct $\boldsymbol{\Pi_{in}}$ and the determination of $\boldsymbol{\Pi_{in}}$ is coupled with the resection for $\boldsymbol{\Pi_{ex}}$. The following section describes an optimization problem to obtain the correct $\boldsymbol{\Pi_{in}}$.

A3.2. Optimization for interior orientation parameters

In order to determine the correct values of $\boldsymbol{\Pi_{in}}$, an extra condition must be given. We note that the correct values of $\boldsymbol{\Pi_{in}}$ are intrinsic constants of a camera/lens system, and they are independent of the target locations $\boldsymbol{p_n}=(x_n,\ y_n)^T$ and $\boldsymbol{P_n}=(X_n,\ Y_n,\ Z_n)^T$. Mathematically, $\boldsymbol{\Pi_{in}}$ is an invariant under a transformation $(\boldsymbol{p}_n,\boldsymbol{P}_n)\mapsto(\boldsymbol{p}_m,\boldsymbol{P}_m)$ ($m\neq n$). By rearranging the collinearity equations with distortion terms, the interior orientation parameters can be expressed in the following form $(c,\ x_p,\ y_p)^T=G(\boldsymbol{p_n},\boldsymbol{P_n},\boldsymbol{\Pi_{in}},\boldsymbol{\Pi_{ex}})$. Therefore, for correct values of $\boldsymbol{\Pi_{in}}$, the quantity

$\boldsymbol{G}(\boldsymbol{p_n}, \boldsymbol{P_n}, \boldsymbol{\Pi_{in}}, \boldsymbol{\Pi_{ex}})$ is an invariant under the transformation $(\boldsymbol{p}_n, \boldsymbol{P}_n) \mapsto (\boldsymbol{p}_m, \boldsymbol{P}_m)$ $(m \neq n)$. In other words, for correct values of $\boldsymbol{\Pi_{in}}$, the standard deviation of $\boldsymbol{G}(\boldsymbol{p_n}, \boldsymbol{P_n}, \boldsymbol{\Pi_{in}}, \boldsymbol{\Pi_{ex}})$ calculated over all targets should be zero, i.e., $\mathrm{std}(\boldsymbol{G}) = [\sum_{n=1}^{M} (\boldsymbol{G} - \langle \boldsymbol{G} \rangle)^2/(M-1)]^{1/2} = \boldsymbol{0}$, where **std** denotes the standard deviation and $\langle \boldsymbol{G} \rangle$ denotes the mean value. Furthermore, since $\mathbf{std}(\boldsymbol{G}) \geq \boldsymbol{0}$ is always valid, the correct $\boldsymbol{\Pi_{in}}$ must correspond to the global minimum point of the function **std**($\boldsymbol{G}$). Hence, the determination of correct $\boldsymbol{\Pi_{in}}$ becomes an optimization problem to seek values of $\boldsymbol{\Pi_{in}}$ that minimize the objective function **std**($\boldsymbol{G}$), i.e., $\mathrm{std}(\boldsymbol{G}) \rightarrow \min$. To solve this multiple-dimensional optimization problem, the sequential golden section search technique is used because of its robustness and simplicity [86]. Since the quantity $\boldsymbol{G}(\boldsymbol{p_n}, \boldsymbol{P_n}, \boldsymbol{\Pi_{in}}, \boldsymbol{\Pi_{ex}})$ is related to $\boldsymbol{\Pi_{ex}}$, the optimization for $\boldsymbol{\Pi_{in}}$ is coupled with the resection for $\boldsymbol{\Pi_{ex}}$. Other appropriate objective functions may also be used. An obvious choice is the root-mean-square (rms) of the residuals of calculated object space coordinates of all targets. In fact, we find that the use of **std**($\boldsymbol{x_p}$) or **std**($\boldsymbol{y_p}$) in optimization is qualitatively equivalent to the use of the rms of the residuals.

In principle, any component of $\mathbf{std}(\boldsymbol{G}) = [\mathrm{std}(c), \mathrm{std}(x_p), \mathrm{std}(y_p)]^T$ can be used as an objective function since minimizing one of three components simultaneously leads to minimization of other components. As will be shown, $\mathrm{std}(x_p)$ and $\mathrm{std}(y_p)$ have a simpler topological structure near the global minimum point than $\mathrm{std}(c)$. Hence, $\mathrm{std}(x_p)$ and $\mathrm{std}(y_p)$ are more appropriate objective functions for optimization. For a simulated 3D field of targets on a step configuration, a typical topological structure of $\mathrm{std}(x_p)$ is shown in Fig. 3.2 near the global minimum point $(c, x_p, y_p) = (28, 0.2, 0.08)$ mm for simulated image of the target field. The function $\mathrm{std}(y_p)$ has a similar topological structure in the parametric space. The topological structure of $\mathrm{std}(x_p)$ or $\mathrm{std}(y_p)$ depends on three-dimensionality of the target field, as shown in Fig. 3.3. The topological structure of $\mathrm{std}(x_p)$ or $\mathrm{std}(y_p)$ can also be affected by random disturbances on the targets, as shown in Fig. 3.5.

The optimization method still requires appropriate initial values to obtain a converged solution even though its convergence ranges of the initial values are quite large. The DLT and closed-form resection method can provide initial approximate values of the exterior orientation parameters $(\omega, \phi, \kappa, X_c, Y_c, Z_c)$ and the principal distance c, where the domain of (ω, ϕ, κ) is defined as $-180^0 \leq \omega \leq 180^0$, $-90^0 \leq \phi \leq 90^0$ and $-180^0 \leq \kappa \leq 180^0$. Using the initial approximations given by the DLT or closed-form resection method, the optimization method gives more accurate estimates of the camera orientation and lens distortion parameters. The standard optimization technique such as the golden section search method can be used to minimize the objective function $\mathrm{std}(x_p)$ in the parametric space (c, x_p, y_p, K_1, K_2, P_1, P_2, S_h/S_v). Combined with the DLT, the optimization method allows a rapid and comprehensive automatic camera calibration to obtain 14 camera parameters from a single image without requiring a guess of the initial values. Note, however, that the optimization method may not work well for lenses with very large amounts of distortion (especially fisheye lenses).

Appendix B. Point correspondence and intersection

To determine three unknown coordinates from multiple views without any *a priori* constraint, the correspondence between two or more images is required for the same physical point in the object space. This is the point correspondence problem in 3D vision. Experimental fluid dynamicists encounter this problem in particle-tracking velocimetry. Longuet-Higgins [74] gave a relation between the corresponding points in two images. Consider two cameras in which the unit vectors $(\boldsymbol{m}_{1(n)}, \boldsymbol{m}_{2(n)}, \boldsymbol{m}_{3(n)})$ constitute a local right-hand coordinate system whose origin is located at the perspective center $X_{c(n)}$, where the index $n = 1, 2$ denotes the cameras 1 and 2. The coordinates $\overline{\boldsymbol{X}}_{(n)} = (\overline{X}^1_{(n)}, \overline{X}^2_{(n)}, \overline{X}^3_{(n)})^T$ in the coordinate frames $(\boldsymbol{m}_{1(n)}, \boldsymbol{m}_{2(n)}, \boldsymbol{m}_{3(n)})$ are related by the translation and rotation transformation $\overline{X}^\alpha_{(2)} = R_{\alpha\beta}(\overline{X}^\beta_{(1)} - T^\beta_r)$, where $\boldsymbol{R} = [R_{\alpha\beta}]$ and $\boldsymbol{T_r} = [T^\beta_r]$ are the rotation matrix and translation vector, respectively. A new matrix $\boldsymbol{Q}$ is given by $\boldsymbol{Q} = \boldsymbol{R}\,\boldsymbol{S}$ or $S_{\alpha\beta} = R_{\alpha\mu} S_{\mu\beta}$, where $\boldsymbol{S}$ is the skew-symmetric matrix $S_{\mu\beta} = \varepsilon_{\mu\beta\sigma} T^\sigma_r$ and the permutation index $\varepsilon_{\mu\beta\sigma} = 1, or\ -1,\ or\ 0$ if (μ, β, σ) is an even, or odd permutation of $(1, 2, 3)$, or otherwise. Thus, we know

$$\overline{X}^\alpha_{(2)} Q_{\alpha\beta} \overline{X}^\beta_{(1)} = R_{\alpha\kappa}(\overline{X}^\kappa_{(1)} - T^\kappa_r) R_{\alpha\mu} \varepsilon_{\mu\beta\sigma} T^\sigma_r \overline{X}^\beta_{(1)} = (\overline{X}^\mu_{(1)} - T^\mu_r) \varepsilon_{\mu\beta\sigma} T^\sigma_r \overline{X}^\beta_{(1)} = 0, \tag{B1}$$

since the rotational matrix $\boldsymbol{R}$ is orthogonal $(R_{\alpha\mu}\, R_{\mu\beta} = \delta_{\alpha\beta})$ and $\varepsilon_{\mu\beta\sigma}$ is anti-symmetric in every pair of its subscripts. When the image coordinates $x^\alpha_{(n)}$ are relative to the principal point, the collinearity equations without lens distortion can be written as a simpler form $x^\alpha_{(n)} = -c\overline{X}^\alpha_{(n)}/\overline{X}^3_{(n)}$, $(n = 1, 2, \alpha = 1, 2, 3)$. Dividing Eq. (B1) by $\overline{X}^3_{(1)} \overline{X}^3_{(2)}/c^2$ yields the Longuet-Higgins equation for the point correspondence

$$x^\alpha_{(2)} Q_{\alpha\beta} x^\beta_{(1)} = 0, \tag{B2}$$

where $\boldsymbol{Q}$ is the fundamental matrix related to the camera exterior orientation parameters. Given a sufficient number of point correspondences between two images, the elements $Q_{\alpha\beta}$ can be determined by solving the algebraic equations $(x^\alpha_{(2)} x^\beta_{(1)})_i Q_{\alpha\beta} = 0$ $(i \geq 8)$ using least-squares method.

The geometrical meaning of Eq. (B2) is related to the epipolar lines in the image plane [81,41]. For a given point $(x^1_{(1)}, x^2_{(1)})$ in the image 1, its epipolar line in the image 2 is projection of a line connecting the object space point and the image point through the optical center of the camera 1 onto the image 2. This epipolar line in the image 2 is given by $x^\alpha_{(2)} p_{\alpha(1)} = 0$, where $p_{\alpha(1)} = Q_{\alpha\beta} x^\beta_{(1)}$ is the coefficients of the epipolar line. Thus, the fundamental matrix $\boldsymbol{Q}$ maps a point in the image 1 to its epipolar line in the image 2 and vice versa. Hence, Eq. (B2) serves as the epipolar constraint to reduce the number of unknowns for establishing the point correspondence between images. When lens distortion exists, the epipolar constraint is $(x^\alpha_{(2)} + \delta x^\alpha_{(2)}) Q_{\alpha\beta} (x^\beta_{(1)} + \delta x^\beta_{(1)}) = 0$, where the lens distortion terms are $[\delta x^\alpha_{(n)}] = (\delta x^1_{(n)}, \delta x^2_{(n)}, 0)^T$. Since the lens distortion terms are non-linear, an epipolar line is a curve rather than a straight line.

For two calibrated cameras, the correspondence between two images can be directly established from the collinearity equations. The collinearity equations for cameras 1 and 2 are written as [69]

$$\boldsymbol{W}_{1(n)} \bullet (\boldsymbol{X} - \boldsymbol{X}_{c(n)}) = 0,\ \boldsymbol{W}_{2(n)} \bullet (\boldsymbol{X} - \boldsymbol{X}_{c(n)}) = 0. \quad (n = 1, 2) \tag{B3}$$

The vectors $\boldsymbol{W}_1$ and $\boldsymbol{W}_2$ are defined as $\boldsymbol{W}_1 = (x^1 - x^1_p + \delta x^1)\boldsymbol{m}_3 + c\boldsymbol{m}_1$ and $\boldsymbol{W}_2 = (x^2 - x^2_p + \delta x^2)\boldsymbol{m}_3 + c\boldsymbol{m}_2$. The different notations of the image and object-space coordinates are used here for more concise tensor expression. The image and object-space coordinates $\boldsymbol{x} = (x^1, x^2)^{\mathrm{T}}$ and $\boldsymbol{X} = (X^1, X^2, X^3)^{\mathrm{T}}$ correspond to (x, y) and (X, Y, Z) used in the most of this paper, respectively. The vectors $\boldsymbol{m}_1 = (m_{11}, m_{12}, m_{13})^T$ and $\boldsymbol{m}_2 = (m_{21}, m_{22}, m_{23})^T$ are the directional cosine vectors parallel to the x^1-axis, x^2-axis in the image plane, respectively. The vector $\boldsymbol{m}_3 = (m_{31}, m_{32}, m_{33})^T$ is normal to the image plane, directing from the principal point to the optical center along the optical axis. The vector $\boldsymbol{W}_1$ is on the plane spanned by the orthogonal unit vectors $\boldsymbol{m}_1$ and $\boldsymbol{m}_3$, while $\boldsymbol{W}_2$ is on a plane spanned by $\boldsymbol{m}_2$ and $\boldsymbol{m}_3$. Geometrically, Eq. (B3) describes two planes normal to $\boldsymbol{W}_1$ and $\boldsymbol{W}_2$, defining an intersection line of the two planes through the optical center $\boldsymbol{X_c}$.

Re-combination of Eq. (B3) yields two systems of linear equations for $\boldsymbol{X}$

$$\boldsymbol{W}_{1\mathrm{com}}\boldsymbol{X}=\boldsymbol{B}_{1\mathrm{com}} \text{ and } \boldsymbol{W}_{2\,\mathrm{com}}\boldsymbol{X}=\boldsymbol{B}_{2\mathrm{com}} \tag{B4}$$

where the composite matrices and vectors are

$$\boldsymbol{W}_{1\mathrm{com}}=\begin{pmatrix}\boldsymbol{W}^T_{1(1)}\\ \boldsymbol{W}^T_{2(1)}\\ \boldsymbol{W}^T_{1(2)}\end{pmatrix},\quad \boldsymbol{W}_{2\,\mathrm{com}}=\begin{pmatrix}\boldsymbol{W}^T_{1(1)}\\ \boldsymbol{W}^T_{2(1)}\\ \boldsymbol{W}^T_{2(2)}\end{pmatrix},$$

$$\boldsymbol{B}_{1\mathrm{com}}=\begin{pmatrix}\boldsymbol{W}^T_{1(1)}\boldsymbol{X}_{\boldsymbol{c}(1)}\\ \boldsymbol{W}^T_{2(1)}\boldsymbol{X}_{\boldsymbol{c}(1)}\\ \boldsymbol{W}^T_{1(2)}\boldsymbol{X}_{\boldsymbol{c}(2)}\end{pmatrix},\quad \boldsymbol{B}_{2\mathrm{com}}=\begin{pmatrix}\boldsymbol{W}^T_{1(1)}\boldsymbol{X}_{\boldsymbol{c}(1)}\\ \boldsymbol{W}^T_{2(1)}\boldsymbol{X}_{\boldsymbol{c}(1)}\\ \boldsymbol{W}^T_{2(2)}\boldsymbol{X}_{\boldsymbol{c}(2)}\end{pmatrix}. \tag{B5}$$

For two calibrated cameras, eliminating $\boldsymbol{X}$ from Eq. (B4), we obtain a relation between the image coordinates $(x^1_{(1)}, x^2_{(1)})$ and $(x^1_{(2)}, x^2_{(2)})$,

$$\boldsymbol{G}(x^1_{(1)}, x^2_{(1)};\, x^1_{(2)}, x^2_{(2)})=\boldsymbol{W}_{1\mathrm{com}}\boldsymbol{W}^{-\boldsymbol{1}}_{2\mathrm{com}}\boldsymbol{B}_{2\mathrm{com}}-\boldsymbol{B}_{1\mathrm{com}}=\boldsymbol{0}. \tag{B6}$$

For a point $(x^1_{(1)},x^2_{(1)})$ in the image 1, its epipolar line in the image 2 is given by $\|\boldsymbol{G}(x^1_{(1)},x^2_{(1)};x^1_{(2)},x^2_{(2)})\|\rightarrow\min$. In general, the epipolar line given by this minimization method is not a straight line due to lens distortion. This minimization method takes a longer computational time to obtain an epipolar line. Although it is not a problem for simulations, it is not suitable to implementation of this algorithm to a real vision system. Thus, as an alternative, we use this minimization method to determine the coefficients $Q_{\alpha\beta}$ in the Longuet-Higgins equation $x^{\alpha}_{(2)}Q_{\alpha\beta}x^{\beta}_{(1)}=0$ for the point correspondence. As long as $Q_{\alpha\beta}$ are known, an epipolar line can be instantly obtained using the Longuet-Higgins equation for a given image point.

The Longuet-Higgins equation indicates that a point in the image 1 corresponds to its epipolar line on the image 2 and vice versa. Therefore, the point correspondence is not uniquely established between a pair of images since for a given image point $(x^1_{(1)}, x^2_{(1)})$, there is only one equation for two unknowns $(x^1_{(2)}, x^2_{(2)})$. In order to establish the point correspondence between images, at least four cameras (or four images) are needed. For four cameras or images, the Longuet-Higgins equations are $x^{\alpha}_{h(i)}\,Q_{\alpha\beta(i,j)}\,x^{\beta}_{h(j)}=0$ $(i=1,2,3,4, j=1,2,3,4)$ where the subscript (i,j) denotes a pair of images. There are six pairs of images $(i,j)=(1,2), (1,3), (1,4), (2,3), (2,4)$ and $(3,4)$. Hence, for given $Q_{\alpha\beta(i,j)}$ and $(x^1_{(1)}, x^2_{(1)})$, we have a system of six quadratic equations for six unknowns $(x^1_{(2)}, x^2_{(2)}, x^1_{(3)}, x^2_{(3)}, x^1_{(4)}, x^2_{(4)},)$. The solution can be found using an iterative method.

Appendix C. Vibration of thin rectangular plate

The differential equation for the displacement w of a vibrating plate is generally expressed by

$$L[w(P,t)]+\frac{\partial}{\partial t}C[w(P,t)]+M(P)\frac{\partial^2 w(P,t)}{\partial t^2}=F(P,t), \tag{C1}$$

where P denotes the coordinates x and y, L is a linear differential operator, C is a linear homogenous differential operator for damping, M is also a linear operator, and $F(P,t)$ is an external distributed force on the plate. For a homogenous plate, the operator L is the stiffness distribution $L=D_E\nabla^4$, where $D_E=Eh^2/12(1-\nu^2)$ is the plate flexural rigidity, and $M(P)$ is the mass distribution. Consider a rectangular thin plate clamped at one end. The plate length from the clamped end to the free end is b and the plate width is a. The y-coordinate directs from the clamped end to the free end along the edge. The x-coordinate directs from the one corner to another corner along the clamped edge.

The displacement w of a vibrating plate is given by an expansion based on the eigenfunctions $w_r(x,y)$ [79]

$$w(x,y,t)=\sum_{r=1}^{\infty}w_r(x,y)\eta_r(t), \tag{C2}$$

where $\eta_r(t)$ are the time-dependent amplitudes. The eigenfunctions are given by

$$w_r(x,y)=X_m(x)Y_n(y), \tag{C3}$$

where $X_m(x)$ and $Y_n(y)$ are the characteristic beam functions [90,107]. For the edge $y=0$ clamped and the other edge $y=b$ free, the characteristic beam function $Y_n(y)$ is $Y_n(y)=\cos\gamma_n\bar{y}-\cosh\gamma_n\bar{y}+k_n(\sin\gamma_n\bar{y}-\sinh\gamma_n\bar{y})$ $(n=1,2,3,\ldots)$, where $\bar{y}=y/b$ is the normalized coordinate and $k_n=(\sin\gamma_n-\sinh\gamma_n)/(\cos\gamma_n+\cosh\gamma_n)$. The values of γ_n are given by solving the nonlinear equation $\cos\gamma_n\ \cosh\gamma_n+1=0$. The first three values of γ_n are $\gamma_1=1.875$, $\gamma_2=4.694$ and $\gamma_3=7.8547$. For the edges $x=0$ and $x=a$ free, the characteristic beam functions $X_m(x)$ are $X_m(x)=1$ $(m=0)$, $X_m(x)=1-2\bar{x}$ $(m=1)$,

$$X_m(x)=\cos\mu_m(\bar{x}-1/2)+\beta_m\cosh\mu_m(\bar{x}-1/2)\quad(m=2,4,6,\ldots)$$
$$X_m(x)=\sin\lambda_m(\bar{x}-1/2)+\alpha_m\sinh\lambda_m(\bar{x}-1/2)\quad(m=3,5,7,\ldots)$$

where $\bar{x}=x/a$ is the normalized coordinate, $\beta_m=-\sin(\mu_m/2)/\sinh(\mu_m/2)$, and $\alpha_m=\sin(\lambda_m/2)/\sinh(\lambda_m/2)$. The parameters μ_m and λ_m are given by solving the equations $\tan(\mu_m/2)+\tanh(\mu_m/2)=0$ and $\tan(\lambda_m/2)-\tanh(\lambda_m/2)=0$. The typical values of μ_m and λ_m are $\mu_2=4.73$, $\mu_4=10.99$, $\lambda_3=7.853$, and $\lambda_5=14.137$. The first nine eigenfunctions are then defined as follows

$$\begin{aligned}&w_1(x,y)=X_0(x)Y_1(y),\ w_2(x,y)=X_0(x)Y_2(y),\ w_3(x,y)=X_0(x)Y_3(y),\\ &w_4(x,y)=X_1(x)Y_1(y),\ w_5(x,y)=X_1(x)Y_2(y),\ w_6(x,y)=X_1(x)Y_3(y),\\ &w_7(x,y)=X_2(x)Y_1(y),\ w_8(x,y)=X_2(x)Y_2(y),\ w_9(x,y)=X_2(x)Y_3(y)\end{aligned} \tag{C4}$$

These nine eigenfunctions or mode shapes are illustrated in Fig. 7.20. Usually, the dominant modes are the first and second bending modes $[w_1(x,y)$ and $w_2(x,y)]$ and the first torsion mode $[w_4(x, y)]$.

Since the eigenfunctions are orthogonal, substituting Eq. (C2) into the differential equation, Eq. (C1), for the displacement w of a vibrating plate yields a system of the ordinary differential equations for $\eta_r(t)$

$$\ddot{\eta}_r(t)+\sum_{s=1}^{\infty}c_{rs}\dot{\eta}_s(t)+\omega_r^2\eta_r(t)=N_r(t),\quad(r=1,2,\ldots) \tag{C5}$$

where the damping coefficients are

$$c_{rs}=\int_D w_r(x,y)C[w_s]\mathrm{d}x\,\mathrm{d}y,\quad(r,s=1,2,\ldots) \tag{C6}$$

and the generalized force is

$$N_r(t)=\int_D w_r(x,y)F(x,y,t)\mathrm{d}x\,\mathrm{d}y.\quad r=1,2,\ldots \tag{C7}$$

Note that appropriate dimensional constants are absorbed into Eqs. (C6) and (C7) to make Eq. (C5) dimensionally consistent. It is possible to recover the external force $F(x, y, t)$ from the generalized force $N_r(t)$ that can be considered, according to its definition, as a projected component of $F(x,y,t)$ on the eigenfunction $w_r(x, y)$. Since $w_r(x,y)$ $(r=1,2,\ldots)$ constitutes an orthonormal system, according to the Riesz–Fischer theorem [61] the force $F(x,y,t)$ at a given time can be expressed as

$$F(x,y,t)=M(x,y)\sum_{r=1}^{\infty}w_r(x,y)N_r(t). \tag{C8}$$

Clearly, the fidelity of reconstruction of external force distribution depends on how many modes can be recovered from measurements.

Appendix D. Determination of aircraft attitude and position

D1. Two-camera method based on three points

The ground, aircraft and image coordinate systems are illustrated in Fig. 9.4. In the right-handed aircraft coordinate system (X_{ac}, Y_{ac}, Z_{ac}), the X_{ac} axis directs from the head to the tail along the fuselage, the Y_{ac} axis directs along the right wing and the Z_{ac} axis points upward. The ground coordinate system (X_g, Y_g, Z_g) is located at the end of a runway. The position and orientation of the image coordinate system is fixed relative to the aircraft coordinate system when an aircraft is rigid. The relationship between the image and aircraft coordinate system is determined by camera calibration/orientation on the ground.

To recover the position and attitude of an aircraft relative to the ground coordinate system, as shown in Fig. 9.4(a), two points P_1 and P_2 on the right edge of a runway and third point P_3 on the left edge (viewed from the aircraft) are selected. The coordinates of the points P_1, P_2 and P_3 in the aircraft coordinate system (X_{ac}, Y_{ac}, Z_{ac}) are determined by photogrammetric intersection in a calibrated two-camera vision system mounted on an aircraft. Thus, the triangle $P_1P_2P_3$ defines three unit orthogonal vectors on the ground expressed in the aircraft coordinate system

$$\begin{aligned}
&\boldsymbol{e}_{1g}=\overrightarrow{P_1P_2}/|\overrightarrow{P_1P_2}|=\sum_{i=1}^{3} r_{1i}\boldsymbol{e}_{iac}\\
&\boldsymbol{e}_{2g}=\boldsymbol{e}_{3g}\times\overrightarrow{P_1P_2}/|\boldsymbol{e}_{3g}\times\overrightarrow{P_1P_2}|=\sum_{i=1}^{3} r_{2i}\boldsymbol{e}_{iac}\\
&\boldsymbol{e}_{3g}=\overrightarrow{P_1P_3}\times\overrightarrow{P_1P_2}/|\overrightarrow{P_1P_3}\times\overrightarrow{P_1P_2}|=\sum_{i=1}^{3} r_{3i}\boldsymbol{e}_{iac},
\end{aligned}\tag{D1}$$

where $\boldsymbol{e}_{iac}$ ($i=1,2,3$) are the unit orthogonal vectors along the axes of the aircraft coordinate system. The vectors $\boldsymbol{e}_{ig}$ ($i=1,2,3$) constitute a local coordinate system on the ground. It is assumed that this local system is just a translated ground coordinate system (X_g, Y_g, Z_g) [see Fig. 9.4(a)]. Therefore, Eq. (D1) actually gives a relationship between the ground coordinate system and the aircraft coordinate system. The projection coefficients of the three ground coordinates onto the one aircraft coordinate ($\boldsymbol{e}_{1ac}$) are $r_{11}=\boldsymbol{e}_{1ac}\cdot\boldsymbol{e}_{1g}$, $r_{21}=\boldsymbol{e}_{1ac}\cdot\boldsymbol{e}_{2g}$ and $r_{31}=\boldsymbol{e}_{1ac}\cdot\boldsymbol{e}_{3g}$. Other projection coefficients are similarly defined.

Without loss of generality, the transformation between the ground coordinate system (X_g,Y_g,Z_g) and the aircraft coordinate system (X_{ac},Y_{ac},Z_{ac}) are given by

$$\begin{pmatrix}X_{ac}\\Y_{ac}\\Z_{ac}\end{pmatrix}=\begin{pmatrix}r_{11}&r_{21}&r_{31}\\r_{12}&r_{22}&r_{32}\\r_{13}&r_{23}&r_{33}\end{pmatrix}\begin{pmatrix}X_g-X_{gO_{ac}}\\Y_g-Y_{gO_{ac}}\\Z_g-Z_{gO_{ac}}\end{pmatrix}\equiv R(\phi)R(\theta)R(\psi)\begin{pmatrix}X_g-X_{gO_{ac}}\\Y_g-Y_{gO_{ac}}\\Z_g-Z_{gO_{ac}}\end{pmatrix}.\tag{D2}$$

In Eq. (D2), the sequential rotational transformations between the two systems are defined, where the rotation matrices are

$$R(\phi)=\begin{pmatrix}1&0&0\\0&\cos\phi&\sin\phi\\0&-\sin\phi&\cos\phi\end{pmatrix},\ R(\theta)=\begin{pmatrix}\cos\theta&0&-\sin\theta\\0&1&0\\\sin\theta&1&\cos\theta\end{pmatrix},$$
$$R(\psi)=\begin{pmatrix}\cos\psi&\sin\psi&0\\-\sin\psi&\cos\psi&0\\0&0&1\end{pmatrix},\tag{D3}$$

and ($X_{gO_{ac}}$, $Y_{gO_{ac}}$, $Z_{gO_{ac}}$) are the position coordinates of the aircraft in the ground coordinate system. The elements r_{ij} in Eq. (D2) are

$$\begin{aligned}
&r_{11}=\cos\theta\ \cos\psi,\quad r_{12}=\sin\phi\ \sin\theta\ \cos\psi-\cos\phi\ \sin\psi\\
&r_{13}=\cos\phi\ \sin\theta\ \cos\psi+\sin\phi\ \sin\psi,\quad r_{21}=\cos\theta\ \sin\psi\\
&r_{22}=\sin\phi\ \sin\theta\ \sin\psi+\cos\phi\ \cos\psi,\\
&r_{23}=\cos\phi\sin\theta\ \sin\psi-\sin\phi\ \cos\psi,\\
&r_{31}=-\sin\theta,\quad r_{32}=\sin\phi\ \cos\theta,\quad r_{33}=\cos\phi\ \cos\theta.
\end{aligned}\tag{D4}$$

The inverse transformation of Eq. (D2) is

$$\begin{pmatrix}X_g-X_{gO_{ac}}\\Y_g-Y_{gO_{ac}}\\Z_g-Z_{gO_{ac}}\end{pmatrix}=R^{-1}(\psi)R^{-1}(\theta)R^{-1}(\phi)\begin{pmatrix}X_{ac}\\Y_{ac}\\Z_{ac}\end{pmatrix}.\tag{D5}$$

According to the typical notation in flight dynamics, the Euler angles ϕ, θ, and ψ are the roll, pitch and yaw angles of an aircraft relative to the ground coordinate system. In an approximate sense, the rotation $R^{-1}(\phi)$ is around the X_{ac} axis and the positive roll angle ϕ means the clockwise rotation. The rotation $R^{-1}(\theta)$ is around the Y_{ac} axis and the positive pitch angle θ means the counterclockwise (nose-up) rotation. The rotation $R^{-1}(\psi)$ is around the Z_{ac} axis and the positive yaw angle ψ means the clockwise rotation. Fig. 9.4(c) illustrates the roll, pitch and yaw rotations of an aircraft defined by $R^{-1}(\phi)$, $R^{-1}(\theta)$ and $R^{-1}(\psi)$.

Since the elements (projection coefficients) r_{ij} can be obtained directly from the vectors defined by the triangle $P_1P_2P_3$ in Eq. (D1), the Euler angles ϕ, θ, and ψ can be extracted from $\tan\phi=r_{32}/r_{33}$, $\sin\theta=-r_{31}$ and $\tan\psi=r_{21}/r_{11}$. Therefore, the aircraft attitude is determined. The position O_{ac} of the aircraft relative to the point P_1 in the ground coordinate system is given by

$$\begin{aligned}
X_{gO_{ac}}-X_{gP_1}&=\overrightarrow{P_1O_{ac}}\bullet\boldsymbol{e}_{1g},\ Y_{gO_{ac}}-Y_{gP_1}=\overrightarrow{P_1O_{ac}}\bullet\boldsymbol{e}_{2g},\ Z_{gO_{ac}}-Z_{gP_1}\\
&=\overrightarrow{P_1O_{ac}}\bullet\boldsymbol{e}_{3g},
\end{aligned}\tag{D6}$$

where (X_{gP_1},Y_{gP_1},Z_{gP_1}) are the coordinates of the point P_1 in the ground coordinate system and $\overrightarrow{P_1O_{ac}}=-(X_{acP_1},Y_{acP_1},Z_{acP_1})^T$ is the vector from the point P_1 to the point O_{ac} in the aircraft coordinate system. When the runway is flat and the runway width is given, from Eq. (D6), we can know the aircraft latitude and the lateral position of the aircraft relative to the runway centerline. However, Eq. (D6) only gives the relative aircraft position along the runway (in the X_g direction). In general, the two-camera (or multiple-camera) approach gives the position and attitude of a landing flight vehicle (aircraft or spacecraft) in the ground coordinate system defined by three selected points.

D2. Single-camera method based on runway edges and horizon

A single-camera method was suggested by Sasa et al. [98] to determine the aircraft position and attitude based on the runway edges and horizon. Here the problem is reformulated. Consider a special case where the aircraft coordinates Y_{ac} and Z_{ac} are aligned with the image coordinates x and y, respectively. Thus, when the lens distortion is corrected, we have the special form of the collinearity equations relating the ground and image coordinate systems

$$\begin{aligned}
-\frac{x}{c}&=\frac{Y_{ac}}{X_{ac}}=\frac{r_{12}(X_g-X_{gO_{ac}})+r_{22}(Y_g-Y_{gO_{ac}})+r_{32}(Z_g-Z_{gO_{ac}})}{r_{11}(X_g-X_{gO_{ac}})+r_{21}(Y_g-Y_{gO_{ac}})+r_{31}(Z_g-Z_{gO_{ac}})}\\
-\frac{y}{c}&=\frac{Z_{ac}}{X_{ac}}=\frac{r_{13}(X_g-X_{gO_{ac}})+r_{23}(Y_g-Y_{gO_{ac}})+r_{33}(Z_g-Z_{gO_{ac}})}{r_{11}(X_g-X_{gO_{ac}})+r_{21}(Y_g-Y_{gO_{ac}})+r_{31}(Z_g-Z_{gO_{ac}})}.
\end{aligned}\tag{D7}$$

The problem is to determine the aircraft position ($X_{gO_{ac}}$, $Y_{gO_{ac}}$, $Z_{gO_{ac}}$) and three attitude angles ϕ, θ, and ψ.

At the vanishing point, when $X_{gO_{ac}}\to-\infty$, Eq. (D7) becomes $-\bar{x}_{vp}=r_{12}/r_{11}$ and $-\bar{y}_{vp}=r_{13}/r_{11}$, where $\bar{x}_{vp}=x_{vp}/c$ and $\bar{y}_{vp}=y_{vp}/c$ are the normalized image coordinates of the vanishing point that can be determined as an intersection between the

runway edges in the image plane. These are two equations for the three unknowns ϕ, θ, and ψ. Consider a straight line $Y_g = g_0 X_g + g_1$ on the flat ground $Z_g = 0$. When $X_{gO_{ac}} \to -\infty$, Eq. (D7) becomes $-\bar{x} = (r_{12} + r_{22} g_0)(r_{11} + r_{21} g_0)^{-1}$ and $-\bar{y} = (r_{13} + r_{23} g_0)\ (r_{11} + r_{21} g_0)^{-1}$, where $\bar{x} = x/c$ and $\bar{y} = y/c$ are the normalized image coordinates. Eliminating the constant g_0, we have a horizon in the image plane $\bar{y} = k_{oh}\bar{x} + k_{1h}$, where $k_{oh} = (r_{21} r_{13} - r_{11} r_{23})(r_{12} r_{21} - r_{22} r_{11})^{-1}$ and $k_{1h} = (r_{22} r_{13} - r_{12} r_{23})(r_{12} r_{21} - r_{22} r_{11})^{-1}$. Further arrangement leads to $k_{oh} = -\tan\phi$, and therefore the roll angle ϕ can be directly determined given the slope of the horizon k_{oh}. Then the pitching and yaw angles θ and ψ can be obtained by solving the non-linear equations $-\bar{x}_{vp} = r_{12}/\ r_{11}$ and $-\bar{y}_{vp} = r_{13}/r_{11}$, given the vanishing point $(\bar{x}_{vp},\ \bar{y}_{vp})$. Note that these equations are very weakly related to the roll angle ϕ and hence it does not contain information on ϕ. This is why the horizon is required for this method. If the horizon cannot be clearly identified in images, a distinct line perpendicular to the runway at the end of the runway is required. For this line, $\bar{y} = k_{oh}\bar{x} + k_{1h}$ is approximately valid as long as the relative distance of an aircraft to the horizontal line is sufficiently large ($|Z_{gO_{ac}}/X_{gO_{ac}}| << 1$). The effect of $|Z_{gO_{ac}}/X_{gO_{ac}}|$ on estimation of the aircraft position and attitude will be evaluated.

Now, we consider the runway edges in the image plane. In the ground coordinates system, the right and left edges of a runway are given by $Y_g = \pm w/2$ and $Z_g = 0$, respectively, where w is the width of the runway. From Eq. (D7), the right and left edges in the image plane are, respectively, given by

$$\bar{y} = k_{o(\pm)}\bar{x} + k_{1(\pm)}. \tag{D8}$$

The coefficients $k_{o(\pm)}$ and $k_{1(\pm)}$ are $k_{o(\pm)} = (a_{2(\pm)} r_{11} - b_{1(\pm)} r_{13})(a_{1(\pm)} r_{11} - b_{1(\pm)} r_{12})^{-1}$ and $k_{1(\pm)} = -(a_{1(\pm)} r_{13} - a_{2(\pm)} r_{12})(a_{1(\pm)} r_{11} - b_{1(\pm)} r_{12})^{-1}$, where $a_{1(\pm)} = r_{22}(\pm 1 - \bar{Y}_{gO_{ac}}) - r_{32}\bar{Z}_{gO_{ac}}$, $b_{1(\pm)} = r_{21}(\pm 1 - \bar{Y}_{gO_{ac}}) - r_{31}\bar{Z}_{gO_{ac}}$, $a_{2(\pm)} = r_{23}(\pm 1 - \bar{Y}_{gO_{ac}}) - r_{33}\bar{Z}_{gO_{ac}}$, and $\bar{Y}_{gO_{ac}} = Y_{gO_{ac}}/(w/2)$ and $\bar{Z}_{gO_{ac}} = Z_{gO_{ac}}/(w/2)$ are the normalized coordinates. Rearrangement of the above relations yields

$$\bar{Z}_{gO_{ac}}/(\pm 1 - \bar{Y}_{gO_{ac}}) = R_{(\pm)}, \tag{D9}$$

where

$$\begin{aligned} R_{(\pm)} &= \frac{k_{0(\pm)}(r_{22} + r_{21}\,\bar{x}_{vp}) - (r_{23} + r_{21}\,\bar{y}_{vp})}{k_{0(\pm)}(r_{32} + r_{31}\,\bar{x}_{vp}) - (r_{33} + r_{31}\,\bar{y}_{vp})} \\ &= \frac{k_{1(\pm)}(r_{22} + r_{21}\,\bar{x}_{vp}) - (r_{22}\bar{y}_{vp} - r_{23}\,\bar{x}_{vp})}{k_{1(\pm)}(r_{32} + r_{31}\,\bar{x}_{vp}) - (r_{32}\bar{y}_{vp} - r_{33}\,\bar{x}_{vp})}. \end{aligned} \tag{D10}$$

From Eq. (D9), the normalized position coordinates are

$$\bar{Y}_{gO_{ac}} = \frac{R_{(+)} + R_{(-)}}{R_{(+)} - R_{(-)}},\ \bar{Z}_{gO_{ac}} = -\frac{2R_{(+)}R_{(-)}}{R_{(+)} - R_{(-)}}. \tag{D11}$$

As long as the three attitude angles and $\bar{Y}_{gO_{ac}}$ and $\bar{Z}_{gO_{ac}}$ are known, the coordinate longitudinal $\bar{X}_{gO_{ac}}$ relative to a reference point on a runway edge can be obtained from Eq. (D7). Essentially, this method is a special camera orientation (resection) method based on the three lines (the two runway edges and the horizon), which is similar to the closed-form resection solution based on three known targets.

References

[1] Abdel-Aziz, YI and Karara, HM. Direct linear transformation from comparator coordinates into object space coordinates in close-range photogrammetry, Proc. ASP/UI Symp. on Close-Range Photogrammetry, Univ. of Illinois at Urbana-Champaign, Urbana, Illinois; 1971. pp. 1–18.

[2] Adrian RJ, Westerweed J. Particle Image Velocimetry. Cambridge: Cambridge University Press; 2011.

[3] Arroyo MP, Greated CA. Stereoscopic particle image velocimetry. Measurement Science and Technology 1991;2(12):1181–6.

[4] Barrows, DA. Videogrammetric model deformation measurement techniques for wind tunnel applications, AIAA Paper 2007-1163, Reno, NV, Jan., 2007.

[5] Barrows, DA, Burner, AW, Berry, FC, Dismond, HR and Cate, KH. Photogrammetric measurements of CEV airbag landing attenuation systems, AIAA Paper 2008-846, Reno, Nevada, January 2008.

[6] Barrows, DA, Burner, AW, Abrego, AI, and Olson, LE. Blade displacement measurements of the full-scale UH-60A airloads rotor, AIAA Paper 2011-3655, Honolulu, Hawaii, June 2011.

[7] Batel M. Operational modal analysis — another way of doing modal testing. Sound and Vibration 2002;36(8):22–7.

[8] Bell JH, McLachlan BG. Image registration for pressure-sensitive paint applications. Experiments in Fluids 1996;22:78–86.

[9] Bell, JH and Burner, AW. Data fusion in wind tunnel testing; combined pressure paint and model deformation measurements (invited), AIAA Paper 98-2500, June 1998.

[10] Bell JH, Shairer ET, Hand LA, Mehta RD. Surface pressure measurements using luminescent coatings. Annual Review of Fluid Mechanics 2001;33:155–206.

[11] Bisplinghoff RL, Ashley H, Halfman RL. Aeroelasticity. New York: Dover; 1996.

[12] Black, JT and Pappa, RS. Photogrammetry and videogrammetry methods for solar sails and other gossamer structures, AIAA Paper 2004-1662, April 2004.

[13] Black JT, Pitcher NA, Reeder MF, Maple RC. Videogrammetric dynamics measurements of a lightweight flexible wing in a wind tunnel. Journal of Aircraft 2010;47(1):172–80.

[14] Blandino, JR, Pappa, RS, and Black JT. Modal identification of membrane structures with videogrammetry and laser vibrometry, AIAA Paper 2003-1745, April 2003.

[15] Brown, DC. A solution to the general problem of multiple station analytical sterotriangulation, RCA Technical Report No. 43, February 1958.

[16] Brown, DC. The bundle adjustment: progress and prospects, Invited Paper, Commission 3, ISPRS Congress, Helsinki, 1976.

[17] Burner AW, Snow WL, Shortis MR, Goad WK. Laboratory calibration and characterization of video cameras. SPIE Vol. 1395 Close-Range Photogrammetry Meets Machine Vision 1990:664–71.

[18] Burner, AW. Zoom lens calibration for wind tunnel measurements, videometrics IV, Proceedings of The International Society for Optical Engineering (SPIE), Vol. 2598, Philadelphia, Pennsylvania; 1995. pp. 19–33.

[19] Burner, AW, Wahls, RA, and Goad, WK. Wing twist measurements at the National Transonic Facility, NASA TM 110229, Feb. 1996.

[20] Burner, AW and Martinson, SD. Automated wing twist measurements under aerodynamic load, AIAA Paper 96-2253, June 1996.

[21] Burner, Aw. Model deformation measurements at NASA Langley Research Center, AGARD Conference Proceedings CP-601: Advanced Aerodynamic Measurement Technology, presented at the 81st Meeting and Symposium of the Fluid Dynamics Panel, Seattle, WA, pp. 34-1 to 34-9, September, 1997.

[22] Burner, AW, Radeztsky, RH and Liu, T. Videometric applications in wind tunnels, videometrics V, Proceedings of The International Society for Optical Engineering (SPIE), Vol. 3174, San Diego, California, pp. 234–247, 1997.

[23] Burner AW, Liu T, Garg S, Bell JH, Morgan DG. Unified model deformation and flow transition measurements. Journal of Aircraft 1999;36(5):898–901.

[24] Burner, AW, Fleming, GA, and Hoppe, JC. Comparison of three optical methods for measuring model deformation, AIAA-2000-0835, January 2000.

[25] Burner AW, Liu T. Videogrammetric model deformation measurement technique. Journal of Aircraft 2001;38(4):745–54.

[26] Burner, AW, Liu, T and DeLoach, R. Uncertainty of videogrammetric techniques used for aerodynamic testing, AIAA 2002-2794, St. Louis, Missouri, June 2002.

[27] Burner, AW, Lokos, WA and Barrows, DA. In-flight aeroelastic measurement technique development, optical diagnostics for fluids, solids and combustion, Proceedings of SPIE, Vol. 5191, P. V. Farrell, F-P Chiang, C. Mercer and G. Shen (Eds.), 10, November 2003.

[28] Burner, AW, Goad, WK, Massey, EA, Goad, LR, Goodliff, SL, and Bissett, OW. Wing deformation measurements of the DLR-F6 transport configuration in the National Transonic Facility, AIAA 2008-6921, Honolulu, Hawaii, August 2008.

[29] Callaway, DW, Reeder, MF, and Greendyke, RB. Photogrammetric measurement of recession rates of low temperature ablators in supersonic flow, AIAA Paper 2010-1216, Orlando, FL, Jan. 2010.

[30] Carruthers AC, Walker SM, Thomas ALR, Taylor GK. Aerodynamics of aerofoil sections measured on a free-flying bird. Proceedings of the Institution of Mechanical Engineers, Part G: Journal of Aerospace Engineering 2010;224:855–64.

[31] Cattafesta LN, Iyer V, Masad J, King RA, Dagenhart JR. Three dimensional boundary-layer transition on a swept wing at Mach 3.5. AIAA Journal 1995;31(3):2032–7.

[32] Cattafesta, LN, and Moore, JG. Review and application of non-topographic photogrammetry to quantitative flow visualization, AIAA Paper 96-2180, June 1996.

[33] Chmielewski, AB, Moore, C, and Howard, R. The gossamer initiative, IEEE 0-7803-5846-5/00, 2000.

[34] Cipolla R, Giblin P. Visual Motion of Curves and Surfaces. Cambridge University Press; 2000.

[35] Curtis, DH, Reeder, MF, Svanberg, CE and Cobb, RG. Flapping wing micro air vehicle bench test set-up, AIAA Paper 2009-1272, Orlando, Florida, January 2009.

[36] Danehy, PM, Jones, TW, Connell, JW, Belvin, WK, and Watson, KA. Photogrammetry method for transparent, reflective, or dark surfaces, NASA Disclosure of Invention and New Technology (Including Software), December 2001.
[37] Donovan, JF, Morris, MJ, Pal, A, Benne, ME and Crites, RC. Data analysis techniques for pressure- and temperature-sensitive paint, AIAA Paper 93-0176, Jan. 1993.
[38] Dorrington AA, Jones TW, Danehy PM, Pappa RS. Laser-induced fluorescence photogrammetry for dynamic characterization of membrane structures. AIAA Journal 2004;42(10):2124–9.
[39] Dracos T, Gruen A. Videogrammetric methods in velocimetry. Applied Mechanics Reviews 1998;51(6):387–413.
[40] Engler, RH, Klein, C, Merlo, E, van Amerom, P. 360 degree PSP measurements in transonic flow, in: ICIASF 2001 Record, 19th International Congress on Instrumentation in Aerospace Simulation Facilities, Cleveland, OH, August 27–30, 2001, pp. 149–56.
[41] Faugeras O. Three-Dimensional Computer Vision. Cambridge: The MIT Press; 1993.
[42] Fleming, GA, and Burner, AW. Deformation measurements of smart aerodynamic surfaces, SPIE International Symposium on Optical Science, Engineering and Instrumentation, July 18–23, 1999, Denver, CO.
[43] Fleming, GA, Soto, HL, South, BW, Bartram, SM. Advances in projection Moiré interferometry development for large wind tunnel applications, Paper No. 1999-01-5598 Presented at the SAE 1999 World Aviation Congress and Exposition, San Francisco, CA, October 19–21, 1999.
[44] Florance, JP, Burner, AW, Fleming, GA, and Martin, CA. Contributions of NASA Langley Researcg Center to the DARPA/AFRL/NASA?Northrop Grumman Smart Wing Program, AIAA Paper 2003-1961, Norfolk, VA, 2003.
[45] Fraser, CS. Photogrammetric camera component calibration — a review of analytical techniques, Workshop on Calibration and Orientation of Cameras in Computer Vision (TU-1), XVII Congress, International Society of Photogrammetry & Remote Sensing, Washington, DC, 1992.
[46] Fraser CS. Optimization of networks in non-topographic photogrammetry. In: Karara HM, editor. Non-Topographic Photogrammetry. 2nd edn. Falls Church, VA: American Society for Photogrammetry and Remote Sensing; 1989. p. 95–106 Chapter 8.
[47] Fryer JG. Camera calibration in non-topographic photogrammetry. In: Karara HM, editor. Non-Topographic Photogrammetry. 2nd Edition. Falls Church, VA: American Society for Photogrammetry and Remote Sensing; 1989. p. 59–69 Chapter 5.
[48] Ganci, G and Brown, J. Developments in non-Contact measurement using videogrammetry, Proceedings of the Boeing Large Scale Metrology Conference, February 2000.
[49] Gilbert, MG, Welch, SS, Pappa, RS, and Demeo, ME. STS-74/MIR photogrammetric appendage structural dynamics experiment preliminary data analysis, AIAA Paper 97-1168, April 1997.
[50] Graves SS, Burner AW, Edwards J,W, Schuster DM. Dynamic deformation measurements of an aeroelastic semispan model. Journal of Aircraft 2003;40(5):977–84.
[51] Graves, SS and Burner, AW. Development of an intelligent videogrammetric wind tunnel measurement system, optical diagnostics for fluids, solids, and combustion, SPIE International Symposium on Optical Science and Technology, San Diego, CA, 29 July to 3 August, 2001.
[52] Gruen A, Huang TS. Calibration and Orientation of Cameras in Computer Vision. Berlin: Springer-Verlag; 2001.
[53] Hooker, JR, Burner, AW, Valla, R. Static aeroelastic analysis of transonic wind tunnel models using finite element methods. AIAA Paper 97-2243, June 1997.
[54] Jacob, JD. Gust encounters in rigid and flexible fixed wing MAVs, AIAA Paper 2010-69, Orlando, FL, Jan. 2010.
[55] Jenkins CHM, editor. Progress in Astronautics and Aeronautics, Vol. 191. Reston, VA: AIAA; 2001.
[56] Jones, TW and Pappa, RS. Dot projection photogrammetric technique for shape measurements of aerospace test articles, AIAA Paper 2002-0532, Reno, NV, Jan. 2002.
[57] Jones T, Dorrington AA, Blandino JR, Fraser C, Liu T. Photogrammetric Measurement Methods Gossamer Structures. Washington DC: AIAA Press; 2006 Chapter 5.
[58] Jones, TW and Lunsford, CB. Design and development of a real-time model attitude measurement system for hypersonic facilities, AIAA Paper 2005-1411, Reno, NV, Jan. 2005.
[59] Jones, TW, Downey, JM, Lunsford, CB, Desabrais, KJ and Gregory Noetscher, G. Experimental methods using photogrammetric techniques for parachute canopy shape measurements, AIAA Paper 2007-2550, Williamsburg, VA, May 2007.
[60] Kellas, S, et al. Full scale crash test of an MD500 helicopter with deployable energy absorbers, Proceedings of the 66th AHS Annual Forum, Phoenix, Arizona, May 2010.
[61] Kolmogorov AN, Formin SV. Introductory Real Analysis. New York: Dover; 1970.
[62] Lenz R, Fritsch D. Accuracy of videogrammetry with CCD sensors. ISPRS Journal of Photogrammetry and Remote Sensing 1990;45:90–110.
[63] Le Sant Y, Merienne M-C. An image resection method applied to mapping techniques. ICIASF '95 Record, International Congress on Instrumentation in Aerospace Simulation Facilities, Wright-Patterson Air Force Base, Dayton, OH 1995:46.1–8 July 18–21.
[64] Littell, JD. Large field photogrammetry techniques in aircraft and spacecraft impact testing, society of experimental mechanics, SEM Annual Conference, Indianapolis, Indiana, June 2010.
[65] Liu T, Campbell B, Burns S, Sullivan J. Temperature- and pressure-sensitive paints in aerodynamics. Applied Mechanics Reviews 1997;50(4):227–46.
[66] Liu T, Radeztsky R, Garg S, Cattafesta L. A videogrammetric model deformation system and its integration with pressure paint. AIAA 99-0568; 1999.
[67] Liu T, Cattafesta L, Radezsky R, Burner AW. Photogrammetry applied to wind tunnel testing. AIAA Journal 2000;38(6):964–71.
[68] Liu T, Barrows DA, Burner AW, Rhew RD. Determining aerodynamic loads based on optical deformation measurements. AIAA Journal 2002;40(6):1105–12.
[69] Liu T. Geometric and kinematic aspects of image-based measurements of deformable bodies. AIAA Journal 2004;42(9):1910–20.
[70] Liu T, Sullivan JP. Pressure and Temperature Sensitive Paints. Berlin: Springer; 2004.
[71] Liu, T and Fleming, G. Videogrammetric determination of aircraft position and attitude for vision-based autonomous landing, AIAA Paper 2006-1437, Reno, January, 2006.
[72] Liu, T and Burner, AW. Photogrammetry Toolbox Reference Manual, NASA Langley Research Center Contract Report, May, 2007.
[73] Liu T, Shen L. Fluid flow and optical flow. Journal of Fluid Mechanics 2008;614(11):253–91.
[74] Longuet-Higgins HC. A computer algorithm for reconstructing a scene from two projections. Nature 1981;293:133–5 10, September.
[75] Lunsford, N and Jacob, J. High speed videogrammetry of flexible wings in flapping flight, AIAA Paper 2009-722, Orlando, FL, Jan. 2009.
[76] Maas HG, Gruen A, Papantoniou D. Particle tracking velocimetry in three-dimensional flows. Experiments in Fluids 1993;15:133–46.
[77] McGlone JC. Analytic data-reduction schemes in non-topographic photogrammetry. In: Karara HM, editor. Non-Topographic Photogrammetry. 2nd Edition. Falls Church, VA: American Society for Photogrammetry and Remote Sensing; 1989. p. 37–55 Chapter 4.
[78] McInnes CR. Solar Sailing — Technology, Dynamics and Mission Applications. Chichester, UK: Praxis Publishing Ltd; 1999.
[79] Meirovitch L. Analytical Methods in Vibrations. New York: The Macmillan Company; 1967.
[80] Mikhail EM, Bethel JS, McGlone JC. Introduction to Modern Photogrammetry. New York: John Wiley & Sons, Inc.; 2001.
[81] Mundy JL, Zisserman A. Projective geometry for machine vision. In: Mundy J, Zisserman A, editors. Geometric Invariance in Computer Vision. Cambridge: The MIT Press; 1992.
[82] Naughton JW, Liu T. Photogrammetry in oil film interferometry. AIAA Journal 2007;45(7):1620–9.
[83] Pappa, RS, Jones, TW, Black, JT, Walford, A, Robson, S, and Shortis, MR. Photogrammetry methodology development for gossamer spacecraft structures, AIAA Paper 2002-1375, April 2002a.
[84] Pappa RS, Jones TW, Black JT, Walford A, Robson S, Shortis MR. Photogrammetry methodology for gossamer spacecraft structures. Sound and Vibration 2002;36(8):12–21.
[85] Pappa RS, Black JT, Blandino JR, Jones TW, Danehy PM, Dorrington AA. Dot-projection photogrammetry and videogrammetry of gossamer space structures. Journal of Spacecraft and Rockets 2003;40(6):858–67.
[86] Pierre DA. Optimization Theory with Applications. New York: Dover; 1986 pp. 264–86.
[87] Pitcher, NA and Maple, RC. A static aeroelastic analaysis of a flexible wing mini unmanned aerial vehicle, AIAA Paper 2008-4057, Seattle, WA, June 2008.
[88] Prasad AK, Adrian RJ. Stereoscopic particle image velocimetry applied to liquid flows. Experiments in Fluids 1993;15(1):49–60.
[89] Raffel M, Willert C, Wereley S, Kompenhans J. Particle Image Velocimetry.2nd edn. Berlin: Springer; 2007.
[90] Reddy JN. Theory and Analysis of Elastic Plates. Philadelphia: Taylor & Francis; 1999.
[91] Roy, JP, Britcher, C, and Liu, T. Extracting dynamic loads from optical deformation measurements, AIAA Paper 2006-2187 2006.
[92] Ruyten W, Sellers M. On-line processing of pressure-sensitive paint images. Journal of Aerospace Computing, Information, and Communication 2004;1:372–82.
[93] Ruyten W. Model attitude determination in wind tunnel with a luminescent paint data system. AIAA Journal 2000;38(9):1692–7.
[94] Ruyten W. More photogrammetry for wind tunnel testing. AIAA Journal 2002;40(7):1277–83.
[95] Rüther H. An overview of software in non-topographic photogrammetry. In: Karara HM, editor. Non-Topographic Photogrammetry. 2nd Edition. Falls Church, VA: American Society for Photogrammetry and Remote Sensing; 1989. p. 129–45 Chapter 10.
[96] Ryall TG, Fraser CS. Determination of structural modes of vibration using digital photogrammetry. Journal of Aircraft 2002;39(1):114–9.
[97] Salvi J, Armanhue X, Batlle J. A comparative review of camera calibrating methods with accuracy evaluation. Pattern Recognition 2002;35:1617–35.
[98] Sasa, S, Gomi, H, Ninomiya, T, Inagaki, T, and Hamada, Y. Position and attitude estimation using image processing of runway, AIAA Paper 2000-0301, Reno, NV, Jan. 2000.
[99] Schairer ET, Hand L. Measurements of unsteady aeroelastic model deformation by stereo photogrammetry. Journal of Aircraft 1999;36(6):1033–40.
[100] Schairer, ET and Heincek, JT. Photogrammetric recession measurements of ablative materials during arcjet testing, AIAA Paper 2007-1158, Reno, Jan. 2007.

[101] Shih Tian-Yuan. On the duality of relative orientation. Photogrammetric Engineering and Remote Sensing 1990;56(9):1281–3.
[102] Shortis MR, Beyer HA. Sensor technology for digital photogrammetry and machine vision. In: Atkinson KB, editor. Close Range Photogrammetry and Machine Vision. Scotland, UK: Whittles Publishing; 2001. p. 106–55.
[103] Spain, CV, Heeg, J, Ivanco, TG, Barrows, D, Florance, JR, Burner, AW, et al. Assessing videogrammetry for static aeroelastic testing of a wind-tunnel model, AIAA Paper 2004-1677, Palm Springs, CA, April 2004.
[104] Tian X, Iriarte-Diaz J, Middleton K, Galvao R, Israeli E, Roemer A, et al. Direct measurements of the kinematics and dynamics of bat flight. Bioinspiration & Biomimetics 2006;1:S10–8.
[105] Trisiripisal, P, Parks, MR, Abbott, AL Liu, T and Fleming, GA. Stereo analysis for vision-based guidance and control of aircraft landing, AIAA Paper 2006-1438, Reno, January, 2006.
[106] Tsai RY. A versatile camera calibration technique for high-accuracy 3D machine vision metrology using off-the-shelf TV cameras and lenses. IEEE Journal of Robotics and Automation 1987;RA-3(4):323–44.
[107] Warburton GB. The vibration of rectangular plates. Proceedings of the Institution of Mechanical Engineers 1954;168(12):371–83.
[108] West JL, Derbes B. Solar sail vehicle system design for the GEOstorm warning mission. AIAA 2000-5326; 2000.
[109] Wolf P. Elements of Photogrammetry. New York: McGraw-Hill; 1983.
[110] Wong KW. Basic mathematics of photogrammetry. In: Slama CC, editor. Manual of Photogrammetry. 4th edn. Falls Church, Virginia: American Society of Photogrammetry; 1980. p. 37–101 Chapter 2.
[111] Zeng Z, Wang X. A general solution of a closed-form space resection. Photogrammetric Engineering and Remote Sensing 1992;58(3):327–38.